1-D Modeling of a Bubbling Fluidized Bed Gasifier

From Biogenic and Waste Feedstocks to Syngas: A Deep Dive into Fuel Conversion Behaviour

MSc Graduation Thesis

Stella Theodoraki

Delft University of Technology

1-D Modeling of a Bubbling Fluidized Bed Gasifier

From Biogenic and Waste Feedstocks to Syngas: A Deep Dive into Fuel Conversion Behaviour

by

Stella Theodoraki

to obtain the degree of Master of Science in Sustainable Energy Technology
at the Delft University of Technology.

Student Number:	5973627
TU Delft Promotor:	Prof. dr. ir. Wiebren de Jong
TU Delft Supervisor:	Dr. Anna Felden
Company Supervisor:	Dr. Avishek Goel
Project Duration:	November, 2024 - August, 2025
Faculty:	Faculty of EEMCS, TU Delft

Cover: Gasification Systems by HoSt Bioenergy
Style: TU Delft Report Style, with modifications by Daan Zwaneveld

Preface

This thesis project was carried out in collaboration with Gidara Energy Holdings B.V, located in Schiphol, Amsterdam in order to acquire the MSc diploma from the Sustainable Energy Technology master's program of TU Delft.

First and foremost, I would like to start by thanking my TU Delft supervisors, Prof. dr. ir. Wiebren de Jong and Dr. Anna Felden, for the invaluable academic support throughout my thesis. Their guidance and constructive feedback were essential in the completion of this thesis project.

In addition, I would also like to thank my company supervisor, Avishek Goel. Although this thesis project did not begin under his supervision, his guidance and encouragement were instrumental in bringing this project to an end.

What is more, I would like to extend special thanks to Nivya Uday Kodimaniyanda and Avikar Saberwal, for providing me with helpful insights into the bubbling fluidized bed technology, which really helped me grasp the core aspects of the process.

To everyone at GIDARA Energy, I am truly thankful for the warm atmosphere and welcoming environment. From day one, I felt like a part of the team, and I really appreciate this.

I would also like to thank and acknowledge the scholarship provided to me by HelleniQ Energy for my studies at TU Delft, during the period of 2023-2025.

Last but definitely not least, a special thanks to my friends and family, and above all Haris, who supported me through this (sometimes rough) journey. This thesis could not have been made possible without you.

Stella Theodoraki
Delft, August 2025

Summary

As the energy demand is growing rapidly across the globe due to industrialization and higher living standards, along with the depletion of fossil fuel reserves and the effect of climate change more evident than ever [1], there is an urgent need to transition to sustainable methods of energy production. Among various sustainable energy alternatives, bio-energy is expected to play a significant role in the energy transition. Gasification constitutes a thermochemical way of converting carbonaceous feedstock into useful energy. When implemented with biogenic or waste-derived fuels, gasification can provide a promising sustainable energy solution, while it can also simultaneously deal with the landfill waste problem when utilizing feedstocks like Solid Recovered Fuel (SRF). Despite the fact that gasification of coal is often featured in literature, the use of biomass or SRF in gasification practices is still limited. Specific areas like the handling of tars, detailed modeling of the hydrodynamics in the fluidized bed and the freeboard of the reactor, as well as the implementation of chemical kinetics specific to waste-derived feedstocks remain underexplored in literature. Furthermore, many studies completely ignore the freeboard region in their models, where critical reactions still occur. Therefore, the aforementioned research gaps are aimed to be answered to in the current thesis project. The purpose of this Master Thesis was to study bubbling fluidized bed gasification and develop a model of its processes using the Python programming language. The open-source software ”Cantera” was used [2], which contains tools for dealing with reaction kinetics, thermodynamics and transport phenomena. To be more exact, the python model includes the chemical reaction kinetics, the mass transfer, and finally the fluid mechanics in the reactor and calculates the composition of the final exiting gas, as well as other physical parameters of the process. The added value of this thesis project lies in the validation of the developed model against experimental results obtained from a series of tests carried out at the TU Darmstadt gasification facility, when experimental gasification campaigns were conducted using Solid Recovered Fuel (SRF) [3]. In addition, this work contributes to the modernization and further development of the model originally presented in Hamel’s PhD thesis [4]. The modeling approach that was followed for the construction of this model was based on a 1-D cell model, where the fluidized bed and the freeboard were discretized in control volumes. Within these control volumes, the local hydrodynamics and the gasification reactions were applied, through mass balance equations. As initial conditions for the gasification model, the outputs of a pyrolysis model were used, applied to the incoming feedstock. The final results of the numerical model show good agreement with the experimental set of data from the TU Darmstadt gasification campaign. More specifically, the model manages to predict with reasonable accuracy the concentrations of four out of the five major syngas species considered. The most notable shortcoming of the model lies in the prediction of the methane content in the final syngas, as this was completely depleted inside the bed, which is an unrealistic behavior given the operating temperature range of the gasification process. This deviation likely lies in the fast kinetics of the steam methane reforming and methane oxidation reactions, pinpointing the need for more accurate reaction kinetics. However, the content of CO, H_2, CO_2 and H_2O were captured reasonably well. In addition, the model predicted a carbon conversion efficiency of 100%, which is unrealistic compared to typical values of around 70-90 % that are observed in real-life applications. This value overestimation lies in the fact that carbon is treated as a pseudo-gaseous species in the model, as well as in the fact that incomplete carbon conversion mechanisms, such as bottom ash removal or particle entrainment with the syngas, are not being considered. Different tests of sensitivity analysis were also conducted to assess the effect of different key parameters on the final product, including the freeboard temperature, the initial gasification conditions, the gaseous distribution through the nozzles and different kinetic parameters. Overall, the model managed to come close to the experimental results, demonstrating its potential in simulating the use of waste-derived fuels in a bubbling fluidized bed gasifier. Therefore, it provides a strong basis for further exploration and development.

Contents

List of Figures

List of Tables

Nomenclature

Abbreviations

Abbreviation	Definition
a.r	as received
daf	dry, ash-free
BBM	Black-Box Method
BFB	Bubbling Fluidized Bed
CFB	Circulating Fluidized Bed
CFD-DEM	Computational Fluid Dynamics with Discrete Elements Method
CFD-M	Computational Fluid Dynamics Method
ER	Equivalence Ratio
FM	Fluidization Method
IEA	International Energy Agency
LHV	Lower Heating Value
MP-PIC	Multiphase Particle In Cell
PGZ	Post - Gasification Zone
S/C	Steam-to-Carbon Ratio
SEG	Sorption Enhanced Gasification
SRF	Solid Recovered Fuel
TFM	Two-Fluid Model

Symbols

Symbol	Definition	Unit
A	Area	[m^2]
Ar	Archimedes Number	[-]
c_b	Resistance Coefficient of the Rising Bubble	[-]
c_i	Concentration of species i	[kmol/m^3]
c_w	Drag Coefficient	[-]
c_b	Resistance Coefficient of Rising Bubble	[-]
E_a	Activation Energy	[J/mol]
d	Diameter	[m]
d_p	Particle Diameter	[m]
d_b	Bubble Diameter	[m]
$d_{b,WS}$	Bubble Diameter at the Fluidized Bed Surface	[m]
d_{bed}	Bed Diameter	[m]
$d_{bed,bottom}$	Bed Bottom Diameter	[m]
$d_{bed,top}$	Bed Top Diameter	[m]
d_{sv}	Sauter Diameter	[m]
dm	Size of Discretized Cell in the Freeboard	[m]
dn	Size of Discretized Cell in the Fluidized Bed	[m]
F	Force	[N]

Symbol	Definition	Unit
f_d	Empirical Coefficient for Dynamic Viscosity Calculation	[-]
f_w	Empirical Parameter for the Calculation of the Solids Discharge due to the Wake Mechanism	[-]
g	Acceleration of Gravity	[m/s^2]
H	Height	[m]
h	Height	[m]
I_P	Maximum Number of Reactions Taking Place	[-]
M	Mass	[kg]
M	Number of Discretized Cells in the Freeboard	[-]
m	Index of Current Cell in the Freeboard	[-]
$m_{in,b}$	Mass Flow Entering Through the Bed Nozzles	[kg/s]
$m_{in,FB}$	Mass Flow Entering Through the Freeboard Nozzles	[kg/s]
$M_{particles}$	Mass of Particles	[kg]
$\dot{M}$	Mass Flow	[kg/s]
$\dot{M}_{A,b,j}$	Exchange Gas Mass Flow of Species j in Bubble Phase	[kg/s]
$\dot{M}_{A,d,j}$	Exchange Gas Mass Flow of Species j in Emulsion Phase	[kg/s]
$\dot{M}_{b,j}$	Convective Gas Mass Flow of Species j in Bubble Phase	[kg/s]
$\dot{M}_{d,j}$	Convective Gas Mass Flow of Species j in Emulsion Phase	[kg/s]
$\dot{M}_{in,b,j}$	External Gaseous Inflows in the Bubble Phase	[kg/s]
MW	Molecular Mass	[kg/kmol]
N	Number of Discretized Cells in the Fluidized Bed	[-]
n	Index of Current Cell in the Fluidized Bed	[-]
n_0	Number of Outlet Openings in Nozzle Base	[-]
n_b	Empirical Coefficient for the Calculation of the Bubble Volume Fraction	[-]
n_{RZ}	Richardson-Zaki exponent	[-]
P	Pressure	[Pa]
r	Reaction Rate	[mol ·m^3/s]
R	Universal Gas Constant	[J/(mol·K)]
R_2	Coefficient of Determination	[-]
Re	Reynolds Number	[-]
R_i	Reaction Rate of Reaction i	[kmol/s]
t	Time	[s]
T	Temperature	[K]
u	Velocity	[m/s]
V_{cell}	Volume of a Cell	[m^3]
V_{gas}	Volume of Gas	[m^3]
$V_{freeboard}$	Volume of the Freeboard	[m^3]
$V_{particles}$	Volume of Particles	[m^3]
V_p	Volume of a Particle	[m^3]

Symbol	Definition	Unit
$\dot{V}_0$	Initial Volumetric Flow Rate	[m^3/s]
v_b	Experimental Parameter for the Calculation of the Bubble Rise Velocity	[-]
Y	Mass Fraction of a species	[-]
y	Midpoint of Each Discretized Cell in the Fluidized Bed	[m]
y_{FB}	Midpoint of Each Discretized Cell in the Freeboard	[m]
α_b	Bubble Index	[-]
β_A	Decay Constant	[-]
ϵ_b	Bubble Volume Fraction	[-]
ϵ_d	Emulsion Porosity	[-]
ϵ_{mf}	Bed Voidage at Minimum Fluidization	[-]
ϵ_{PGZ}	Voidage in the Freeboard	[-]
λ_b	Average Lifespan of Bubble	[-]
μ_g	Gas Dynamic Viscosity	[kg/(m ·s)]
ν_g	Gas Kinematic Viscosity	[m^2/s]
$\nu_{i,j}$	Stoichiometric Coefficient of component j in reaction i	[-]
ρ	Density	[kg/m^3]
ρ_b	Bubble Phase Density	[kg/m^3]
ρ_d	Emulsion Phase Gas Density	[kg/m^3]
ρ_p	Particle Density	[kg/m^3]
ρ_g	Gas Density	[kg/m^3]
$\tau_{res,bed}$	Residence Time in the Bed	[s]
$\tau_{res,freeboard}$	Residence Time in the Freeboard	[s]
ϕ	Sphericity	[-]

Subscripts

Subscript	Definition
0	Empty Cross-Section
A	Buoyancy (Force)
b	Bubble Phase
bed	Bed
b,i	Isolated Bubble
b,WS	Bubble at the Fluidized Bed Surface
ch	Char
d	Dense Phase
F	Dry, Ash-Free Fuel
g	Gas
gb	Ghost Bubble
G	Gravitational (Force)
k	Solids
mf	Minimum Fluidization
p	Particle
$p,0$	Particle at Initial State
PGZ	Freeboard
s	Sinking Particle
T	Inertia (Force)
W	Drag (Force)

1

Introduction

1.1. Global Energy Landscape

In the past few decades, the global demand for energy has risen significantly, driven by a growing global population, the expansion of industrial activities, urbanization, higher incomes, rising living standards and increased consumption patterns. In 2018, the International Energy Agency (IEA) projected that the global energy consumption would increase by more than 25% by 2040 under the current implemented policies [1]. This persistent growth places enormous pressure on existing energy systems, which are still largely dependent on fossil fuels, since according to IEA, in 2023, fossil fuels met 80% of global energy demand [5]. The reliance on coal, oil, and natural gas not only raises concerns about the finite nature of these resources, but also contributes substantially to the worsening climate crisis, anthropogenic global warming and greenhouse gas emissions of which CO_2 is the largest contributor [6, 7]. Therefore as global temperatures continue to rise to unprecedented levels, compared to pre-industrial times [8], the planet is experiencing a disturbing increase in natural disasters and catastrophes [9]. In response to these alarming events, mankind has looked for ways to avert this situation and address the environmental damage that still remains reversible. Although the IEA predicts that the growth rate of energy demand will slow down due to to efficiency gains, increasing electrification and a rapid build-out of renewables [5], the importance and urgency of sustainable measures is still evident. A transition towards renewable and sustainable energy sources can help meet future energy demands, while simultaneously limiting the environmental impact.

Among the diverse range and options of renewable energy sources (such as solar, wind, and hydro) bio-energy (renewable energy produced from plants and animal waste [10]) is acknowledged as one of the technologies that need to exist in future's renewable energy mix in order to drive the greenhouse gas emissions down by 2050 [5]. According to the IEA's Net Zero by 2050 scenario, modern bio-energy is expected to contribute around 15% of total final consumption in 2050 [11], emphasizing its vital role in the future energy mix. Biomass holds unique potential due to its versatility and possibility to act as a carbon-neutral (or even carbon-negative when integrated with carbon-capture technologies [5]) option, that is able to supply energy in the form of heat, electricity, as well as fuels [5]. The term biomass is used to refer to organic material derived from plants, agricultural residues, forestry byproducts and energy crops. In addition, various forms of organic waste — such as Municipal Solid Waste (MSW), Solid Recovered Fuel (SRF), industrial byproducts, and sewage sludge — can also serve as valuable feedstocks for bio-energy. The term SRF refers to a high-quality waste stream, which is derived by shredding and dehydrating solid waste [12], such as paper, card, wood, plastics, textiles, food and kitchen waste. SRF is characterized by a relatively high calorific value, due to a pre-processing that it undergoes [13, 12]. The utilization of waste streams not only contributes to energy generation but also supports circular economy principles by reducing landfill usage and mitigating methane emissions from un-managed decomposition of landfill waste. Biogenic and waste-derived feedstocks can be converted into useful energy through, for example, biochemical or thermochemical pathways [14]. Biochemical or biological conversion is typically suited for wet, biodegradable biomass and involves processes like anaerobic digestion (commonly used to produce biogas) and fermentation (commonly used to produce bio-ethanol) [14]. On the other hand, thermochemical conversion — including combustion, pyrolysis, and gasification — is more suitable for dry, lignocellulosic feedstocks or SRF and offers the advantage of higher conversion efficiencies and flexible end-product [15]. This thesis focuses on the gasification process and its potential role in contributing to a more sustainable energy mix of the planet.

1.2. Gasification

1.2.1. Gasification Principle

Gasification is a thermochemical process, converting carbonaceous fuel into combustible gases, which has seen a lot of research and development into it the past couple of decades [16]. The gasification technology can be utilized with both fossil and non-fossil fuels, but, as previously mentioned, this thesis focuses only the use of biogenic and waste-derived feedstock in gasification processes. Studies have shown that depending on the gasification technology utilized, the carbon dioxide emissions from such a process can be reduced up to 90%, compared to the carbon dioxide emissions from a conventional combustion process [17] [16]. Gasification can be accomplished with different types of gasification agents, such as air, oxygen, steam or a combination of those. Air gasification leads to the formation of a product with a low heating value (around 4-6 MJ/m^3), while steam gasification forms products of higher quality and higher heating value [18].

The product gas exiting from a gasifier is called synthesis gas or syngas. Syngas consists of a mixture of mainly CO and H_2, and also CO_2 and CH_4 to a lesser amount [19]. Some other products that arise from gasification are tars, steam and char, the production rate of which can be controlled by the gasification conditions [20]. However, its main desired product is syngas, which is very versatile, as it can be used as a base to form other chemicals (such as ammonia, methanol or Fischer-Tropsch fuels) or used for power generation (i.e. in gas turbines), as it is a fuel with high chemical energy [16].

In order to make syngas suitable for its downstream applications, a gas cleaning process is required. This removes the undesirable by-products found in the syngas flow, but also eliminates trace elements, such as sulfur or nitrogen, that can be detrimental to the catalysts used and cause their deactivation [21]. The goal is to end up with a gas consisting as much exclusively as possible of H_2 and CO [3].

The gasification process consists of various individual steps, such as:

1. **Drying.**
   Based on the gasification process and the designing of the reactor, the fuel enters the reactor either from the bottom or the top. The fuel feeding options depend on the fuel type and on the system configuration, with common methods including auger (screw) feeders for granular solids and pneumatic transport for fine or lightweight materials [22]. During drying, which occurs at around 100-200° C, the surface water content of the feedstock is removed and turned into vapor [23].
2. **Pyrolysis or devolatilization.**
   Pyrolysis occurs during the heating of the feedstock between 300-700° C under oxygen deprived conditions. At this stage, the thermal decomposition of the feedstock is carried out, with tars, char, gases and steam being released [16]. As far as the reaction kinetics of pyrolysis are concerned, there are two main approaches that are followed. The first approach refers to the use of kinetics reported in literature sources, while the second approach assumes that pyrolysis takes place instantaneously [24].
3. **Oxidation or combustion.**
   During the oxidation stage of gasification, the pyrolysis products (the char and gases) react with free or bound oxygen (in the form of steam or CO_2). The general heterogeneous solid-gas and homogeneous gas-gas chemical reactions that take place, along with their enthalpies of formation, are listed in Table 1.1.
4. **Reduction or gasification.**
   During the reduction stage, the gases that are produced from the combustion reactions (carbon dioxide and steam) (see Reactions R1, R2 from Table 1.1) take then part in the gasification reactions that happen afterwards, providing the necessary oxygen for them (see Reactions R3-R5

from Table 1.1).

Table 1.1: List of global reactions taking place, their enthalpies, and descriptions

Reaction	Equation	ΔH_r [kJ/mol]	Description
R1	$2\,CO + O_2 \leftrightarrow 2\,CO_2$	-246.7	Combustion
R2	$2\,H_2 + O_2 \leftrightarrow 2\,H_2O$	-241.8	Combustion
R3	$C + CO_2 \leftrightarrow 2\,CO$	+159.6	Boudouard Reaction
R4	$C + H_2O \leftrightarrow CO + H_2$	+118.5	Carbon-Steam Reaction
R5	$CO + H_2O \leftrightarrow CO_2 + H_2$	-41.1	Water-Gas Shift Reaction

The exact composition of the exiting syngas is hard to predict. One reason for this is the low residence times that prevail in most gasifier setups, in which cases it is rather difficult to reach a chemical equilibrium. Therefore, the reaction kinetics are the ones dominating the process. Since these kinetics are strongly dependent on the type of feedstock used, experimental studies are necessary for each feedstock, in order to calculate the relevant reaction rates and design the gasification process accordingly. However, the syngas composition can also be adjusted to a certain extent to the requested levels, by using the Water-Gas Shift Reaction (R5 from Table 1.1) [16].

1.2.2. Types of Gasifiers

Gasifiers come in many different types and designs, the main ones being the fixed bed gasifier (updraft or downdraft), the fluidized bed gasifier (bubbling, circulating or dual) and the entrained flow gasifier (see Fig. 1.1). A positive characteristic of the fluidized bed gasifier is their fuel flexibility, allowing them to handle a wide range of feedstocks [25]. Contrary to that, an entrained flow gasifier requires pulverized fuel, which means that a high degree of pretreatment of the feedstock is essential [26].

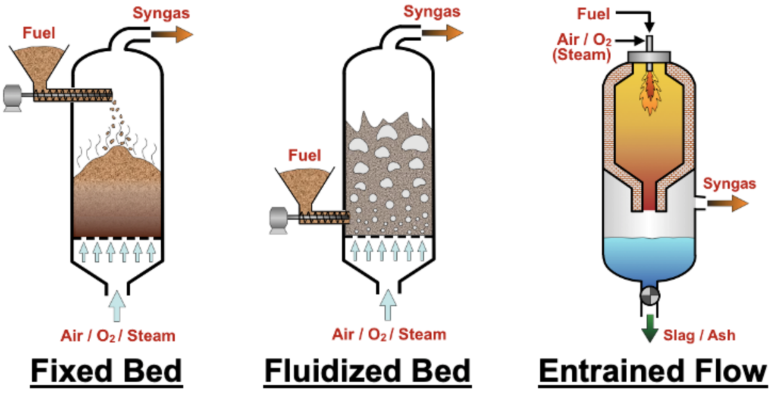

Figure 1.1: Different types of gasifiers. [27]

A gasifier setup typically includes one or two vessels, which are filled with solid particles that are called the bed material [19]. The operating conditions differ from one type of gasifier to another, hence leading to a wide range of syngas products. For example, it has been observed that the syngas products derived from a fluidized bed gasifier or an updraft fixed bed gasifier, can lead to the creation of higher methane and tar compounds compared to the other types of gasifiers [28]. In addition, in the case of updraft fixed bed gasifiers, a significant syngas cleaning is needed before the syngas can be used as a product, due to the large amount of unwanted products that are formed. Downdraft fixed bed gasifiers produce a much cleaner syngas product, but face significant limitations with up-scaling, such as poor flow distribution and localized high temperatures [29], hence not being able to be used in facilities of large capacity.

1.2.3. Fluidization and Fluidized Bed Gasifiers

As far as fluidized bed gasifiers are concerned, it is first important to understand the concept of fluidization. Fluidization is the process where a bed of solid particles acts as a fluid, when a gas or liquid (called the fluidization agent) is passed upwards through it. The gas or liquid is inserted from the bottom of the reactor, through a gas distributor in order to provide a uniform velocity profile that will flow through the bed of solid particles and transform it into a fluid-like body (see Figure 1.2). For fluidization to be achieved however, the velocity of the gas needs to reach a certain threshold, which is characteristic for each setup, called the minimum fluidization velocity u_{mf}. When the upward velocity of the gas is low, the upward drag force acting on the bed of particles is not enough to overcome the weight force of the solid bed, and therefore the bed remains fixed. However, when the upward velocity of the gas is high enough, the solid particles become suspended and start acting like a fluid. When the gas velocity increases above the minimum fluidization velocity u_{mf}, channeling of the gas and bubbles are noticed. As the gas velocity increases further, agitation intensifies, causing the solids to move even more rapidly, without causing however the bed to expand significantly past its volume at minimum fluidization [23]. The bed of solids is called the bubbling fluidized bed under these conditions. In a bubbling fluidized bed, gas moves through it in void or in the form of bubbles with a higher velocity. At the top of the bed, the gas can cause some particles to become entrained into the post-gasification zone, with some fine particles being carried to the exit of the gasifier and into the cyclone by the flowing gas. However, most entrained particles actually fall back down to the bed and are removed along with the ash from the bottom of the reactor [18]. Figure 1.2 shows a simplified view of the fluidization process.

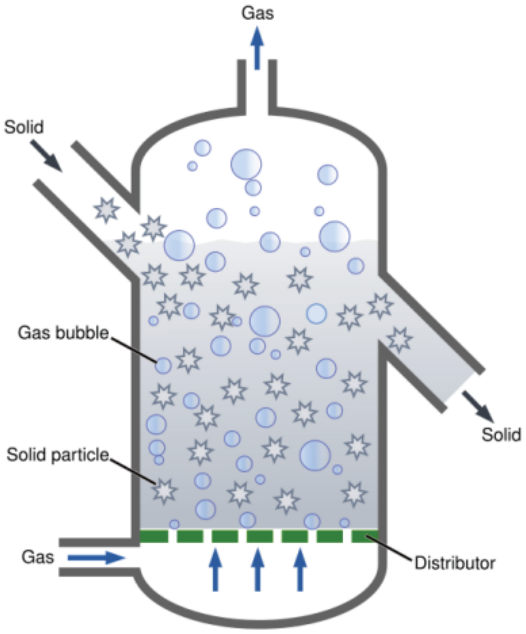

Figure 1.2: Simplified view of the fluidization process [30].

It should be noted that depending on the velocity of the gas (also called the fluidization agent) we can distinguish different types of fluidization, from bubbling to turbulent and fast. Figure 1.3 depicts the different types of fluidization based on the gas velocity.

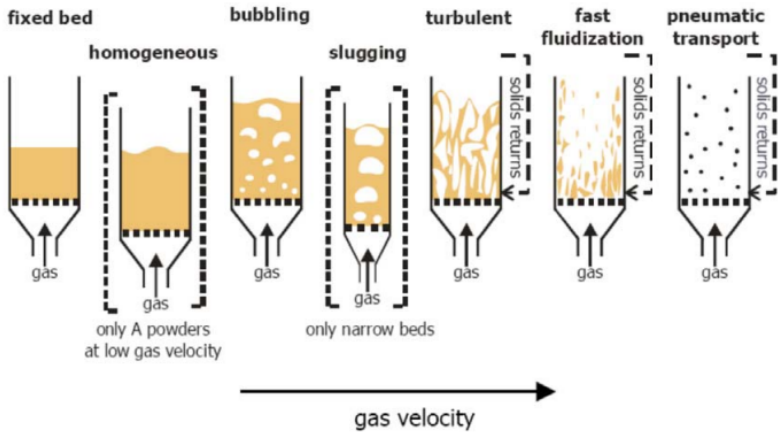

Figure 1.3: Different types of fluidization based on the gas velocity. [30]

Fluidized beds are commonly classified into three main types: bubbling, circulating, and dual fluidized beds. This study focuses specifically on the bubbling fluidized bed, as it is the configuration used in our case.

The conditions prevalent in a bubbling fluidized bed result in an effective mixing of the solids and gases as well as a uniform temperature across the bed and therefore an increased carbon conversion efficiency and a syngas product with a higher High Heating Value [19]. Another favorable feature of the fluidized bed gasifiers is their ability to be implemented with a wide variety of feedstocks, such as biomass and waste-derived fuels (which is also this case study), while they show promise for scale up [18]. On the other hand, some disadvantages include the formation of tars during the process, as well as the need to control the temperature to levels lower than the ash melting point, so as to avoid agglomeration, which refers to the undesirable formation of assemblages which can cause operational problems [31]. In a fluidized bed gasifier, there is usually the presence of an external bed material inside the reactor (such as sand, olivine or alumina) to improve the energy transfer between the particles and enhance heat distribution, maintain uniform temperature, and promote better gas-solid contact for more efficient gasification [18]. A circulating fluidized bed (CFB) gasifier uses a circulating loop for the continuous flow of solid particles in order to increase the gasification efficiency. In CFBs, the conversion of carbon is higher compared to a bubbling fluidized bed (BFB), while they are also characterized by a lower tar formation [19]. Another advantage of a CFB, is that they can operate on a wider range of feedstock type and size, compared to a BFB, but the operation of the latter ones has been studied more than that of the former and therefore, there is more academic knowledge about it. A dual fluidized bed gasifier basically combines two circulating beds or one circulating and one bubbling [32].

A typical bubbling fluidized bed gasification process includes a gasification reactor, the feeding system, the bottom ash removal system (located below the gasifier), a cyclone at the exit of the gasifier and a recirculation loop. After the syngas exits the cyclone, it is cooled in the raw gas cooler (releasing heat, which can be exported and financially exploited) and undergoes a process to remove its dust, or fly ash, in a ceramic filter. Depending on the process requirements, the produced syngas can be cleaned using either wet or dry gas cleaning methods. In wet cleaning methods, the syngas is passed through a wet scrubber, where it is quenched with water in order to remove the the remaining contaminants. Contrary to that, in dry cleaning methods, high temperature filters are implemented in order to remove particulates and other contaminants [33]. The feeding system includes gravity pipes or screw conveyors that provide the feedstock to the gasifier, while the feeding and removal of bottom ash need to be performed by lock-hopper systems due to the high gasifier pressure [34]. Figure 1.4 presents a simplistic depiction of this process.

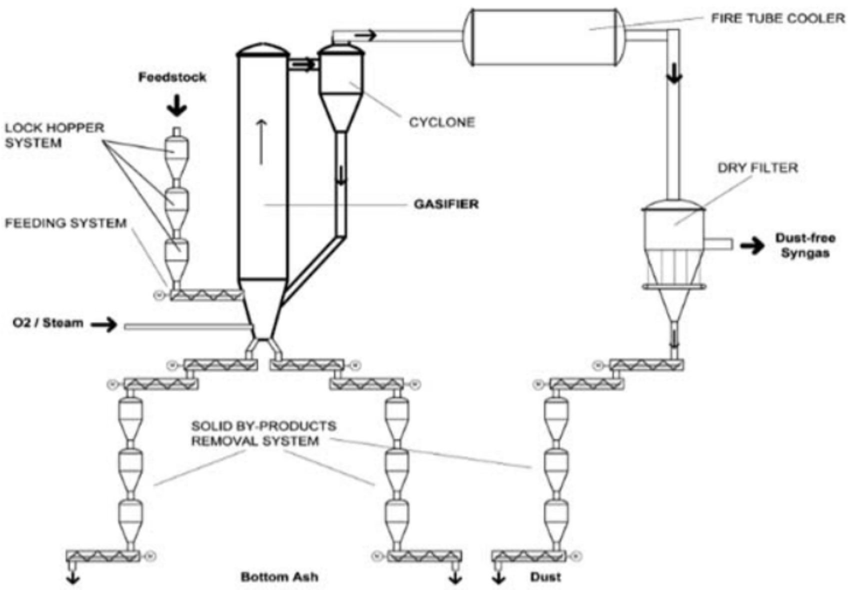

Figure 1.4: A simplistic depiction of the entire bubbling fluidized bed gasification process [34].

1.2.4. Operation of a Fluidized Bed Gasifier

A fluidized bed gasifier is characterized by two different zones, the fluidized bed and the post-gasification zone or freeboard. As can be seen in Figure 1.4, the feedstock enters the gasifier from its bottom part via screw conveyors and it is pyrolyzed, releasing its volatiles and forming a dense phase in the bottom of the reactor, which constitutes the fluidized bed zone. The reactions taking place in the bed are controlled by the input of gasification agents via nozzles along the height of the bed. From the bottom of the reactor, a part of the bed inventory is removed constantly to ensure ash removal and prevent its accumulation and obstruction of the reactor's operation. Moreover, the bed temperature must remain below the ash melting point — typically around 800–1000° C — which ensures that the bottom product is removed in solid form. It is also worth noting that this bottom product contains not only ash but also unconverted carbon, due to the effective mixing conditions within the bed [3].

Above the fluidized bed zone, there is the post-gasification zone, or also called freeboard (see Fig. 1.5), where a further reforming of tars or large hydrocarbons can take place, often achieved with the help of additional gasification agents. This zone is almost completely particle-free, except for a few particles that are entrained from the bed [16]. As gas bubbles move upwards through the fluidized bed, they reach the bed surface which leads to their bursting.

During the bubbles' ascent towards the bed surface, they cause the solids in the bed to move upwards as well, through two mechanisms: wake transport and drift transport. In reality, bubbles in the bed are not perfectly spherical, but they rather have a flat or even concave base. The wake, therefore refers to the region just below the bubble, which is formed due to the pressure at the lower part of the bubble being lower than the rest of the emulsion phase [35]. Due to this pressure difference, solids are being ”pulled up” behind the bubbles and therefore forming the wake region. Drift refers to solid particles that are loosely swept along by the movement of the bubbles [6].

The eruption of the bubbles once they reach the bed surface creates localized jets of gas that entrain solid particles into the space above the bed due to their momentum. The area above the bed surface is called the splashing zone, which is a transitional region between the fluidized bed and the freeboard. Depending on whether the fluid drag force acting on the particle is larger than its weight force, some of the particles will disengage from the gas and fall back into the dense bed or continue moving upwards with the gas and exit the freeboard. A specific height is defined, referred to as the Transport Disengaging Height (TDH), which marks the point beyond which almost no additional particles return to the bed. Therefore, beyond the TDH only very fine particles continue to be carried upwards by the gas and exit the freeboard, which constitutes a flux of particles called the elutriation rate [36].

As new gasification agents (i.e. steam or oxygen) enter through the freeboard nozzles, new combustion reactions take place and the temperature in the freeboard tends to increase significantly compared to the bed zone. In the freeboard, there are no limitations for the increase of the temperature, since there are almost no particles in this part of the gasifier, and therefore temperatures way above the ash melting point are observed (typically around 900 - 1200° C) [3]. This higher temperature profile helps the cracking of tar products and longer hydrocarbons that have reached the freeboard. At the top of the reactor, a cyclone receives the gasifier's product, separating the syngas from the entrained solids, and returning them to the fluidized bed of the gasifier so that they can be converted further (see also Fig. 1.4).

Figure 1.5 provides a simplistic depiction of a fluidized bed gasifier, consisting of the fluidized bed and the freeboard region, on top of it. The white circles inside the bed area represent the gas bubbles that are rising through the bed, growing in size, while the black dots represent the char particles produced after the feedstock undergoes pyrolysis.

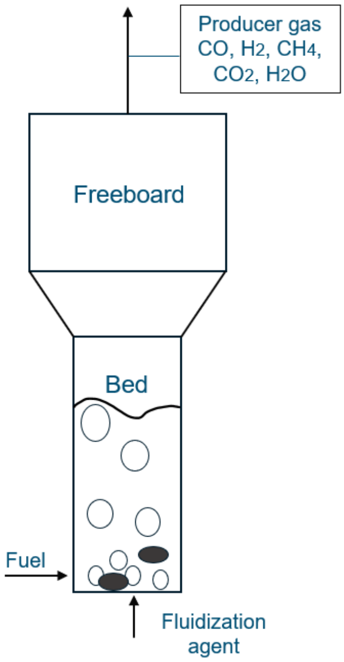

Figure 1.5: Simplistic depiction of the freeboard and the fluidized bed of a gasifier system

1.3. Thesis Outline

The structure of this thesis is organized into six chapters. Chapter 2 gives a comprehensive literature review, offering an overview of the existing research on 1-D modeling of bubbling fluidized bed gasifiers, with a specific focus on biomass or waste gasification processes. In addition, it discusses the identified research gaps and the research question that is addressed. Chapter 3 details the methodology that was followed in order to develop the gasification model, with a main focus on the use of the cell model and the empirical expressions that were used to formulate it. In Chapter 4, the model is validated by comparing its results with experimental data obtained from tests conducted in 2020 at the TU Darmstadt facility. What is more, several sensitivity analysis tests were also conducted, to assess how the model responds to certain varying parameters. Chapter 5 summarizes the conclusions drawn from the model validation, presenting the key findings of this study. Finally, Chapter 6 outlines potential directions for future research, suggesting areas for improvement in subsequent studies.

2

Literature Review

2.1. Different Modeling Approaches for Gasification

The gasification of solid fuels in a fluidized bed gasifier is a complex process to model due to the interaction of different phases (such as solid-gas and solid-solid interactions in the bed) [32]. There are usually 3 different types of gasification model approaches that are being used, them being [34]:

1. Black-box models (BBM): a 0-D (zero-dimensional) model, treating the entire gasifier as one big black box, solving for the overall mass and heat balances of the whole gasifier
2. Fluidization methods (FM): a 1-D model, which does not go deep into the details of solid-gas interactions but still considers a multiphase flow in the bed. The ”zone models”, which are a type of fluidization method, divide the gasifier into separate areas, such as the bed and the freeboard, or the emulsion and the bubble phase, and solve simplified balances for each zone, without CFD complexity.
3. Computational fluid dynamics methods (CFD-M): a 2-D or 3-D modeling approach, which takes into account the transport phenomena and the gas-particle, and even sometimes the particle-particle interactions.

2.1.1. BBM

A BBM is usually based on a chemical equilibrium model, meaning that it is assumed that chemical equilibrium is achieved at the exit of the gasifier. A chemical equilibrium model calculates the so-called ’ideal’ syngas composition, which would result if the participating substances had infinite time to react with each other [37]. An equilibrium model simulation predicts that there is no oxygen, tars or solid carbon left in the outlet stream, which is far from the truth (especially for the hydrocarbon and tar content), which shows that there is therefore a strong reaction kinetics limitation [34]. The only species that are assumed are H_2, CO, CO_2, CH_4, N_2 and H_2O, with the others being considered as negligible. The reactor is often assumed to operate under isothermal conditions and the syngas product to be under gasifier temperature [23]. In addition, the chemical equilibrium model does not offer any insights into the design of the gasifier and only considers the final syngas composition at equilibrium [32]. A chemical equilibrium model is basically based on the minimization of Gibbs free energy [19], and its outputs are the maximum theoretical gas yields for a specific set of operating conditions. These models require as input the elemental composition of the inlet feedstock, along with the reactor temperature and pressure, and solve for the equilibrium composition that minimizes the system’s total Gibbs free energy. It is mainly used for concept studies and for preliminary designs of a process [19], or for operations where the rates of chemical reactions taking place are very fast compared to the residence time of the reactants [23]. The lack of accuracy of these models has led to the development of more effective kinetic or CFD models. Of course, it should be noted that as the output quality and effectiveness of a model increases, so does its complexity and computational demand [37].

2.1.2. FM

The FM gasification approach is based mainly on the chemical reaction kinetics of the procedure. A model of this type takes into account the reactor geometry and can also flexibly incorporate a wider range of reactions, compared to the BBM approach [32]. The 1-D reaction kinetics model uses the assumption that the reactor is divided into a series of computational cells (or finite volumes) along the height of the reactor. Each cell consists of two different areas, the bubble phase, considered to be completely solid-free, and the emulsion or suspension phase. In the emulsion phase, which contains all the solids and some of the gases, the solid and gaseous phases co-exist and interact with each other, and the mixture is assumed to be perfectly mixed. Semi-empirical expressions are used to calculate the flow pattern of each phase in each cell, as well as the yields of the different gaseous substances and other relevant variables. A set of 1-D equations is solved for the calculation of mass and heat balances for each species along the height of the reactor, which leads to the derivation of the temperature profile and the distribution of the species. This method uses the kinetic data for the different types of reactions taking places, such as drying, pyrolysis, combustion and gasification, which need to be adapted to the specific type of feedstock used, and can be retrieved from literature sources or from experiments under similar operating conditions. It should be noted that a combination of chemical equilibrium and reaction kinetics model has also been attempted in different works [32].

2.1.3. CFD-M

CFD methods are based on more complex mathematical models, which consider and simulate the dynamic fluid flow, the chemical reactions, the turbulence and heat transfer, all typically described in a Eulerian approach; as well as the heterogeneous reactions, the mass, heat and momentum transfer in either a Lagrangian or a Eulerian approach [34].

The CFD approach, while widely applied for modeling the combustion or gasification of pulverized coal, its application to fluidized bed gasifiers is proving more challenging due to the inherent characteristic of high solid volume fraction in such systems. A flow that has a high particle density, in order to be modeled needs to include advanced modeling approaches that also account for particle-particle interactions [34]. Currently, various multiphysics and multiscale numerical models are available to model gasification processes, such as the the two-fluid model (TFM) [38], the computational fluid dynamics coupled with discrete element method (CFD-DEM) [39] and the multiphase particle-in-cell method (MP-PIC) [38]. The CFD-M approaches can also be distinguished based on the frameworks they utilize, in either Eulerian - Eulerian or Eulerian - Lagrangian [40].

The Eulerian - Eulerian TFM approach models both the gas and the solid phases as continuous flows, which is more computationally efficient than the other two aforementioned approaches [32]. Nevertheless, this method also faces some challenges, such as its trouble simulating flows with particle type and size distributions, because for each of these types and sizes separate mass and momentum balances need to be expressed [38].

The CFD-DEM numerical model is based on a Eulerian - Lagrangian theory, which implements the Eulerian method for the gas phase, but uses the discrete element method for the solid particle phase [39]. This method uses a very small time step, in its effort to solve for the particle collisions. Under this approach, every solid particle is tracked and its individual physical and thermochemical properties are calculated, which therefore requires quite a lot of computational power and time [32] [40].

The MP-PIC is a Eulerian - Lagrangian method, where the solid motion is described with the Lagrangian principles and assumes a computational particle that basically represents a group of particles sharing similar properties. This approach of grouping particles together improves the model efficiency when compared to the previous approach, clearly showcasing its better compatibility with industrial needs [32].

2.1.4. This work

It is evident that the CFD-M approaches offer greater details and deliver more accurate results than the BBM and FM approaches. However, they are significantly more computationally demanding and complex. Simulating just a few seconds of real-time operation can take up to several days on modern supercomputers to be completed, making them not so easily applicable to industrial applications [32]. Therefore, in this thesis project, an FM approach was selected to model the bubbling fluidized bed gasifier in one dimension.

2.2. Geldart's Classification of Solids

An important aspect to take into consideration when modeling a gasification process in a fluidized bed is the physical classification of the solid particles, found in the bed of the reactor. In 1973, Derek Geldart [41] submitted a paper to ”Powder Technology”, called ”Types of Gas Fluidization”, which supported the notion that the fluidization behavior can be dictated based on the density and the diameter values of the process [42]. Geldart had collected a number of fluidization data from various researchers, which were mainly empirical observations of the difference between the particle’s and the fluid’s density used in each process, as well as observations on the Sauter diameter of the particles. This research of Geldart led to the so-called ”Geldart classification”, which is currently a widely accepted framework, and is used to categorize solids based on their fluidization behavior under ambient air conditions in four main categories (A, B, C and D) The four Geldart groups can be characterized as follows: A – aeratable, B – bubbly, C – cohesive and D – spoutable [41].

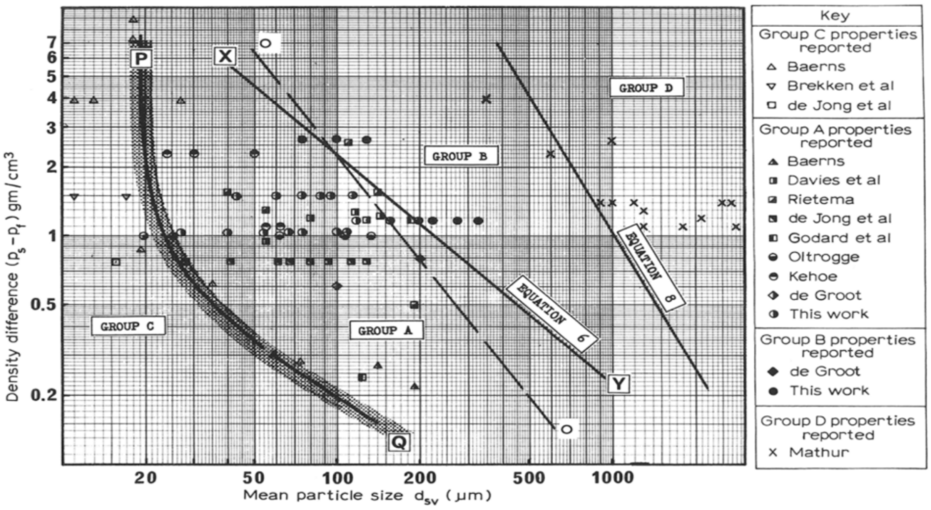

Figure 2.1: Geldart’s solid classification diagram for fluidization by air. [41]

Particles in Group A exhibit relatively good heat and mass transfer phenomena, which makes them a suitable candidate for fast and exothermic reactions [42]. In addition, the bubbles noticed in gasification processes with Group A particles are usually small, around 5 cm, and they do not form when the gas velocity reaches the minimum fluidization velocity u_{mf}, but rather when the gas velocity surpasses u_{mf} and becomes the so-called ”minimum bubbling velocity” u_{mb}. That is why, for particles of Group A, the dense phase seems to grow between minimum fluidization conditions and the beginning of bubble formation. Particles in Group A have particle density values of around 800-2000 kg/m^3 and diameters of approximately 45 to 150 μm [42] [41].

Group B particles have a larger size than that of Group A particles, ranging from about 150 - 1000 μm, leading to low cohesive behavior due to their large diameters. The use of particles from Group B in a fluidization process leads to the creation of significantly larger bubbles, especially compared to the ones when using Group A particles, as can also be seen in Fig. 2.2. To be more exact, bubbles in a fluidized bed of Group B particles continue to grow as they move forward, with no equilibrium bubble size being reported to exist [42]. In large-scale industrial systems, the bubble size can reach the order of meters, which can present significant challenges, as large bubbles can lead to slugging, which in turn can cause severe stresses on the reactor [43]. Sand is a typical Group B solid material.

Group C particles are the smallest in size, with a particle diameter less than 45 μm and a particle density of around 1200 kg/m^3. Group C particles are commonly called as ”fines”, due to their small size and also exhibit significantly cohesive behavior with a tendency to agglomerate. These particles are the hardest to fluidize, since the fluidization gas chooses to bypass the bed flowing through temporary channels [42].

Group D particles have large particle sizes, with values usually bigger than 1000 μm and are spoutable, meaning that they can cause the formation of a stable spout or a fountain-like flow pattern when gas is introduced from the bottom of a bed (see Fig. 2.2). One exception to the rule of large particles for Group D, is the case of particles smaller than 1000 μm but with very high density values (i.e. metal particles) [42]. One characteristic of the case of Group D particles is that they lead to high bed densities, which can significantly limit mixing and cause less effective gasification. Similarly to when Group B particles are used, the use of Group D particles can cause the creation of rather large bubbles, which have lower velocities. In this case, the gas velocity is higher than the rise velocity of the bubbles, with the gas flowing through the bubbles from bottom to top [44]. Because of the bigger size of the Group D particles, the gas flow needs to be rather high in order to manage to fluidize adequately the bed.

It is evident that the various solid classification groups display significantly different properties and fluidization behaviors. Therefore, it is important to understand in which Geldart group the bed particles belong to, as depending on the group, different modeling assumptions can be implemented (i.e. perfect mixing or gas bypassing).

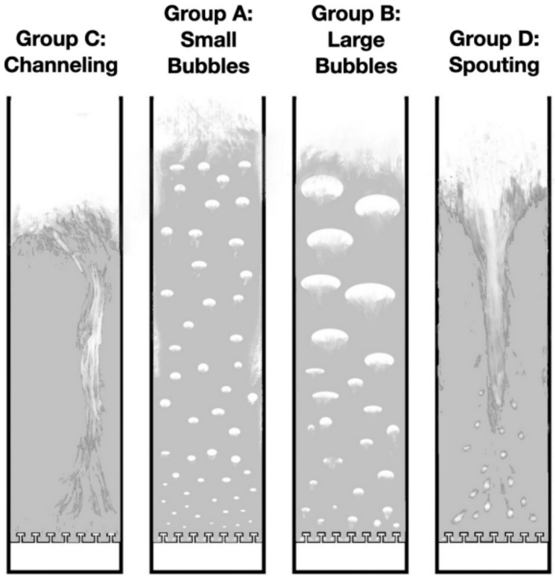

Figure 2.2: Schematic of the fluidization behavior of each Geldart Group of solids. [42]

2.3. Latest Developments on Gasification Modeling

Numerous researchers have attempted throughout the years to formulate their own models to simulate a fluidized bed gasification, with a variety of approaches developed to predict reactor behavior. These models can be grouped into several categories depending on their complexity and objectives.

2.3.1. Equilibrium and Simplified Models

Several researchers have implemented equilibrium models in order to predict the performance of fluidized bed gasifiers. For example, Li et al. (2004) [45] investigated the gasification of biomass in a circulating fluidized bed through both experimental testing and equilibrium modeling using an iterative algorithm. The authors studied the influence of several operational parameters on the final syngas product of a circulating fluidized bed, and concluded that the composition and heating value of the syngas exiting the gasifier depend greatly on the air-to-carbon or oxygen-to-carbon ratio, as well as the suspension temperature. They deducted that an air ratio with a value of around 0.2–0.3 is suitable for producing a syngas rich in CO, while a slightly lower air ratio of around 0.15-0.25 will lead to the producing of a H_2-rich syngas. Similarly, Masnadi et al. (2015) [18] modeled a co-gasification (gasification with two or more fuels used) procedure with switchgrass and coal in Aspen Plus [46], and discovered that the equilibrium model that they used was not able to predict the formation of CH_4 compounds adequately. The equilibrium studies can provide the modeler with a fast prediction of the final outcome, but they often lack in accuracy regarding the kinetic and transport phenomena taking place, which can be a significant limitation when dealing with complex feedstocks, such as waste or biomass. In addition, equilibrium models have also been found out to overestimate the presence of certain species in the final syngas (such as H_2 or CO), while underestimating others (such as CH_4) [47].

2.3.2. Kinetic and Unsteady-State Models

In the effort to deal with the limitations of the aforementioned equilibrium models, more detailed kinetic models have been developed. These kinetic models have implemented reaction kinetics as well as hydrodynamic expressions. Miao et al. (2014) [48] developed a 1-D biomass gasification model to predict the behavior of rice husk as fuel in a circulating fluidized bed, calculating the temperature distribution, the LHV of the final gas, the efficiency of the gasification and the composition of the syngas. Their model was able to reasonably predict the performance of circulating fluidized bed gasifiers at steady state, as it was validated with experimental results and data found in literature. Agu et al. (2019) [32] worked on a 1-D unsteady state model for biomass gasification in a bubbling fluidized bed, which utilized the Lagrangian approach to model the flow of solid particles and the Eulerian approach for the gas phase. They conducted a study on how the feedstock feeding position affects the final gas composition, and found out that a higher feedstock feeding position (closer to the bed surface) will lead to higher fractions of CO_2 and H_2, while it will decrease the conversion of char. Gamero et al. (2021) [47] also modeled a bubbling fluidized bed in Aspen Plus, gasifying biomass with air, while also including a kinetic mechanism to simulate its operation. Their model, which was validated against experimental data, managed to predict adequately the performance of the gasifier, under a set of different operating conditions (range of temperatures and equivalence ratios), but was overestimating the production of H_2. A major simplification of their model lies in their neglect of the hydrodynamics, which they also acknowledge in their paper. Gordillo et al. (2011) [49] developed a two-phase model to simulate the steam gasification of biomass char in a bubbling fluidized bed, using nuclear heat as the source of energy needed, with hydrogen being the principal product of the operation. Due to the nature of the heat used, there is no combustion reactions taking place, which limits significantly the product yield of the carbon dioxide. What is more, the authors also studied the effect of the Height-to-Diameter (H/D) ratio, and concluded that a high H/D leads to higher H_2 production. It should be mentioned that the authors in this paper consider only 4 reactions taking place in the reactor, while also neglecting the formation of tars, and only model the fluid dynamics for the bed, but not for the freeboard. Hejazi et al. (2016) [50] studied the gasification of biomass with steam in a dual fluidized bed reactor while also taking into account the solid circulation flux. The authors performed a sensitivity analysis with the steam-to-biomass ratio, and noticed that a low steam input led to the formation of less H_2 and more CH_4 in the product gas, which was also closer to the experimental results. Although the authors modeled the hydrodynamics for the fluidized bed, they omitted the freeboard region, as well as solids entrainment therein. Inayat et al. (2010) [51] studied the biomass steam gasification, while using calcium oxide as a sorbent, in order to produce a rich gas in hydrogen. They considered a gasification system integrated with a CO_2 absorption step, where implementing a mass ratio of 1.52 sorbent-to-biomass, they were able to produce a H_2 gas with 0.98 purity. The authors concluded that an increase in temperature and the steam-to-biomass ratio, can significantly increase the production of more hydrogen and the char conversion. It should be mentioned though, that the authors neglected to model the formation of tars as well as the hydrodynamics. Despite the higher complexity of the kinetic models (compared to the equilibrium models), due to the inclusion of necessary detailed information regarding the kinetic mechanisms taking place, the results of kinetic models are often found to be closer to experimental data [47].

2.3.3. Experimental Studies and Model Validation

In addition to the equilibrium and kinetic models, the experimental studies also offer significant input for model development and validation. Kim et al. (2013) [52] studied the air-blown gasification of biomass in a bubbling fluidized bed varying the amount of the gasification agents to examine their effect on the final product. They also noticed that a gasification unit with a longer freeboard and a fuel feeding from the top of the reactor led to the formation of more hydrogen. Pitkäoja et al. (2020) [53] developed a 1-D two-phase flow model for sorbent enhanced gasification (SEG) in a bubbling fluidized bed and validated it with experimental results from a test in a 200 kW_{th} pilot plant. They also assumed that the bed was not perfectly mixed and that the conversion rate of the bed material varies along the height of the reactor. The authors concluded that SEG holds a lot of promise for the production of renewable syngas, seeing as their model could adequately predict the hydrodynamics, temperature distribution and the syngas composition. However, the authors also noticed that the model didn't perform as well in low temperature ranges. Bhattacharya (2006) [54] examined the performance of Australian lignites in an bubbling fluidized bed gasification reactor, reaching a carbon conversion efficiency of around 70-87%, due to the elutriation (process where fine particles are carried out of the bed due to the upward gas flow) witnessed for the solid particles. Krause et al. (2019) [16] also studied the stationary bubbling fluidized bed gasification of high volatile coal, in the effort to determine the applicability of coal for this process.

2.3.4. Identified Research Gaps

Although there have been various studies on the modeling of gasification mechanisms, examining the reaction kinetics and hydrodynamics, as can be previously seen, literature gaps still remain. There are still several limitations and open research questions regarding the modeling of a bubbling fluidized bed gasifier with biogenic or waste-derived feedstock. First of all, the operation of a bubbling fluidized bed gasifier has still not been studied in depth when using biomass or waste-derived fuels as feedstock, with most models using coal as feedstock. Proper understanding of the behavior of waste or biomass in a bubbling fluidized bed, which would consider the diffusion effect, tar formation and cracking, kinetics and hydrodynamics, remains to be lacking [55] [56]. Second, the modeling of tar in the gasification of biogenic or waste-derived feedstock remains a significant challenge, as there is no common understanding on the most appropriate approach [57]. To be more exact, the downstream reactions of tars are often omitted in many studies, as was also confirmed in the literature review. Furthermore, char is often simplistically modeled as consisting solely of carbon, hence overlooking the presence of other compounds in it. Limited understanding of the catalytic effects of the bed material or the fuel ash in gasification reactions further complicates the modeling process, with the absence of catalytic activity frequently cited as a key factor contributing to discrepancies between experimental and simulation results [50]. In addition, most studies, even if they model the hydrodynamics of the process, focus primarily on the fluidized bed area, while the freeboard is often neglected [50] [49]. Lastly, there is a lack of findings on the secondary reactions taking place (especially with tars and light hydrocarbons) when biogenic or waste-derived feedstock is gasified and limited availability of trustworthy experimental data for the species involved in the secondary reactions, which however play an important role in the overall kinetic model of devolatilization and combustion reactions [58].

2.3.5. Research Question

Thus, considering the aforementioned issues and gaps, this thesis project specifically investigates ways to develop more representative 1-D simulations of a bubbling fluidized bed gasifier, by integrating detailed hydrodynamics, waste-specific kinetic mechanisms and nozzle effects in the bed and in the freeboard. Therefore, in order to do so, this thesis introduces several innovative elements:

(i) detailed hydrodynamic modeling of the entire fluidized bed gasifier (both the bed and the freeboard),

(ii) release and creation of tars from pyrolysis,

(iii) use of Python Cantera, in order to model region-specific chemical reactions taking place during the gasification of waste-derived feedstock,

(iv) validation of the model's results with experimental data from a gasification test with SRF in a pilot plant of a bubbling fluidized bed gasifier,

(v) sensitivity analysis tests, among which the testing of different kinetic parameters for the gasification reactions and evaluation of their effect for the final syngas composition.

Therefore, although previously mentioned, certain research gaps (such as the catalytic activity or the detailed modeling of char), remain out of the scope of this present work and are suggested for future research.

3

Model Development & Methodology

In this section, the methodology that was followed for the development of the bubbling fluidized bed gasifier cell model is described, listing all the key assumptions that were made, the most important equations that were used, as well as the idea and structure behind the numerical algorithm that was built in Python. The model used in this current thesis project is primarily based on the work of Hamel, as was presented in his doctoral thesis [4] [59], where he aimed to model mathematically a fluidized bed gasifier. This project aims to adapt and extend Hamel's model so that it includes chemical kinetics from the gasification of waste-derived feedstock, nozzle effects in the bed and the freeboard, as well as the use of Cantera. The general structure behind the cell-based model can be seen in Figure 3.1.

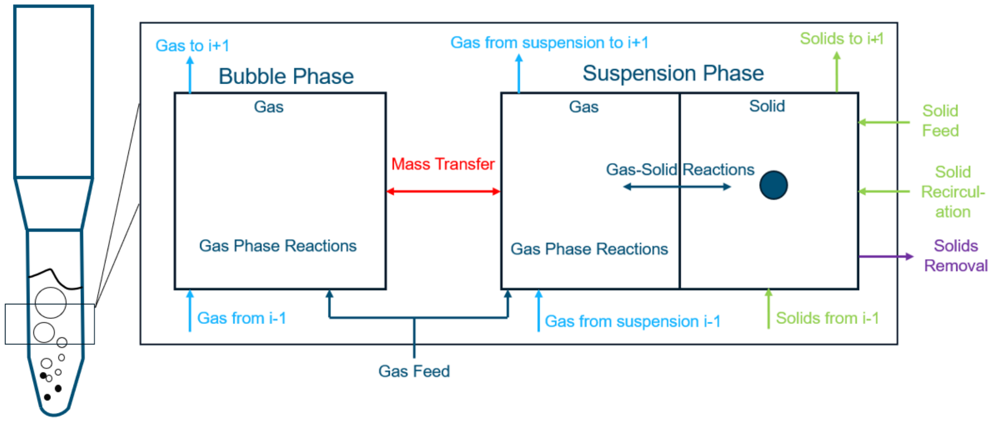

Figure 3.1: Schematic diagram of the general structure of the cell model.

3.1. List of Assumptions

1. The chemical reactions taking place in the gasifier (both homogeneous and heterogeneous) are modeled using Arrhenius-type kinetics equation, and are either first, second or third-order reactions based on the work of [32, 60, 61, 47, 62]. All the reactions are therefore considered to be kinetically limited, rather than mass-transfer limited, which is an assumption commonly found in literature [50]. A fluidized bed gasifier is generally characterized by intense particle movement and high mass transfer rates in the bed, which leads to low internal and external mass-transfer limitations, also due to the severe attrition that the char particles undergo [50], which makes it reasonable to assume that the rate-controlling mechanism in gasification reactions is the chemistry. However, it should be mentioned that char particles derived from biogenic feedstock can remain relatively large, which would lead to non-negligible mass transfer limitations for heterogeneous reactions involving char [63]. Nonetheless, the current model assumes that chemical kinetics are the rate-limiting mechanism.

2. Although the gasification reactions in the current model (both homogeneous and heterogeneous) are treated as kinetically limited using Arrhenius-type expressions, devolatilization is simplified and considered to be instantaneous upon fuel entry [64, 65, 24, 66]. To be more specific, P. Basu (2010) [67] states that the rate of gasification of char is significantly slower than the pyrolysis rate, while F. Prashanth et al (2024) [68] and C. Dupont (2008) [69] claim that pyrolysis can be achieved in less than 0.5 sec for particles of this size (0.4mm). Therefore, although pyrolysis is a reaction with its own kinetic mechanism, it is not explicitly modeled, but rather assumed to be complete at the moment of fuel injection.
3. The product yields obtained from the pyrolysis of the fuel are used as the initial conditions in the gasification reactions [56].
4. Tar, released during devolatilization, is assumed to comprise only of phenol (C_6H_6O), benzene (C_6H_6) and naphthalene ($C_{10}H_8$) [60].
5. Char, released during devolatilization, is assumed to comprise of pure carbon (C) in the gasification reactions, as is considered in most literature sources [60, 57, 70].
6. Contaminants like SO_2, H_2S, NOx, HCl, Cl_2 were considered to be negligible [60]. Therefore, the only chemical elements that were considered were C, H, O.
7. The gasification system is considered to be at steady-state, which implies that the feeding and removal rates of gaseous and solid compounds are constant in time [56, 47].
8. The model is one-dimensional, with changes occurring only in the axial direction. No variations of mass or temperature are considered in the radial axis [32].
9. The recirculation line of the gasifier setup (where solids are returned from the cyclone back to the reactor) is not modeled. This is reasonable given that the superficial gas velocity u_0 (see Section 3.5.2) is below the 0.5 m/s threshold, when significant solid entrainment begins to occur [30].
10. The bottom product removal rate was not modeled. This can be justified by the fact that the bottom product removal is not continuous, but rather intermittent based on certain parameters, such as the bed height inside the gasifier. Therefore, this falls outside of the scope of a steady-state modeling approach, that this project is following.
11. The bubble phase is considered to be completely free of solids [6].
12. In the bubble phase, only gas-gas chemical reactions occur, while in the suspension phase both heterogeneous and homogeneous reactions take place [24].
13. The gas feeding angles of the nozzles were not considered.
14. The entrance of the fuel feed was considered to be at the bottom of the reactor.
15. The gasification agents enter the reactor through the bubble phase [35, 67].
16. In each discretized cell of the reactor's length, solids and gases are assumed to be fully mixed [6], so uniform composition and temperature is assumed throughout the emulsion. Hence, no intraparticle or interphase concentration and temperature gradients exist within the emulsion phase at any axial location. In other words, the emulsion phase is treated as a ”pseudo-homogeneous” phase [71].
17. The products of the initial pyrolysis process are assumed to be completely allocated and uniformly distributed in the emulsion phase [72, 24].
18. Fluidization agent in the form of H_2O enters at the bottom of the reactor, as well as CO_2 to act as seal gas for the bottom product removal and hinder syngas from exiting through there.
19. Ash is assumed as chemically inert under the studied conditions due to the lack of kinetic data on the chemical properties of bed materials in the literature [56, 47].
20. The sphericity of the bed material particles (char and ash) was considered to remain constant and was assumed to be equal to 0.75 [6]. For further details on sphericity, refer to Section 3.3.4.
21. The porosity of the char particles was assumed to be 93%, based on the work of Yao et al (2022) [73], who measured the effective porosity of different raw and torrefied biomass particles [74, 75].
22. The expansion of the bed is considered to be negligible, consistent with literature findings [76].

23. The bubbles inside the fluidized bed are assumed to be of uniform size in a cell [24], but changing their size over the length of the bed.
24. Carbon C was modeled as a pseudo-gaseous species, due to software limitations (explained further in Section 3.3).
25. Each region of the reactor (the fluidized bed and the freeboard) is assumed to operate under isothermal conditions, with a fixed temperature in each zone. While in real-life applications, the temperature varies along the reactor due to the exothermic and endothermic reactions of the gasification model, this is not accounted for in the current model. As a result, no energy balance is solved.
26. The gases in the freeboard are assumed to be moving in plug-flow regime (Peclet numbers are high, also validated in Section 4.2) [50].

In Figure 3.2, a schematic diagram of the cell model can be seen, after the implementation of the aforementioned assumptions.

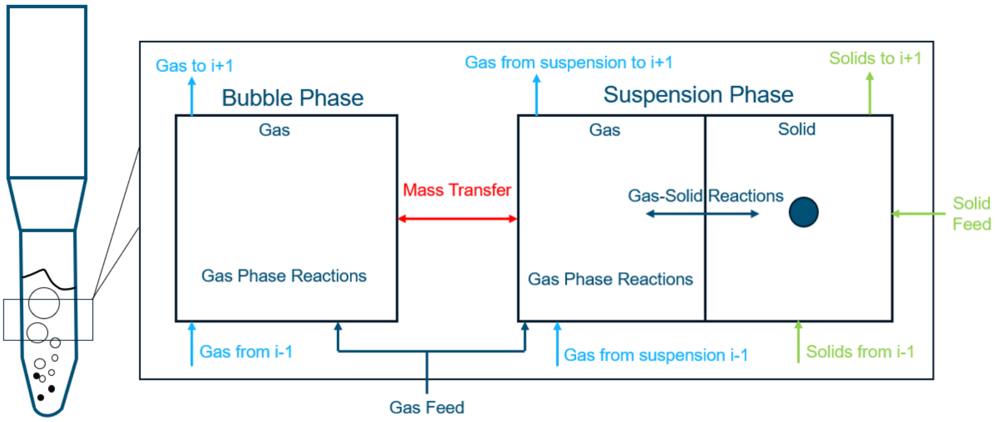

Figure 3.2: Schematic diagram of the structure of the cell model after applying assumptions.

3.2. Steps of the model

The present 1-D model of the bubbling fluidized bed gasifier is structured into several key steps which are listed and explained here, so as to provide clarity and guidance to the reader. In the beginning of Section 3.3.1, the emulsion phase, bubble phase and the freeboard kinetic mechanisms (modeled via Cantera) are explained. In Section 3.3.2, the devolatilization model is presented, which is applied on the incoming fuel and provides the feedstock composition used as input in later steps. In Section 3.3.3, the chemical kinetics of the reactions taking place are listed, which are applied on the outputs of the pyrolysis model. Afterwards, the hydrodynamics for the fluidized bed and the freeboard, describing the gas-solid flow behavior, are presented in Section 3.3.4. The mass balance model applied separately both for the fluidized bed and the freeboard is provided in Section 3.3.5, the algorithm of the model is detailed in Section 3.4, and finally, the geometrical and technical characteristics of the gasifier are listed in Section 3.5.1.

3.3. Mathematical formulation of the model

3.3.1. Modeling the emulsion, bubble and freeboard phases

The formulation of the problem in Python was carried out with the help of the Cantera Library [2]. Cantera is an open-source object-oriented software, used for simulating problems involving reaction kinetics, thermodynamics and transport processes. Cantera offers various object types or classes that represent different phases of matter, interfaces between phases, reactors, and steady-state one-dimensional reacting flows [2].

The first step was to define the feedstock into a form understandable by Cantera and create a new mechanism in a YAML file (a user-friendly format of storing information) that is then imported into the model, defining the substances considered and the chemical reactions that they participate in. Two separate reaction mechanisms were created to simulate the two distinct fluidized bed phases: the **emulsion phase** and the **bubble phase**. This phase-specific approach (regarding the construction of the two different mechanisms) was implemented so that a more accurate representation of each phase would be allowed, enabling an easier tracking of each phase's parameters (such as density, viscosity, mass fractions etc). In addition, another mechanism was created to simulate the gas species moving and reacting in the area above the bed, **the freeboard phase** (see Figure 1.5).

For more information on how the Cantera mechanisms were constructed, refer to Appendix A.

It should be noted that solid carbon (C) was modeled as a pseudo-gaseous species in Cantera, due to the software's limitations in handling gas-solid reactions. Cantera handles and processes reactions between gaseous and solid species through surface interfaces, which comes into contrast with how reactions actually take place in the whole volume of reactor's bed in a fluidized system. This makes modeling heterogeneous reactions in Cantera impractical. In order to address this issue, a decision was made to model solid carbon as a pseudo-gaseous species, which implies that the reactions between solid carbon and gases were modeled as gas-gas reactions, and carbon contributes to the properties of the emulsion phase gas and bubble phase gas that Cantera calculates internally. The main advantage of this decision is the simplification it introduced to the model, since Cantera now only considers a single-phase environment, while also uses the standard ODEs to track carbon. On the other hand, the decision to model carbon as a pseudo-gaseous species leads to the neglect of important carbon properties, such as the particle size, or the behavior of solids within the bed. In addition, in real gas-solid reactions, there are diffusion limitations, which are not taken into account in this model. Therefore, an overestimation of the reaction rates of char gasification might be possible. Lastly, solids contribute differently to properties like enthalpy or density, than if they were gases. Despite all the drawbacks of this decision, the choice to proceed with modeling solid carbon as a pseudo-gaseous species is considered a reasonable one, given that the main focus of this project lies mainly on the syngas trends, and less on investigations of the chemical kinetics and solids trends.

3.3.2. Pyrolysis Sub-Model

Describing the pyrolysis process is quite a challenge, as it contains a lot of physical and chemical transformations and releases a wide range of species. Therefore, the existing pyrolysis models that predict the release rates of the product species rely on empirical data [77, 60].

Pyrolysis of SRF feedstock

Although the initial model of this thesis was intended to operate on biomass feedstocks, this work focuses on the use of SRF, due to its increasing social and technological relevance and its limited representation in literature. For the validation of the model with experimental data, the campaign conducted by TU Darmstadt using SRF was selected as a reference [3]. Therefore, an empirical pyrolysis model developed for SRF is implemented [60], which was based on a feedstock of municipal plastic waste and is applicable for a range of pyrolysis temperatures between 650 - 950 ° C. The pyrolysis model of SRF is however more simplified than the pyrolysis models available for biogenic feedstocks, as it primarily uses the temperature as input. In any case, the biomass pyrolysis model is retained in the contents of this thesis for potential future use by other readers and it is explained in detail in Appendix C.

Based on the empirical model of [60], the mass yield (Y_i) (in %) of the pyrolysis products is given as a function of temperature T (in ° C) (see Equation 3.1 - Equation 3.6), which is also the only input to the SRF pyrolysis model:

$$Y_{\mathrm{CO_2}} = -1.82 \times 10^{-4}\, T^2 + 0.28\, T - 101.80 \tag{3.1}$$

$$Y_{\mathrm{CO}} = 1.69 \times 10^{-2} \cdot \exp(7.30 \times 10^{-3}\, T) \tag{3.2}$$

$$Y_{\mathrm{CH_4}} = -1.435 \times 10^{-3}\,T^2 + 0.23\,T - 85.45 \tag{3.3}$$

$$Y_{\mathrm{H_2}} = 2.00 \times 10^{-5} \cdot \exp(13.40 \times 10^{-3}\,T) \tag{3.4}$$

$$Y_{\text{char}} = -1.610 \times 10^{-2}\,T + 47.83 \tag{3.5}$$

$$Y_{\text{tar}} = -4.340 \times 10^{-2}\,T + 76.15 \tag{3.6}$$

Since the pyrolysis model does not explicitly provide the individual pyrolysis product yield for each tar species (i.e. $C_{10}H_8$, C_6H_6, C_6H_6O), the total tar pyrolysis product yield (derived from Equation 3.6) was evenly distributed among the three major tar species considered in this study.

Regarding the tar pyrolytic products, their elemental composition is expressed by Equation 3.7 - Equation 3.9:

$$Y_{\mathrm{C,\,tar}} = 5.91 \times 10^{-4}\,T + 0.24 \quad (R^2 = 0.96) \tag{3.7}$$

$$Y_{\mathrm{O,\,tar}} = -3.51 \times 10^{-3}\,T + 0.45 \quad (R^2 = 0.89) \tag{3.8}$$

$$Y_{\mathrm{H,\,tar}} = -2.40 \times 10^{-4}\,T + 0.307 \quad (R^2 = 0.92) \tag{3.9}$$

General Pyrolysis Assumption

As previously mentioned in the assumptions list, the products of the pyrolysis process are assumed to be allocated completely to the emulsion phase [72], and are treated as the initial conditions for the gasification model that is applied afterwards. This is a valid modeling approach, since pyrolysis is significantly faster than gasification. On the other hand, the bubble phase is assumed to be initialized as CO_2 which enters from the bottom of the bed, acting as a seal gas. The reason behind this decision lies on the fact that the incoming feed-rate of CO_2 is a known input, and it is introduced entirely through the bed's bottom, where bubbles are first formed.

3.3.3. Gasification Sub-Model

In Table 3.1, all the reactions that were considered in this model are described, as well as their reaction kinetics expressions [32, 60, 61, 47, 62].

The emulsion phase mechanism, as previously mentioned, contains the heterogeneous reactions taking place between the solid char and the gaseous species that are released, as well as the homogeneous reactions between the gaseous species. Therefore, the reactions that are included in the emulsion phase mechanism are R1 - R16. Similarly, for the freeboard phase mechanism, the same set of reactions is considered (R1 - R16). On the other hand, the bubble phase mechanism includes only homogeneous gas-phase reactions, which can occur in fast moving gas bubbles. This includes the reactions R2, R3, R4, R8 and R9.

Initially, the "plastic-gasification" model from the study of Bhattarai et al. [60] was used in its entirety for the description of the reaction kinetics of the gasification process, which was based on a feedstock of municipal waste, consisting of a blend of eight different plastic materials. However, as it will also be discussed in Section 4.7, this kinetic model did not seem to capture accordingly the characteristics of some reactions, especially the homogeneous ones, and therefore, a new set of kinetics was applied [62]. In the study of [62], the derived kinetics were empirically fitted to the gasification process of a biomass feedstock, and more specifically poplar sawdust. The final set of reaction kinetics that was implemented in the model can be seen in Table 3.1.

The input to this model is the output of the pyrolysis sub-model, after Cantera internally calculates the corresponding species concentration c_i in kmol/m^3 based on Equation 3.10:

$$c_i = \frac{\rho \cdot Y_i}{MW_i} \tag{3.10}$$

where Y_i is the mass fraction of each pyrolysis product, ρ the gas density (kg/m^3) and MW_i the molecular weight of each species (kg/kmol).

Table 3.1: Chemical reactions involved in the gasification process and their reaction rate expressions [60].

Reactions	Oxidation/Reduction Reactions	Rate expression (kmol/m^3/sec)
R1	$\alpha\,\mathrm{C}(s) + \mathrm{O_2} \rightarrow 2(\alpha - 1)\,\mathrm{CO} + (2 - \alpha)\,\mathrm{CO_2}$	$r_1 = 7.43 \cdot 10^5 \cdot T \cdot \exp\left(\frac{-1.21 \cdot 10^5}{RT}\right) \cdot [\mathrm{C}] \cdot [\mathrm{O_2}]$, $\alpha = \frac{4}{3}$ [60]
R2	$\mathrm{CO} + 0.5\,\mathrm{O_2} \rightarrow \mathrm{CO_2}$	$r_2 = 1.78 \cdot 10^{10} \cdot \exp\left(\frac{-1.8 \cdot 10^5}{RT}\right) \cdot [\mathrm{CO}] \cdot [\mathrm{O_2}] \cdot [\mathrm{H_2O}]$ [60]
R3	CH_4 + $0.5O_2$ → CO + $2H_2$	$r_3 = 5.15 \cdot 10^5 \cdot \exp\left(\frac{-2.20 \cdot 10^5}{RT}\right) \cdot [CH_4] \cdot [O_2]$ [60]
R4	H_2 + $0.5O_2$ → H_2O	$r_4 = 1.08 \cdot 10^7 \cdot \exp\left(\frac{-1.25 \cdot 10^5}{RT}\right) \cdot [H_2] \cdot [O_2]$ [60]
R5	C_6H_6O + $4O_2$ → 6CO + $3H_2O$	$r_5 = 655 \cdot T \cdot \exp\left(\frac{-80{,}200}{RT}\right) \cdot [C_6H_6O]^{0.5} \cdot [O_2]$ [62]
R6	C_6H_6 + $4.5O_2$ → 6CO + $3H_2O$	$r_6 = 0.56 \cdot 10^5 \cdot \exp\left(\frac{-1.17 \cdot 10^5}{RT}\right) \cdot [C_6H_6] \cdot [O_2]$ [60]
R7	C + H_2O → CO + H_2	$r_7 = \frac{k_1 P_{\mathrm{H_2O}}}{1 + k_2 P_{\mathrm{H_2O}} + k_3 P_{\mathrm{H_2}}}$ $k_1 = 4.93 \cdot 10^3 \exp\left(\frac{-18522}{T}\right)$ $k_2 = 1.1 \cdot 10^1 \exp\left(\frac{-3548}{T}\right)$ $k_3 = 1.53 \cdot 10^{-9} \exp\left(\frac{25161}{T}\right)$ [62]
R8	CO + H_2O ↔ CO_2 + H_2	$r_8 = 2.78 \cdot 10^2 \cdot \exp\left(\frac{-12{,}600}{RT}\right) \cdot \left([\mathrm{CO}] \cdot [\mathrm{H_2O}] - \frac{[\mathrm{H_2}] \cdot [\mathrm{CO_2}]}{K_{\mathsf{EQ}}}\right)$ $K_{\mathsf{EQ}} = 0.022 \exp\left(\frac{34730}{RT}\right)$ [47]
R9	CH_4 + H_2O ↔ CO + $3H_2$	$r_9 = 3 \cdot 10^8 \cdot \exp\left(\frac{-1.25 \cdot 10^5}{RT}\right) \cdot [CH_4] \cdot [H_2O]$ [62]
R10	C + CO_2 ↔ 2CO	$r_{10} = 4.36 \cdot 10^3 \cdot \exp\left(\frac{-248123}{RT}\right) \cdot [C] \cdot [CO_2]$ [60]
R11	C_6H_6O → CO + $0.4C_{10}H_8$ + $0.15C_6H_6$ + $0.1CH_4$ + $0.75H_2$	$r_{11} = 2.92 \cdot 10^5 \cdot \exp\left(\frac{-3.74 \cdot 10^5}{RT}\right) \cdot [C_6H_6O]$ [60]
R12	C_6H_6O + 2 H_2O → 3CO + C_2H_4 + CH_4 + H_2	$r_{12} = 1 \cdot 10^7 \cdot \exp\left(\frac{-1 \cdot 10^5}{RT}\right) \cdot [C_6H_6O]$ [62]
R13	$C_{10}H_8$ → 6.5C + $0.5C_6H_6$ + $0.5CH_4$ + $1.5H_2$	$r_{13} = 2.61 \cdot 10^5 \cdot \exp\left(\frac{-2.88 \cdot 10^5}{RT}\right) \cdot [C_{10}H_8] \cdot [H_2]$ [60]
R14	$C_{10}H_8$ + 10 H_2O → 14 H_2 + 10 CO	$r_{14} = 1 \cdot 10^{11} \cdot \exp\left(\frac{-3.24 \cdot 10^5}{RT}\right) \cdot [C_{10}H_8]$ [61]
R15	C_2H_4 + 2 H_2O → 4 H_2 + 2 CO	$r_{15} = 3 \cdot 10^8 \cdot \exp\left(\frac{-1.25 \cdot 10^5}{RT}\right) \cdot [C_2H_4] \cdot [H_2O]^2$ [62]
R16	C + 2 H_2 → CH_4	$r_{16} = 6.11 \cdot 10^{-3} \cdot \exp\left(\frac{-80{,}333}{RT}\right) \cdot [C][H_2]$ [32]

As previously mentioned, the formation of tars during pyrolysis was also considered in this model, and so the reactions (R5, R6, R11, R12, R13, R14, R15), representing key gasification and oxidation reactions of the tar species, were added, along with their reaction kinetics.

The Reactions R2 and R13 from Table 3.1 are called third-body reactions, since their reaction rate expressions features a species that does not participate in that reaction (H_2O for R2 and H_2 for R13). These reactions needed to be modeled slightly differently in the YAML environment, specifying their type as ”three-body” and the efficiency of the third-body species [78].

The heterogeneous reactions between solids and gas (like R7, or R10 from Table 3.1) can be based on the bulk cell concentrations and properties, since fast and perfect mixing is assumed for the emulsion phase in each cell. Therefore, conditions such as the interphase resistance are not considered and there is no need to model the individual particle conversion.

3.3.4. Hydrodynamic Sub-Model

This Subsection delves into the hydrodynamic sub-model used to express the fluid dynamic parameters for both the fluidized bed and the freeboard areas of the gasifier. The results of the hydrodynamic sub-model are used as inputs in the mass balance model, explained further in Subsection 3.3.5, as they are used to define the convective mass flow rates and the mass exchange terms between the two phases in the bed.

The most important parameters of the hydrodynamic sub-model are the:

- Velocity of gas in the emulsion (u_d)
- Bubble velocity (u_b)
- Porosity (gas volume fraction) in the emulsion phase (ϵ_d)
- Bubble volume fraction (ϵ_b) in the bed
- Bubble diameter (d_b) and its evolution along the bed height

3.3.4.1. Fluidized Bed

Each cell of the fluidized bed system was split into two different phases, the bubble phase, which was considered to be completely solid-free, and the dense or emulsion phase, which consists of solids and gas, that is flowing through the solids. This model is called a "2-phase theory" model and can be seen in Figure 3.3. For each cell, the hydrodynamic, kinetic and thermodynamic parameters were calculated.

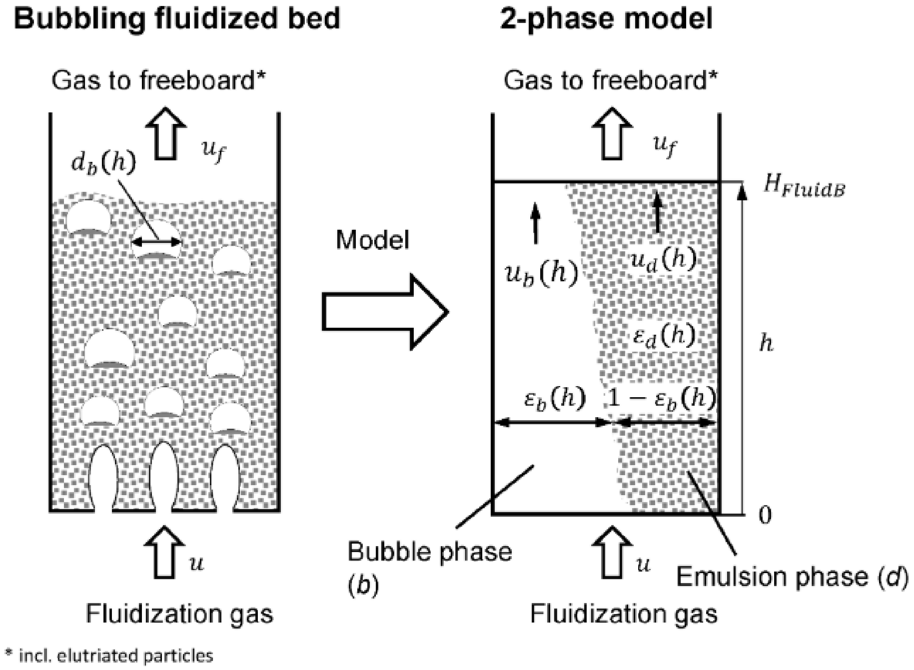

Figure 3.3: Scheme depicting the 2-phase theory in a bubbling fluidized bed [6]

It should be noted that not all gases behave in the same way inside the bubbling fluidized bed of the gasifier. To be more specific, we consider 3 main mechanisms of gas flow inside the bed [4]:

1. Visible Gas Flow (Dominant)
2. Flow Through and Around Bubbles (Dominant)
3. Flow Through Suspension / Back-mixing (Minor but Crucial)

The visible gas flow refers to the large visible bubbles that move upwards through the bed. These bubbles rise fast and carry a lot of gas, hence being considered as a dominant flow regime. Since bubbles are considered to be free of solids, they have very poor gas-solid contact. Therefore, this gas flow regime is inefficient for char conversion reactions.

The flow through and around the bubbles is another dominant regime. The flow through the bubbles refers to gas that is transferred from the bubble into the emulsion phase and reverse, based on the concentration gradients. On the other hand, the flow around the bubbles refers to the circulation and mixing of the emulsion phase gas that is caused due to the bubbles rising and causing the displacement of solids around them. This mechanism is very important, since it significantly helps the mass transfer between solids and gas.

Lastly, the flow through the suspension phase refers to the gas that moves slowly through the packed bed of solids. This slow movement allows enough time for the char reactions and tar cracking to take place, since they need more time to overcome the gas-solid diffusion limitations that are a typical characteristic of heterogeneous reactions. Although the majority of gas moves through the bed in the form of bubbles, this mechanism is responsible for the char conversion efficiency. In addition, the flow through the suspension phase can lead to back-mixing of the gas within the dense phase due to solids circulation, which can increase the uniformity of the bed.

Minimum Fluidization Velocity and Voidage

As previously mentioned, for fluidization to take place, the fluidization gases need to reach a velocity of u_{mf}, which is called the minimum fluidization gas velocity. At the velocity u_{mf}, the bed voidage ϵ_{mf}, which represents the gas volume fraction in the bed at that specific velocity can be calculated using the empirical Equation 3.11 from Gibson (2018) [79]. It should be noted that the subscript ”mf” refers to conditions at minimum fluidization.

$$\frac{(1-\epsilon_{mf})}{\phi^2\epsilon_{mf}^3} = 12.2 \pm 0.4 \tag{3.11}$$

As stated in the assumptions list, the value for the sphericity ϕ was assumed to be 0.75 [6], which through Equation 3.11 led to an ϵ_{mf} value of 0.435. Sphericity reflects how close to a perfect sphere is an actual solid particle. It is defined as the ratio between the surface area of a sphere that has the same volume as the particle, and the actual surface area of the particle. For a non-spherical particle, the sphericity will be less than 1 [80].

When modeling some solid fuels like coal, the assumption of a particle’s sphericity as close to unity has been a valid and reasonable approach, according to literature sources. When it comes to other types of fuels though, such as lignocellulosic biomass or SRF, which is the feedstock considered in the current model, this assumption does not stand. Biomass- and waste-derived char particles tend to have an elongated shape [81], their shape being characterized as ”needle-like”, with a large aspect ratio [82]. In the current model, a sphericity value of 0.75 was considered for the bed particles, based on the work of Beirow et al. [6] for biomass-derived fuel, which can also be supported by other literature data [83].

For the calculation of u_{mf}, the Ergun Equation is used (see Equation 3.12), which uses the definitions of the Archimedes (Ar) (see Eq. 3.13) and Reynolds numbers (Re) (see Eq. 3.14), and also the Sauter diameter (d_{sv}) (see Eq. 3.15) [6].

$$Ar = 150\frac{1-\epsilon_{mf}}{\phi^2\epsilon_{mf}^2} \cdot Re_{mf} + \frac{1.75}{\phi\epsilon_{mf}^3} \cdot Re_{mf}^2 \tag{3.12}$$

The Archimedes number is a dimensionless number and it is defined as the ratio of gravitational forces to viscous forces acting on a body (the solid particles in the current case) moving inside a fluid, where ρ_p refers to the solid particle density and ρ_g refers to the density of the gas in the emulsion phase of the fluidized bed.

$$Ar = \frac{g \cdot d_p^3}{\nu_g^2} \cdot \frac{\rho_p - \rho_g}{\rho_g} \tag{3.13}$$

The Reynolds number at minimum fluidization velocity (Re_{mf}) is a dimensionless number, which represents the ratio between the inertial forces and the viscous forces, acting on a body moving inside a fluid, where d_p is the particle diameter, u_{mf} is the minimum fluidization velocity, and ν_g is the kinematic viscosity of the gas in the emulsion phase.

$$Re_{mf} = \frac{d_p \cdot u_{mf}}{\nu_g} \tag{3.14}$$

The Sauter diameter d_{sv} represents an average value for the solid particle size, or more specifically, it represents the diameter of a sphere that has the same volume-to-surface area ratio as the specific particle of interest [72]. Equation 3.15 constitutes an empirical relation for the calculation of the Sauter diameter, based on the sphericity of the specific particle ϕ and d_p its diameter [6].

$$d_{sv} = \sqrt{\phi} \cdot d_p \tag{3.15}$$

The velocity and voidage at minimum fluidization (u_{mf} and ϵ_{mf} respectively) will then be used to calculate the gas velocity and the voidage in the emulsion phase (u_d and ϵ_d).

Emulsion Phase Velocity and Voidage

The dense phase is characterized by a gas velocity u_d and a porosity ϵ_d, which basically describes the void fraction in the dense phase. Note that the subscript "d" refers to the dense or emulsion phase.

Regarding the velocity of the gas in the dense phase u_d, the Equation 3.16 was used, as stated in the study of Kunii and Levenspiel [35] for fluidized beds with Geldart-B or Geldart-D particles, which calculates the emulsion gas velocity u_d as a function of the superficial gas velocity u_0 and the minimum fluidization velocity u_{mf}.

$$u_d = u_{mf} + \frac{1}{3} \cdot (u_0 - u_{mf}) \tag{3.16}$$

The void porosity ϵ_d is calculated by Eq. 3.17, as proposed by Hilligardt [84] and Richardson and Zaki [85]. The void porosity represents the volume fraction of the emulsion phase occupied by gas, therefore how much of the emulsion phase is filled with gas, instead of solid particles. The solid volume fraction of the emulsion phase is hence reflected by (1 - ϵ_d). Equation 3.17 shows how the porosity of the emulsion phase increases with the gas velocity u_d.

The exponent n_{RZ}, also called the Richardson-Zaki exponent, represents the effect of the drag force acting on a particle moving inside a fluid (through the Reynolds number of a settling particle (Re_s)) on the porosity of the emulsion phase. The empirical Equation 3.18 shows that as the Reynolds number increases and the inertial forces acting on a particle dominate over the viscous ones, and the drag force decreases, the n_{RZ} decreases, leading to a higher porosity in the emulsion phase. Following the same logic, for fluids with high viscosity, where the Reynolds number is low, there is a higher drag force acting on the particles inside the fluid, which in turn leads to a lower porosity.

$$\epsilon_d(h) = \epsilon_{mf} \left(\frac{u_d(h)}{u_{mf}} \right)^{\frac{1}{n_{RZ}}} . \tag{3.17}$$

$$n_{RZ} = \begin{cases} 4.65, & \text{if } Re_s \leq 0.2 \\ 4.4 \cdot Re_s^{-0.03}, & \text{if } 0.2 \leq Re_s \leq 1 \\ 4.4 \cdot Re_s^{-0.1}, & \text{if } 1 \leq Re_s \leq 500 \\ 2.4, & \text{if } Re_s > 500 \end{cases} \tag{3.18}$$

The Reynolds number of a sinking particle (Re_s) (see Eq. 3.19) is formed with the sinking or settling speed of the individual particle (u_s).

$$Re_s = \frac{u_s \cdot d_p \cdot \rho_g}{\mu_g} \tag{3.19}$$

The settling velocity of a particle inside the fluidized bed is calculated by solving the force balance for a single particle moving inside a fluid [4]. This leads to the Equation 3.20.

$$u_s = \sqrt{\frac{4 \cdot g \cdot d_p \cdot (\rho_p - \rho_g)}{3 \cdot \rho_g \cdot c_w}} \tag{3.20}$$

The drag coefficient c_w seen in Equation 3.20, is calculated through Equation 3.21, as described by Bürkle (1991), Dersch (1994), and Heinbockel (1995) who used the approach of Martin (1984) [4].

$$c_w = \frac{1}{3} \cdot (\sqrt{\frac{72}{Re_s}} + 1)^2 \tag{3.21}$$

Using the Equation 3.21 for the drag coefficient and Equation 3.19 for the Reynolds number, the Equation 3.20 is transformed into Equation 3.22, expressing the particle settling velocity as:

$$u_s = 18 \cdot \frac{v_g}{d_p} \left(\sqrt{(1 + \frac{1}{9} \cdot \sqrt{Ar})} - 1 \right)^2 \tag{3.22}$$

The voidage in the emulsion phase ϵ_d will then be used to calculate parameters used to compute the bubble velocity u_b, while the gas velocity in the emulsion phase is needed to calculate the bubble volume fraction ϵ_b.

Bubble Phase Velocity and Bubble Volume Fraction

The bubble rise velocity u_b is calculated using Eq. 3.23, proposed by Werther for Geldart B particles and bed diameters smaller than 1 m [35].

$$u_b = 1.6 \cdot ((u_0 - u_{mf}) + 1.13 \cdot d_b^{1/2}) \cdot D_{bed}^{1.35} + u_{b,i} \tag{3.23}$$

Equation 3.23 takes into account the diameter of the fluidized bed D_{bed}, the bubble diameter d_b, the superficial gas velocity u_0, the minimum fluidization velocity u_{mf} and lastly the rise velocity of the individual bubble $u_{b,i}$.

It should be noted that there are a lot more expressions for the bubble velocity in the literature, such as the one proposed by Davidson and Harrison, based on the two-phase theory, $u_b = u_0 - u_{mf} + 0.711 \cdot \sqrt{g \cdot d_b}$ [35],or $u_b = \Psi_b \cdot (u_0 - u_{mf}) + v_b \cdot u_{b,i}$, proposed by Hamel [4], but the decision was made to follow Equation 3.23 as it is specifically for Geldart B particles.

The parameter $u_{b,i}$, which corresponds to the rise velocity of an isolated individual bubble, can be described by Eq. 3.24, derived by Davidson and Harrison on the basis of the two-phase theory [35]:

$$u_{b,i} = 0.711 \cdot (g \cdot d_b)^{1/2} \tag{3.24}$$

Regarding the calculation of the bubble volume fraction in the reactor ϵ_b, the following formula was used (see Eq. 3.25):

$$\epsilon_b = \frac{u_0 - u_d}{u_b + n_b u_d - u_d} \tag{3.25}$$

, where the relative bubble velocity factor n_b is equal to 2.7, according to experiments conducted by Hilligardt [4]. The n_b factor represents how much faster the bubbles rise through the bed, in comparison to the gas of the emulsion phase.

Based on the results for the bubble volume fraction (ϵ_b), bubble velocity (u_b), gas velocity and voidage in the emulsion phase (u_d and ϵ_d), and the minimum fluidization velocity (u_{mf}), the bubble diameter evolution is then able to be calculated.

Bubble Diameter Evolution

Regarding the bubble diameter, Eq. 3.26 expresses the average bubble diameter along the height of the fluidized bed [86]. This expression is applicable for deep fluidized beds, where the ratio of the height of the bed over the bed diameter is larger than 2, which is applicable for the setup used for validation in this project (further detailed in Section 3.5.1).

$$d_b = 0.848 \cdot (u_0 - (\frac{u_0}{u_{mf}})^{0.62} \cdot u_{mf})^{0.66} \cdot D_{bed}^{0.34} \tag{3.26}$$

This bubble diameter expression takes into account the size of the gasifier, which many other expressions omit to do [4]. This expression also manages to successfully capture the bubble diameter size in both a bubbling and a slugging regime, with only minor modifications needed to be made, such as on the exponents of the parameters.

3.3.4.2. Freeboard

In the freeboard, the region above the dense bed, several important hydrodynamic mechanisms take place due to the interaction between gas bubbles, entrained particles, and gas flow.

Particle Movement in the Freeboard

The solid particles that are thrown upwards into the freeboard due to the bursting of bubbles when the latter reach the bed surface have an initial velocity, the particle starting speed. The mean particle starting speed is given by Eq. 3.27 [4]:

$$\bar{u}_{p,0} \approx 1.53 \cdot u_b \tag{3.27}$$

Regarding the discharge of solids into the freeboard, there is a broad agreement among the research community about the processes that occur when a single bubble reaches the bed surface and erupts. When the ascending bubble pierces the surface, a ”roof” of solid particles gets formed above the bubble [4]. This roof of particles remains in its place until the bubble reaches a height above the bed equal to the bubble’s diameter, when the latter bursts and solids get thrown into the freeboard. The other mechanism that contributes to the discharge of solid particles into the free space above the bed is the wake mechanism [4], that was previously explained in Section 1.2.4.

There are different types of solids that can be found in the freeboard section of a fluidized bed gasifier, with the main ones being unconverted carbon (char particles), inert materials (such as ash or the bed material) [87] and catalyst particles [35]. In the present model, since there is no external bed material considered and no use of a catalyst, the solid particles refer to unconverted char and inert ash particles. Therefore, even if there is a complete char conversion in the bed, solid particles (mainly ash) are still present in the freeboard.

Regarding the flow of the entrained particles in the freeboard, their equation of motion is derived from a balance of the forces acting on an individual particle (see Eq. 3.28 and 3.29 - 3.32 for the individual forces’ definitions). More specifically the forces acting on an entrained particle are the inertia force F_T, the buoyancy force F_A, the gravitational force F_G and the drag force F_W.

$$F_T + F_A + F_G + F_W = 0 \tag{3.28}$$

, where

$$F_T = -\rho_p \cdot V_p \cdot \frac{du_p}{dt} \tag{3.29}$$

$$F_A = \rho_g \cdot V_p \cdot g \tag{3.30}$$

$$F_G = -\rho_p \cdot V_p \cdot g \tag{3.31}$$

$$F_W = -c_W \cdot \rho_g \cdot \left(\frac{\pi \cdot d_p^2}{4}\right) \cdot \left(\frac{(u_p - u_g)|u_p - u_g|}{2}\right) \tag{3.32}$$

The V_p in Equations 3.29, 3.30 and 3.31 refers to the volume of a single particle, u_p is the velocity of the particles and u_g represents the velocity of the gaseous species in the freeboard (it will be explained further down in more detail).

It should be noted that the direction of the drag force F_W is determined based on the relative speed between the particle and the gas. If the particle moves faster than the surrounding gas ($u_p > u_g$) or it is falling ($u_p < 0$), the drag force acts in the opposite direction of the inertia force F_T and of the particle's motion. On the other hand, if a particle is rising but moving slower than the surrounding gas ($u_p > 0, u_p < u_g$), the drag force acts as a retarding force [4].

By substituting the Equations 3.29 to 3.32 into the force balance acting on the particle, we get the final expression for the equation of motion of the particle in the freeboard (see Eq. 3.33):

$$\frac{du_p}{dt} = -\frac{3 \cdot c_W \cdot \rho_g \cdot u_r \cdot |u_r|}{4 \cdot \rho_p \cdot d_p} - \frac{(\rho_p - \rho_g) \cdot g}{\rho_p} \tag{3.33}$$

,where

$$u_r = u_p - u_g \tag{3.34}$$

Equation 3.35 shows an expression aimed at the calculation of the drag coefficient for a particle moving in the freeboard, based on experimental findings that Haider and Levenspiel [88] derived. This expression has the potential to be applied to both spherical and non-spherical particles, by inputting the appropriate value of sphericity in each case.

$$c_w = \frac{24}{\mathrm{Re}}\left(1 + 8.1716 \cdot e^{-4.0655 \cdot \phi} \cdot \mathrm{Re}^{0.0964 + 0.5565 \cdot \phi}\right) + \frac{73.69 \cdot \mathrm{Re} \cdot e^{-5.0784 \cdot \phi}}{\mathrm{Re} + 5.378 \cdot e^{6.2122 \cdot \phi}} \tag{3.35}$$

The Re number seen in Equation 3.35 is expressed by Equation 3.36:

$$Re = \frac{u_r \cdot d_p \cdot \rho_g}{\mu_g} \tag{3.36}$$

, where d_p refers to the mean particle diameter, ρ_g represents the density of the freeboard gas, μ_g is the dynamic viscosity of the freeboard gas and u_r is given by Equation 3.34.

Gas Movement in the Freeboard

Regarding the movement of the gaseous species in the freeboard (or post-gasification zone), the Equation 3.37 is used, based on the work of Narayana and Leela [89].

$$u_g = \frac{u_0}{\epsilon_{PGZ}} \tag{3.37}$$

The ϵ_{PGZ} refers to the voidage in the freeboard or the space that the gas occupies.

$$\epsilon_{PGZ} = \frac{V_{gas}}{V_{freeboard}} \tag{3.38}$$

$$V_{gas} = V_{freeboard} - V_{particles} \tag{3.39}$$

$$V_{particles} = \frac{M_{particles}}{\rho_p} \tag{3.40}$$

After calculating the mass of solid particles in the freeboard, the computation of the gas velocity in that region can be achieved through Equation 3.37 - 3.40. Once the gas velocity in the freeboard is known, Equation 3.28 can be integrated, since there are no more unknown variables (including those in the Eq. 3.35 and 3.36).

3.3.5. Mass Balance

For the development of the 1-D Python model, the gasifier (both the fluidized bed and the freeboard) was considered to be split into ”cells” or ”control volumes”. The cells of the fluidized bed have a size of dn, while the cells of the freeboard have a size of dm. The size of each cell was calculated with Equation 3.41 and Equation 3.42 for the fluidized bed and the freeboard respectively. The mass balance equations were applied for both areas separately.

$$dn = \frac{H_{bed}}{N} \tag{3.41}$$

$$dm = \frac{H_{PGZ}}{M} \tag{3.42}$$

It should be mentioned that the number of cells in the bed (N) and the freeboard (M) are user-defined inputs to the model, chosen in such a way to reach system convergence, and balance accuracy and computational cost. The exact logic that was followed to land on the final number of cells will be further explained in Section 4.2.

3.3.5.1. Fluidized Bed

As there are two distinct phases present in the fluidized bed (the bubble and the emulsion phase), the mass balance equations were applied two times, one for each distinct phase. What is more, since both gaseous and solid species participate in the reactions in the emulsion phase, the mass balance equations also needed to be implemented separately for gaseous and solid species in the emulsion phase. In Figure 3.4, the parameters that participate in the mass balance equations in each cell for both gases and solids can be seen.

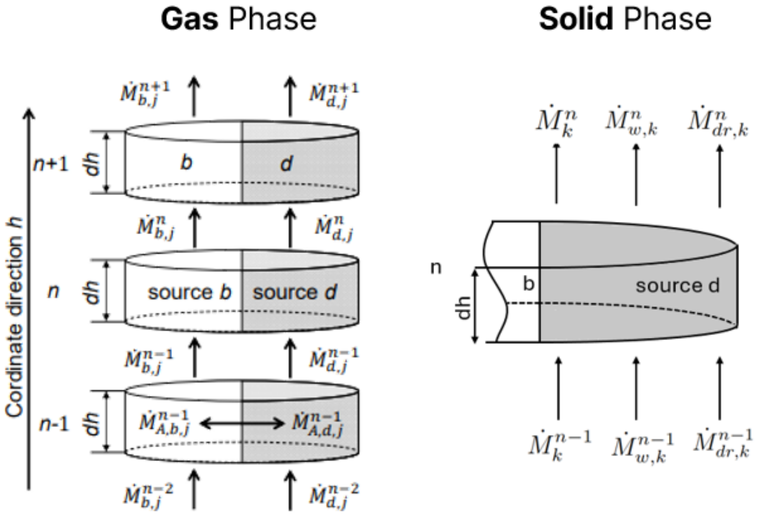

Figure 3.4: Scheme depicting: **Left**: the convective mass flows of gaseous species in the fluidized bed, where "b" refers to the bubble phase and "d" refers to the dense phase, along with interphase exchange mass flows ($\dot{M}_A$) between the two phases **Right**: the wake and drift mass flows for solids, as well as the pseudo-convective flow [6]

Gaseous Species

According to the discretization shown in Figure 3.4, the mass balance for each gaseous component in both the dense (P = d) and the bubble phase (P = b) is stated in Equation 3.43:

$$\frac{dM_{P,j}^{n}}{dt} = 0 = \dot{M}_{P,j}^{n-1} - \dot{M}_{P,j}^{n} + \dot{M}_{A,P,j}^{n} + MW_j \sum_{I_P} \nu_{i,j} R_{P,i}^{n} V_{cell}^{n} + \dot{M}_{\text{in},P,j}^{n} \tag{3.43}$$

where $\dot{M}_{P,j}$ is the convective gas mass flow (in kg/s), $\dot{M}_{A,P,j}$ is the exchange mass between bubble and dense phases of component j in phase P (in kg/s), MW_j is the molecular weight of each component j (in kg/kmol), I_P describes the maximum number of reactions taking place in the phase, $\nu_{i,j}$ is the unitless stoichiometric coefficient of component j in reaction i, R_i is the reaction rate of reaction i (in kmol/s/m^3), V_{cell}^{n} is the volume of the cell of the bed (in m^3) and finally, the term $\dot{M}_{in,P,j}$, expresses external inflows to the gasifier through the nozzles (in kg/s) [6] (which is not shown in Figure 3.4).

The convective gas mass flow $\dot{M}_{P,j}$ between adjacent cells in the dense or the bubble phase are defined by Eq. 3.44 and 3.45 respectively:

$$\dot{M}_{d,j}^{n} = \rho_d^n \cdot u_d^n \cdot Y_{d,j}^{n} \cdot (1 - \epsilon_b^n) \cdot \epsilon_d^n \cdot A_{bed}^{n} \tag{3.44}$$

$$\dot{M}_{b,j}^{n} = \rho_b^n \cdot u_b^n \cdot Y_{b,j}^{n} \cdot \epsilon_b^n \cdot A_{bed}^{n} \tag{3.45}$$

The exchange mass flow between bubble and suspension phase $\dot{M}_{A,P,j}$ inside the cell n is defined by Eq. 3.46 for the dense phase and by Eq. 3.47 for the bubble phase :

$$\dot{M}_{A,d,j}^{n} = K_{db}^{n} A_{db}^{n} \left(\rho_b^n Y_{b,j}^{n} - \rho_d^n Y_{d,j}^{n} \right) \tag{3.46}$$

$$\dot{M}_{A,b,j}^{n} = K_{db}^{n} A_{db}^{n} \left(\rho_d^n Y_{d,j}^{n} - \rho_b^n Y_{b,j}^{n} \right) \tag{3.47}$$

According to Hilligardt [6], the mass transfer coefficient between the bubble and suspension phase K_{db} is calculated by Eq. 3.48:

$$K_{db}^{n} = \frac{2.7u_d^n}{4d_b^n} \tag{3.48}$$

and the mass exchange area over all bubbles A_{db} in the cell n is calculated by Eq. 3.49:

$$A_{db}^{n} = 6\epsilon_b^n A_{bed}^n dn/d_b^n. \tag{3.49}$$

The term $\dot{M}_{in,P,j}$ which expresses the external inflows to the gasifier, in our case represents the inflows of the gasification agents through the nozzles that are located along the height of the reactor, as well as the inflows of the seal gas agent CO_2 and the inflow of H_2O as the fluidization agent at the bottom of the reactor. Regarding the entry of these gaseous compounds, it was found that these gases are primarily allocated in the bubble phase, rather than the emulsion phase. Kunii and Levenspiel [35] mention that gas entering the reactor through horizontal or downpointing pipes (which resemble the nozzles in our gasifier) produces a succession of bubbles at low gas velocities, or a gas plume at higher velocities. What is more, Prabir Basu [67] state that the bulk of the gasification gases travel up the reactor in the form of bubbles, further validating hence this assumption. The reasons behind this allocation to the bubble phase, apart from experimental observation, likely lie in the high particle concentration in the emulsion phase, which hinders the gas penetration, with the bubble phase thus providing the least resistance to the incoming gasification gases. Therefore the inflow term of the mass balance for the suspension phase can be eliminated.

The distribution of the gaseous agents along the different nozzles of the reactor was one of the parameters that sensitivity analysis was conducted on (see Chapter 4.7), in the effort to determine which allocation of the gaseous agents would lead to a syngas product closer to the experimental results.

Solid Species

For the solid species (only carbon (C) in the present model) according to the discretization shown in Figure 3.4, a different mass balance expression was used (see Eq. 3.50).

$$\frac{dM_k^n}{dt} = 0 = \dot{M}_k^{n-1} + \dot{M}_{dr,k}^{n-1} + \dot{M}_{w,k}^{n-1} - \dot{M}_k^n - \dot{M}_{dr,k}^n - \dot{M}_{w,k}^n + MW_k \sum_{I_f} \nu_{i,k} R_i^m V_{cell}^n \tag{3.50}$$

The $\dot{M}_{dr,k}$ refers to the drift term, so solids which are loosely drawn upwards because of the bubbles moving, while the $\dot{M}_{w,k}$ represents the wake term, particles that fasten to the bubbles while they are moving upwards [6].

The $\dot{M}_k$ term refers to the pseudo-convective mass flow of solid carbon moving upwards, that was included in this model and it has arisen due to the handling of solids as pseudo-gaseous in Cantera's environment.

In the literature source from which the solid mass balance model was derived [6] , the downwards motion of the solids was also considered, which was omitted in the current model. This decision was taken due to the added complexity of its incorporation, since for each cell, the velocity of the particles in the cell above would require to be known, which would add computational complexity.

The expressions for the wake and drift term are given by Eq. 3.51 and 3.52 respectively [6]:

$$\dot{M}_w = A_{bed}\rho_p(1-\epsilon_d)\epsilon_b u_{b,i}\left[0.59 - 0.046\ln(\mathrm{Ar})\right] \cdot Y_{d,C} \tag{3.51}$$

$$\dot{M}_{\mathrm{dr}} = A_{bed}\rho_p(1-\epsilon_d)\epsilon_b \cdot 0.38u_{b,i}\left[1.5 - 0.135\ln(\mathrm{Ar})\right] \cdot Y_{d,C} \tag{3.52}$$

The reason that the mass balance for the solid C was formulated as depicted in Equation 3.50, is due to our assumption and treatment of C as a pseudo-gaseous component, as has been previously mentioned. Therefore, because carbon is being considered as a gaseous component, its mass balance still has the convective flow term $\dot{M}_{\text{k}}$ in its expression, which is expressed by Eq. 3.44. The reaction term refers, as previously, to the amount of C consumed or produced from the reactions taking place in the emulsion phase, while the external inflows term $M_{\text{in,k}}$ represents carbon entering the bed, which in our case is not applicable and is therefore ignored.

3.3.5.2. Freeboard

At the end of the fluidized bed lies the freeboard or the post-gasification zone (PGZ), where the gaseous phase is prevalent with only a small amount of fine particles in it [6]. The mass balance for the gaseous species in the PGZ can be expressed through Eq. 3.53:

$$\frac{dM_j^m}{dt} = 0 = \dot{M}_j^{m-1} - \dot{M}_j^m + MW_j \sum_{I_f} \nu_{i,j} R_i^m + \dot{M}_{\text{in},j}^m \tag{3.53}$$

, where m represents the cell number in the freeboard and j the gaseous species. The $\dot{M}_{\text{j}}^{m-1}$ term represents the mass flow of the species j entering from the cell below (in kg/s), the $\dot{M}_{\text{j}}^m$ represents the mass flow of species j exiting to the cell above (in kg/s), the term $MW_j \sum_{I_f} \nu_{i,j} R_i^m$ represents the mass flow of species j that is either produced or consumed during the chemical reactions (in kg/s) and the term $\dot{M}_{\text{in,j}}^m$represents any external inflows to the freeboard through the nozzles (in kg/s).

More specifically, the convective gaseous mass flow entering from the cell below is given by Equation 3.54:

$$\dot{M}_j^{m-1} = \rho_f^{m-1} \cdot u_g^{m-1} \cdot Y_j^{m-1} \cdot \epsilon_{PGZ}^{m-1} \cdot A_{PGZ}^{m-1} \tag{3.54}$$

Similarly, the convective gaseous mass flow to the cell above is given by Equation 3.55:

$$\dot{M}_j^m = \rho_f^m \cdot u_g^m \cdot Y_j^m \cdot \epsilon_{PGZ}^m \cdot A_{PGZ}^m \tag{3.55}$$

, where ρ_f is the density of the freeboard gas (kg/m^3), u_g is the velocity of the gas in the freeboard (m/s), Y_j is the mass fraction of each species in the freeboard, ϵ_{PGZ} is the gas volume fraction in the freeboard and A_{PGZ} is the area of one cell in the freeboard (m^2).

The link between the fluidized bed and the freeboard is shown in Eq. 3.56 and 3.57:

$$\dot{M}_{f,j}^{m=0} = \dot{M}_{d,j}^{n=N} + \dot{M}_{b.j}^{n=N} \tag{3.56}$$

$$M_{f,k}^{m=0} = M_{d,C}^{n=N} + M_{ash,feed} \tag{3.57}$$

, where it is expressed that the mass flow of gaseous species j in the first cell of the freeboard is equal to the mass flow of the same species on the last cell of the emulsion phase in the fluidized bed plus the mass flow of that species on the last cell of the bubble phase in the bed. In addition, the solid particles that enter the freeboard consist of the solid carbon (C) that is present in the last cell of the bed and the ash content of the feedstock.

Regarding the mass balance of the solids in the freeboard, it is expressed by Equation 3.58, which is a modification of the Equation 3.53.

$$\frac{dM_k^m}{dt} = 0 = \dot{M}_k^{m-1} - \dot{M}_k^m + MW_k \sum_{I_f} \nu_{i,k} R_i^m \tag{3.58}$$

, where m represents the cell number in the freeboard and k the solid species (which is C in the present case). The $\dot{M}_k^{m-1}$ term represents the mass flow of the species k entering from the cell below (in kg/s), the $\dot{M}_k^m$ represents the mass flow of species k exiting to the cell above (in kg/s) and the term $MW_k \sum_{I_f} \nu_{i,k} R_i^m$ represents the mass flow of species k that is either produced or consumed during the chemical reactions (in kg/s). The external inflow term is removed, since there are no solids entering through the nozzles of the gasifier.

Similarly to the convective gaseous flow in the freeboard, the convective solid flow from the cell below is expressed by Equation 3.59:

$$\dot{M}_k^{m-1} = \rho_f^{m-1} \cdot u_p^{m-1} \cdot Y_k^{m-1} \cdot (1 - \epsilon_{PGZ}^{m-1}) \cdot A_{PGZ}^{m-1} \tag{3.59}$$

The convective solid mass flow to the cell above is given by Equation 3.60:

$$\dot{M}_k^{m} = \rho_f^{m} \cdot u_p^{m} \cdot Y_k^{m} \cdot (1 - \epsilon_{PGZ}^{m}) \cdot A_{PGZ}^{m} \tag{3.60}$$

Since C is treated as a pseudo-gas species in this model, the density used in the convective mass flow is the freeboard gas density, because Cantera provides the species mass fractions relative to the freeboard gas mixture that it's receiving as input. However, C represents solid char and the solid particles in the freeboard move with a velocity u_p, and therefore this velocity will be used for the calculation of the convective mass flow.

In addition, since char is solid, it occupies the particle-laden part of the freeboard, described by the term (1-ϵ_{PGZ}), which is multiplied with the area of a cell (A_{PGZ}), in order to account for this situation.

3.4. Model Algorithm

The developed 1-D model simulates a bubbling fluidized bed gasifier by dividing the bed and the freeboard into a series of discrete cells along its height. Each cell of the bed represents a control volume containing two distinct gas phases: the bubble and the emulsion, while each cell of the freeboard zone represents the gases and particles that are present there. The algorithm iteratively solves mass balances in each cell while accounting for interphase mass exchange (for the bed cells only), chemical reactions and convective transport, until reaching convergence.

A schematic overview of the model algorithm is shown in Figure 3.5. The algorithm begins with the initialization of the operating conditions and other relevant parameters. This is followed by the modeling of the pyrolysis process and the definition of the external mass inflows through the nozzles. The fluidized bed mass balance is then being implemented, followed by the mass balance for the freeboard. Lastly, the final syngas composition is processed and compared with the experimental set of data.

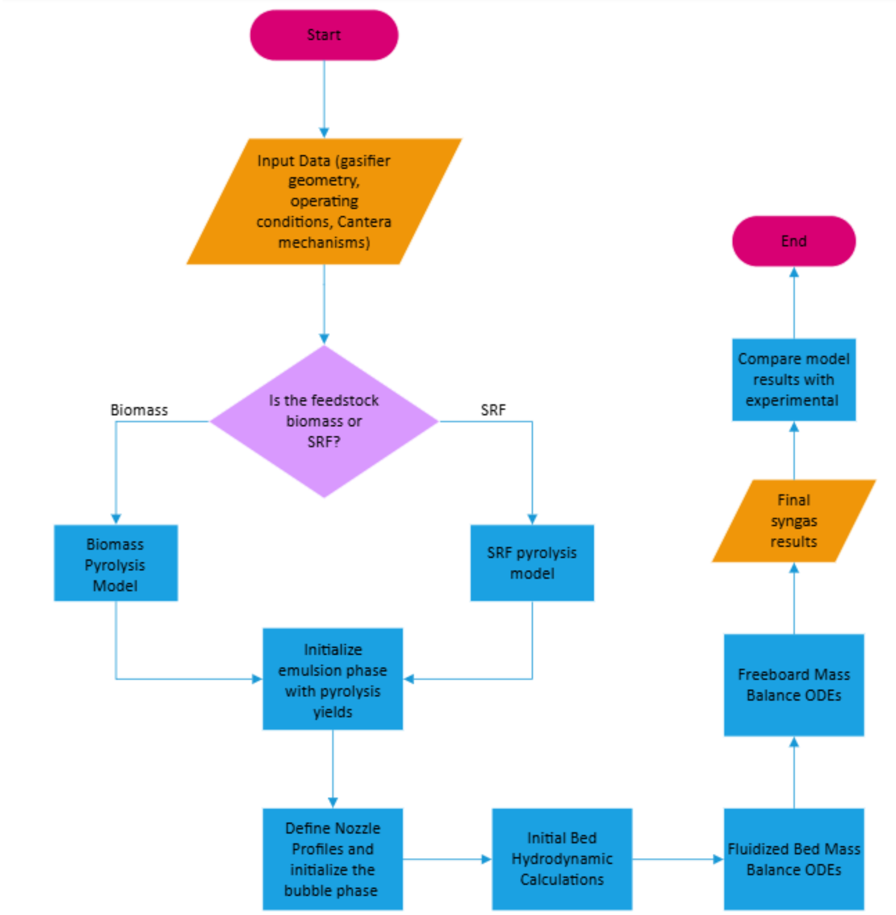

Figure 3.5: Model Algorithm Scheme.

A detailed step-by-step description of the complete model algorithm is given in Appendix B.

3.5. Case Definition

The gasifier that was considered for the validation of this model was the pilot-scale fluidized bed gasifier at the Institute of Energy Systems and Technology at the Technical University of Darmstadt in Germany [90].

A schematic diagram of the experimental setup can be observed in Figure 3.6.

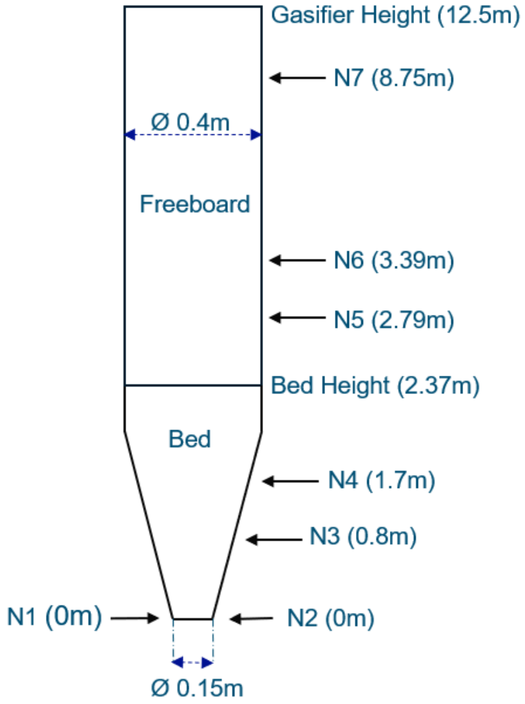

Figure 3.6: Schematic diagram of the considered fluidized bed gasifier reactor at TU Darmstadt.

For a detailed depiction of the gasifier, refer to the work of Heinze et al. (2023) [91].

3.5.1. Gasifier Dimensions

The gasifier of Figure 3.6 has the following technical characteristics and dimensions:

1. The reactor has a conical part at its bottom, with a bottom diameter of 0.15 m ($\varnothing 0.15$) and a top diameter of 0.4 m ($\varnothing 0.4$) [91].
2. The end of the conical area of the gasifier ends at a height of approximately 2m [91].
3. The area of the fluidized bed ends slightly higher than the end of the conical part of the gasifier, at a height of $H_{bed} = 2.37$m [91].
4. The diameter of the freeboard is 0.4 m ($\varnothing 0.4$) [91].
5. The height of the total gasifier is approximately 12.5 m [91].
6. The height of the freeboard is $H_{PGZ} = 10.13$m (12.5 m - 2.37 m) [91].
7. There are nozzles placed along the height of the gasifier with the following characteristics:
    (a) The N1 nozzle supplies CO_2 as seal gas for the bottom extraction process (considered at h=0 m), in order to prevent syngas from exiting the gasifier through the bottom product removal system [91].
    (b) The N2 nozzle supplies superheated steam for fluidization (considered also at h=0 m) [91].
    (c) The nozzles N3 and N4 supply steam and oxygen into the bed zone, considered at 0.8 m and 1.7 m respectively [91].
    (d) The nozzles N5 and N6 supply steam and oxygen in the freeboard, considered at 2.79 m and 3.39 m respectively [91].
    (e) The nozzle N7 ejects water in the freeboard if the temperatures at the reactor outlet exceeds the acceptable limit or if the raw gas cooler, situated at the exit of the cyclone, exceeds its designated power. The nozzle N7 is situated at a height of 8.75 m [91].

Since, as it was previously mentioned, part of the bed area of the gasifier has a conical shape, it was important to accurately define the reactor bed geometry, and more specifically how the bed diameter and corresponding cross-sectional area vary with the height of the reactor. The diameter changes linearly from the bottom diameter (0.15 m) to the top diameter (0.4 m), and then continues at a constant diameter of 0.4 m until the end of the height of the bed (H_{bed}). In order to capture this variation in the bed diameter at any height (y), Equation 3.61 was applied, based on a linear interpolation:

$$d_{\text{bed}}(y) = \begin{cases} d_{\text{bottom}} + \left(\frac{d_{\text{top}} - d_{\text{bottom}}}{z_{\text{cone\_end}}}\right) y, & \text{for } y \leq z_{\text{cone\_end}} \\ d_{\text{top}}, & \text{for } y > z_{\text{cone\_end}} \end{cases} \tag{3.61}$$

, where y refers to the midpoint of each cell of the fluidized bed, leading essentially to the calculation of the bed diameter at the center of the control volume.

Once the bed diameter at a given height is known $d_{bed}(y)$, the corresponding cross-sectional area $A_{bed}(y)$ can be determined through Equation 3.62 using the formula for the area of a circle.

$$A_{bed}(y) = \pi \left(\frac{d_{\text{bed}}(y)}{2}\right)^2 \tag{3.62}$$

In addition, the volume of each cell can be calculated through Equation 3.63:

$$V_{cell}(y) = A_{bed}(y) \cdot dn \tag{3.63}$$

The cross-sectional area $A_{bed}(y)$ and the volume of each cell $V_{cell}(y)$ are used for the calculation of various mass balance terms, as can be seen in Section 3.3.5.

3.5.2. Operating Conditions

The operating conditions that were implemented in the present model were:

1. The pyrolysis temperature was assumed to be 650° C [3, 60].
2. The gasification temperature in the bed was 713° C and 751 ° C in the freeboard [3].
3. The pressure P at the fluidized bed reactor was considered to be atmospheric, in order to be in line with the experimental conditions, and uniform across the reactor [47].
4. The average particle size of the bed material (d_p) was considered to be 500 μm, and was considered to remain constant during the operation [92].
5. The particle density of the bed material (ρ_p) was considered to be around 2500 kg/ m^3, based on literature sources [67, 92].
6. The bed material belongs in Geldart's Group B category, based on its particle size (d_p = 500 μm) and density (ρ_p = 2500 kg/m^3) and the Figure 2.1. The value of ρ_f corresponds to the density of air, which with a molar mass of 0.029 kg/mol and at atmospheric conditions and a temperature of 713° C is 0.36 kg/ m^3 through the assumption of air as ideal gas (ρ_f = P · MW / (R · T)).
7. Superficial gas velocity at an empty-pipe reactor u_0 was considered as equal to 0.30 m/s, based on literature sources and the mass flow rate of fluidization agents. This assumption is in line with literature sources for bubbling fluidized beds with Geldart B particles, as it is stated that bubbling fluidization can even occur at gas velocities ranging from 2 to 20 times the minimum fluidization velocity [35]. In the Results Section 4.3, it can be seen that this u_0 value aligns with the u_{mf} value.
8. The feedstock flow entering the gasifier is 80.1 kg/hr, based on the data from the experimental test conducted at the TU Darmstadt gasification facility.
9. The total amount of CO_2 entering the reactor through nozzle N1 is 38.6 kg/hr.
10. The total amount of O_2 entering the reactor through the different nozzles is 43.2 kg/hr.
11. The total amount of H_2O entering the reactor through the different nozzles is 52.1 kg/hr.

3.5.3. Feedstock Composition

The composition of the feedstock that was used for the validation of the 1-D computational model is displayed in Table 3.2. The feedstock is a pelletized Solid Recovered Fuel, which was provided by the company N+P under the brand name ”Subcoal” [3]. The exact values for the composition of the feedstock were not given, but rather a bar chart depicting the fuel analysis was provided, hence the rounding of all the numbers in Table 3.2.

Table 3.2: Feedstock Proximate and Ultimate Analyses

Proximate Analysis (a.r.)	**Content (%)**	**Ultimate Analysis (waf)**	**Content (%)**
Moisture	5	Carbon	68
Ash	15	Hydrogen	9
Volatile Matter	75	Nitrogen	1
Fixed Carbon	5	Oxygen	22

4

Results

In the following sections, the results from different parts of the model are presented. More specifically, in Section 4.1 the results of the pyrolysis model are presented, followed by Section 4.2, where the logic behind the grid discretization and the mass balance integration is discussed in detail. In Section 4.3, the results of the bed hydrodynamic model are shown, while in Section 4.4, the freeboard hydrodynamics are presented. In Section 4.5, the numerical solution acquired from the current model is compared with the experimental set of data from the TU Darmstadt campaign, and the evolution of species' quantities along the reactor is depicted. In Section 4.6, the mass balance validation of the model is discussed, while in Section 4.7, four different tests of sensitivity analysis are conducted, testing the effect of the freeboard temperature, the nozzle gas distributions, the kinetic parameters and the initial gasification conditions on the final syngas product result.

4.1. Pyrolysis Results

In Table 4.1, the results of the pyrolysis model under a temperature of 650 ° C are shown, presenting the percentage of the mass yield for each species released during devolatilization. Although there is no O_2, C_2H_4 or N_2 released, the species are still listed in the Table for matters of clarity, since this is the full list of species considered in the current model.

Table 4.1: Pyrolysis product yields for each species (kg/kg waf fuel) of feedstock "Subcoal" at a temperature of 650 ° C

Species	**Mass Yield (%)**
H_2	0.121
CO	1.944
CO_2	3.305
$C_{10}H_8$	15.98
H_2O	5.904
C_6H_6	15.98
C_6H_6O	15.98
O_2	0.000
CH_4	3.421
C_2H_4	0.000
C	37.365
N_2	0.000

From Table 4.1, it is obvious that the species that dominate are the tar compounds ($C_{10}H_8$, C_6H_6 and C_6H_6O) and the char. The mass fraction of the gaseous pyrolysis products (CO, H_2, CO_2, H_2O and CH_4) is approximately 14.7%.

The results are generally consistent with findings in literature regarding the pyrolysis of SRF in bubbling fluidized beds. For example, in the work of Tokmurzin et al. [66], it is stated that at pyrolysis temperatures of around 600 ° C (similar to the 650 ° C that is considered in this model), tar is typically the major product.

When the pyrolysis temperature increases (i.e. from 600 ° C to 900 ° C), the gas yield of the products is expected to rise, due to a augmented thermal scission and decomposition taking place [66].

The char yield predicted by the current model falls within a reasonable range for pyrolysis of SRF at 650 ° C, albeit slightly on the higher side. The yield of 37% is consistent with findings from the study of Tokmurzin et al. [66], who report a range of values between 18 - 40 % for char yield. Regarding the tars, the pyrolysis model's result for C_6H_6, C_6H_6O and $C_{10}H_8$ falls within the values suggested by [66] of 30-60%, again on the higher side. In order for the tar compounds to be decreased or the gaseous products to increase, a higher pyrolysis temperature would need to be applied.

In order to check the consistency of the empirical pyrolysis model for SRF, elemental mass balances for C, H and O were computed using the mass yields of species CO, H_2, CO_2, CH_4, H_2O, tar and char. Since the pyrolysis model provides only temperature-dependent expressions for the pyrolysis mass yields, and the elemental feedstock's composition was taken from a literature source, the expressions of the elemental mass balances don't represent an actual conservation or loss of mass, but can rather be perceived as an error or deviation estimate between the known elemental composition of the fuel used and the implied elemental composition of the fuel that undergoes pyrolysis.

$$\begin{aligned} Y_{\text{C},F} = Y_{\text{char}} + Y_{\text{C,tar}} \cdot Y_{\text{tar},F} + Y_{\text{C},CH_4} \cdot Y_{\text{CH}_4,F} \\ + Y_{\text{C},CO} \cdot Y_{\text{CO},F} + Y_{\text{C},CO_2} \cdot Y_{\text{CO}_2,F} \end{aligned} \tag{4.1}$$

$$\begin{aligned} Y_{\text{O},F} = Y_{\text{O,tar}} \cdot Y_{\text{tar},F} + Y_{\text{O},CO} \cdot Y_{\text{CO},F} \\ + Y_{\text{O},CO_2} \cdot Y_{\text{CO}_2,F} + Y_{\text{O},H_2O} \cdot Y_{\text{H}_2O,F} \end{aligned} \tag{4.2}$$

$$\begin{aligned} Y_{\text{H},F} = Y_{\text{H,tar}} \cdot Y_{\text{tar},F} + Y_{\text{H},CH_4} \cdot Y_{\text{CH}_4,F} \\ + Y_{\text{H},H_2O} \cdot Y_{\text{H}_2O,F} + Y_{\text{H},H_2} \cdot Y_{\text{H}_2,F} \end{aligned} \tag{4.3}$$

Based on the values of the pyrolysis mass yields displayed in Table 4.1, a pyrolysis temperature of 650 ° C and the SRF's elemental composition (see Table 3.2), the discrepancies that were observed between the left-hand side and the right-hand side of the elemental mass balances for C, H and O were very small in scale, around ±3% for carbon and hydrogen (see Equation 4.1 - Equation 4.3), which implies that the actual feedstock composition is very close to the one considered by the pyrolysis model.

4.2. Grid Size and Mass Balance Integration for Fluidized Bed and Freeboard

Grid Size

The size of the grid (i.e. the number of the control volumes, "N" and "M") significantly affects the accuracy of the model, as well as its numerical stability. A finer grid (higher N or M value) will lead to a better, more accurate solution, but also to a higher computational time [32]. On the other hand, a coarser grid (lower N or M value), will lead to numerical oscillations and divergence. Therefore, the amount of cells for both the bed and the freeboard was inferred through iterative trial and error for both cases. To be more specific, when the number of cells was small, and therefore the cells were larger in size, the system had difficulty in reaching convergence, due to disproportionately large reaction terms in the mass balance, compared to the other terms present (see Section 3.3.5), since the reaction term is directly affected by the volume of each cell. On a stiff system (due to nonlinear, fast reaction kinetics and tightly coupled convection–reaction terms) like the current one, big step sizes can lead to oscillations in the results, and therefore the step size needed to be reduced and the number of cells to increase until reaching convergence. In addition, since the number of cells affects also the time span that the mass balance ODEs were integrated for, a longer time span can accumulate integration errors and also lead to oscillations in the system.

Based on all the aforementioned considerations, for the present study the gasifier was discretized with 5000 computational cells along the reactor's vertical axis, comprised of N = 1000 cells in the fluidized bed and M = 4000 cells in the freeboard. This specific ratio of discretization was chosen based on the relative heights of the two regions. More specifically, the fluidized bed region has a height of 2.37 m, while the freeboard was a height of 10.13 m (see Section 3.5.1). In this way, a consistent spatial resolution was ensured across the entire reactor.

The ratio of the freeboard height to the fluidized bed height can be calculated as:

$$\frac{H_{PGZ}}{H_{bed}} = 4.27 \tag{4.4}$$

Hence, the amount of cells in the freeboard was selected to be approximately 4 times higher than the amount of cells inside the bed (4000 vs 1000), ensuring similar cell sizes in both regions.

Therefore, the resulting cell size for the fluidized bed, based on Equation 3.41 was calculated as $dn = \frac{H_{bed}}{N} = 0.0024$m, while the cell size for the freeboard (see Equation 3.42) was $dm = \frac{H_{PGZ}}{M} = 0.0025$m. The fact that both cell sizes are of the same order makes physical sense, as in both the freeboard and the bed a similar set of ODEs is being integrated, with comparable numerical stiffness.

Mass Balance Integration and Convergence

The mass balance ODEs presented in Section 3.3.5 were integrated for the duration of the residence time of gases in the bed and in the freeboard respectively. The values for the residence time of the gases in the bed was derived from Kunii and Levenspiel's expression in [35] (see Equation 4.5), while the residence time of the gases in the freeboard was calculated based on Equation 4.6.

The terms u_0, H_{bed} and H_{PGZ} have been defined in Section 3.5. The term u_g in Equation 4.6 refers to the gas velocity in the freeboard, which is discussed in Section 4.4.

$$\tau_{tot,bed} = \frac{\epsilon_f \cdot H_{bed}}{u_0} \tag{4.5}$$

$$\tau_{tot,freeboard} = \frac{H_{PGZ}}{u_g} \tag{4.6}$$

In Equation 4.5, the term ϵ_f refers to the overall void fraction in the entire fluidized bed, according to [35]. It therefore represents the average gaseous volume fraction throughout the bed, taking into account both the gas in the emulsion phase and the gas in the bubble phase. The expression from Kunii and Levenspiel regarding the bed residence time provides a global average residence time for the gaseous species, and it is not phase-specific (same value for the emulsion or the bubble phase).

The expression for the ϵ_f is shown in Equation 4.7:

$$\epsilon_f = \epsilon_b + (1 - \epsilon_b) \cdot \epsilon_d \tag{4.7}$$

, where ϵ_b refers to the bubble volume fraction of the bed and ϵ_d represents the void fraction of the emulsion phase, as they have been defined in Section 3.3.4.1.

Since the hydrodynamic properties of the bed are solved for as the mass balance ODEs are also integrated, an average value of 0.62 for ϵ_f was used for the solution of the ODEs, which can also be validated by the results of ϵ_d and ϵ_b, shown in Section 4.3.

Using this derived value of ϵ_f, the bed residence time was found to be 4.88 s, while the freeboard residence time was calculated as 33 s. Both the bed and the freeboard residence time can be validated from literature sources, since in the study of Ghaly et al. [93] a bed residence time of 4 s is listed , while in the work of Bates et al. [94], it is stated that a freeboard residence time can vary between 4-30 s, therefore validating the current value.

The expression for the calculation of the residence time in the freeboard is based on the assumption of plug-flow in this region. In order to validate this assumption, the Peclet number was calculated for the freeboard region. The Peclet number is a dimensionless quantity that expresses the ratio of convective to diffusive transport [95] and is given by Equation 4.8.

$$Pe = \frac{u \cdot L}{D_{eff}} \tag{4.8}$$

, where u refers to a characteristic velocity (in m/s), L a characteristic length (in m) and D_{eff} is the mass diffusion coefficient.

When the Peclet number is very large (approaching infinity), diffusion is negligible and convection dominates the mass transport [95], basically representing ideal plug-flow. A lower Peclet number, around 1, indicates that both convection and diffusion have an influence on the mass transport, while a lower Peclet number, which approaches 0, shows that diffusion dominates the mass transport.

Regarding the calculation of the Peclet number in the freeboard, the gas velocity in that region u_g was used, as well as the length of the post-gasification zone H_{PGZ}. As for the diffusion coefficient, this was calculated through the internal commands of Cantera, which basically uses the hypothesis of ”mixture-averaged”.

Cantera features the command ”mix diff coeffs” which calculates the diffusion coefficient for each species present in the mixture considered each time, with the hypothesis of a mixture-averaged transport model. Hence, based on these values and on the mass fraction of each species, a weighted average diffusion coefficient can be calculated. By using a representative set of values for the mass fractions of the freeboard gas (since these change along its height) from both the beginning and the end of the freeboard, some satisfying values can be derived for the diffusion coefficient, and therefore for the Peclet number. Two measurements of the Peclet number were hence used, one for the beginning of the freeboard (end of fluidized bed) where $Pe = 17,144.4$, and one for the end of the freeboard, where $Pe = 14,793.51$. Both of these values validate the assumption of plug-flow in the freeboard.

Given the values for the total residence time of gases in the bed and in the freeboard, the ”cell residence time” was calculated, by dividing the total residence time over the amount of cells for each case (see Equation 4.9 and Equation 4.10).

$$\tau_{cell,bed} = \frac{\tau_{tot,bed}}{N} = \frac{4.8}{1000} = 0.0048\text{s} \tag{4.9}$$

$$\tau_{cell,freeboard} = \frac{\tau_{tot,freeboard}}{M} = \frac{33}{4000} = 0.0083\text{s} \tag{4.10}$$

The mass balance ODEs were integrated in each cell for a time span of the equivalent of the cell residence time. Therefore, the discretization of the grid, once again had a big influence on the integration of the ODEs.

In order to reach numerical convergence, an under-relaxation factor was introduced in the model, as previously described in Section 3.4. The appropriate values for the under-relaxation factor were determined through iterative trial and error. Before introducing under-relaxation, the model's results often showed oscillatory behavior and failed to reach a stable value and converge. Hence, in order for the model to procure a stable outcome, a relaxation factor needed to be implemented in both the loop for the fluidized bed and the freeboard. For the fluidized bed, a different value of under-relaxation was implemented for the emulsion and the bubble phase - 0.0024 and 0.01, respectively- while for the freeboard a factor of 0.0032 was applied.

Iterations for Convergence

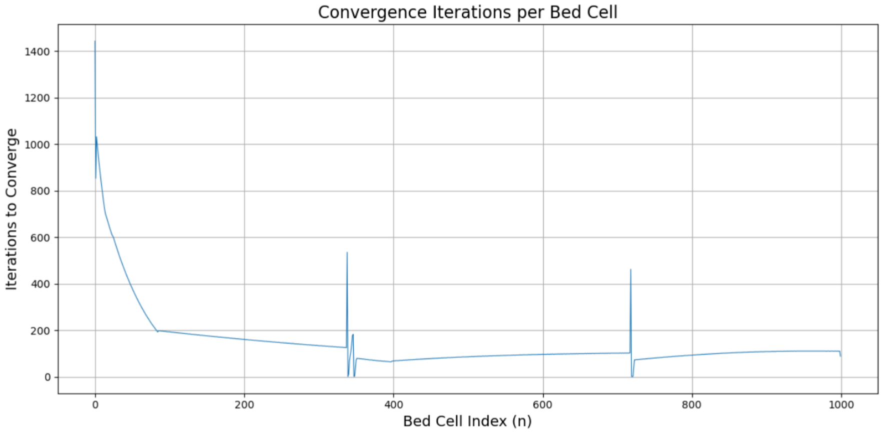

Figure 4.1: Iterations needed for convergence for each computational cell in the bed.

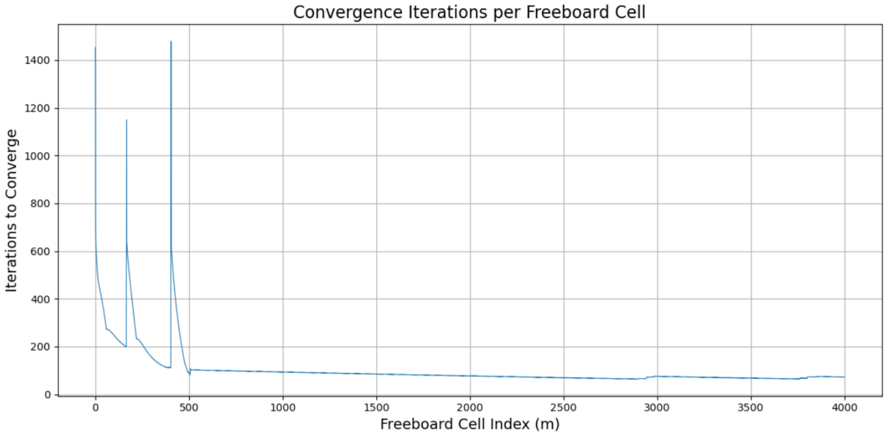

Figure 4.2: Iterations needed for convergence for each computational cell in the freeboard.

Both Figures 4.1 and 4.2 show that most computational cells in both domains generally need few iterations in order to reach convergence. However some spikes are witnessed, showing that some cells need significantly more iterations than the rest. The cells that seem to be struggling the most with convergence are the cells where the nozzles are positioned (cells [0, 338, 718] for the bed and [167, 404] for the freeboard), and therefore an extra term is introduced in the mass balance ODEs (the incoming mass flow term, M_{in}, see Equations 3.43 and 3.53). In addition, it is evident that the first cells of the freeboard are also struggling with convergence, even though there are no nozzles present there, which can probably be attributed to the inlet conditions (mass entering the freeboard from the top of the bed).

Indeed, by comparing the value for the mass inflow term with the other terms of the mass balance ODEs (convective flow, interphase gas exchange and reaction term), it is obvious that the external mass inflow term is of a similar order of magnitude with the other mass balance terms, if not larger. This justifies the fact that the cells where nozzles are located need significantly more iterations than the rest, while also highlighting the need for improved model efficiency, so that the computational time gets reduced.

The most dominant contributor is usually the incoming mass flow term, followed closely by the reaction rate term. In the bed, where there is also the mass exchange term, the incoming flow term tends to dominate, while the reaction term, the convective flow term and the mass exchange term follow in importance. In the freeboard, a similar trend is also observed. Naturally, depending on the distribution of gases among the injection nozzles, the relative importance between the incoming flow term and the reaction rate term may switch. Regarding the solid species present in the fluidized bed, the most dominant contributor to the mass balance ODE tends to be the drift and wake term, followed by the convective flow term and the reaction rate term.

4.3. Bed Hydrodynamics

Bubble Growth

The vertical profile of the bubble diameter along the fluidized bed height can be seen in Figure 4.3. From the graph, it can be observed that the bubble diameter grows as the bubbles move along the bed, but not significantly. The diameter remains around the value of 11 cm, which is smaller than the diameter of the bed itself, which varies between 15 - 40 cm.

This bubble behavior is consistent with the expected fluidization characteristics for Geldart B particles, since they are known to form larger bubbles than Geldart A particles (see Section 2.2). In addition, from the graph, it can be observed that the bubbles continue to grow, with no equilibrium bubble size being reached.

This model was preferred to be implemented over the one from Hamel's model, as it accounts for the gasifier dimensions to ensure physical realism. In addition, the current bubble growth model is also applicable to the slugging regime, when higher superficial gas velocities are applied. The current model is an improvement to Hamel's model, which tended to overestimate the bubble size at high gas velocities, sometimes providing bubble diameter results which even surpassed the gasifier's dimensions, leading to non-physical results.

The size of the bubbles can also be validated by literature sources, showing that the diameter of a bubble ranges between values of 1 - 10 cm [96, 97, 98].

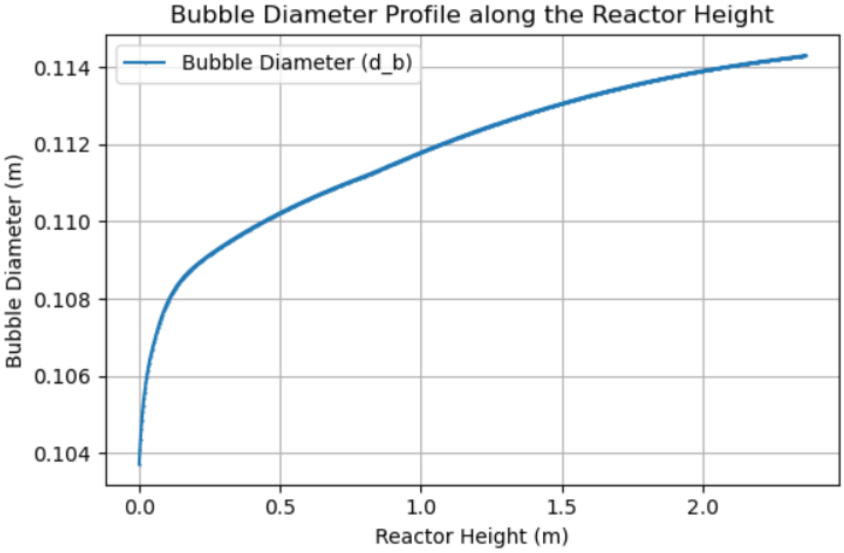

Figure 4.3: Vertical profile of bubble diameter growth in the fluidized bed.

Bubble Velocity

In Figure 4.4, the change in the bubble rise velocity u_b and the isolated bubble rise velocity $u_{b,i}$ are depicted along the height of the fluidized bed.

From Figure 4.4, it can be observed that both velocities increase gradually along the height of the bed. This is a reasonable outcome, since larger bubbles (given that the bubble diameter increases along the height of the bed, as seen previously in Figure 4.3) rise faster to the bed surface (higher velocity), due to physical effects such as a lower drag-to-buoyancy ratio, which is reflected by the $(g \cdot d_b)^{1/2}$ term in the $u_{b,i}$ Equation (see Equation 3.24).

The bubble rise velocity values predicted by the model (at approximately 0.80 - 0.83 m/s) align well with typical findings in literature for Geldart B particles in bubbling fluidized beds. In the study of Kunii and Levenspiel [35], it is reported that for Geldart B particles and with superficial gas velocities of around 0.1 - 0.3 m/s, a bubble rise velocity of around 0.9 - 1 m/s can be expected. Similarly, for the isolated bubble rise velocity, which only depends on the bubble diameter, values of around 0.4 - 0.9 m/s are reported. Similarly, in the work of Agu et al. [99], a bubble rise velocity was calculated to vary between 0.2 - 0.6 m/s for glass and limestone particles as bed materials. Although both of these materials have particle diameters smaller and larger, respectively, than the particle diameter considered in the current model, the similar trend of the bubble velocity is still visible. Therefore it is safe to say that both our results are within a physically realistic range.

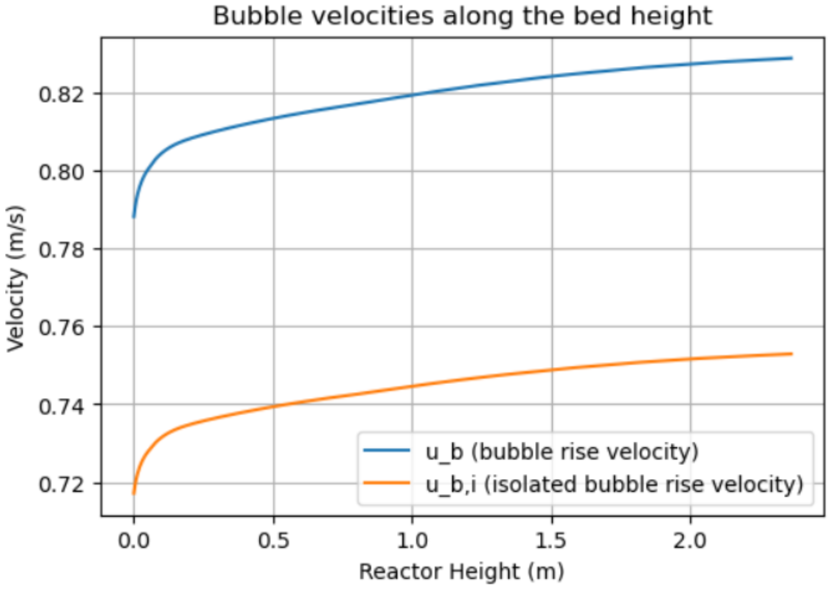

Figure 4.4: Vertical profile of bubble velocities in the fluidized bed.

Bubble volume fraction

In Figure 4.5, the change in bubble volume fraction ϵ_b is depicted along the height of the fluidized bed.

From Figure 4.5, it can be observed that the bubble volume fraction ϵ_b increases slightly along the height of the reactor, with changes only occurring in the second decimal place. The value of the bubble volume fraction fall reasonably with ranges seen in literature sources, such as values between 0.1 - 0.24 stated in the work of Van et al. [96], or 0.18 - 0.27 for a commercial and bench unit respectively in the study of Kunii and Levenspiel [35]. The slightly increasing trend of the bubble volume fraction is consistent with literature sources, where it is stated that the solid volume fraction decreases along the height of the reactor, and therefore the bubble volume fraction increases, as bubbles coalesce and form bigger entities [76].

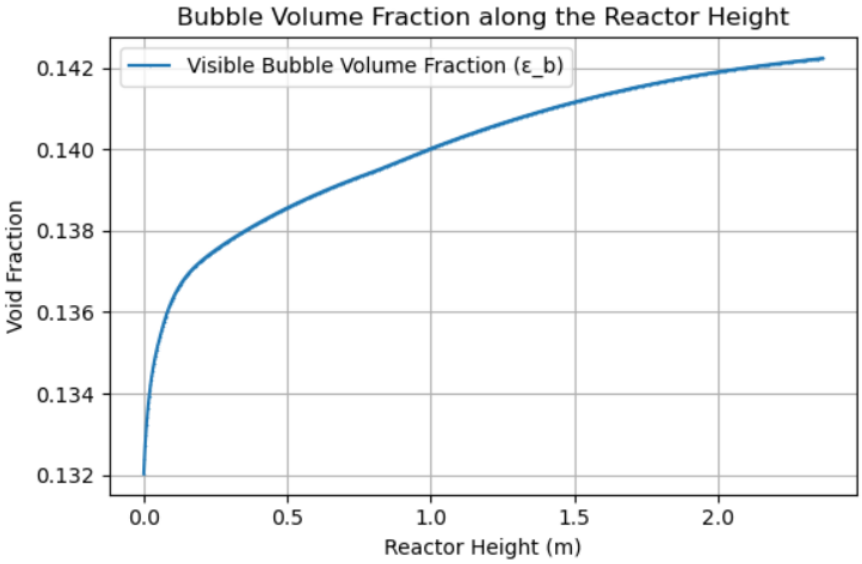

Figure 4.5: Vertical profile of bubble volume fraction in the fluidized bed.

Emulsion Gas Velocity

In Figure 4.6, the change in the velocity of the emulsion gas is depicted along the height of the fluidized bed. In the Figure it can be observed that the emulsion gas velocity gradually decreases along the height of the bed, but not substantially.

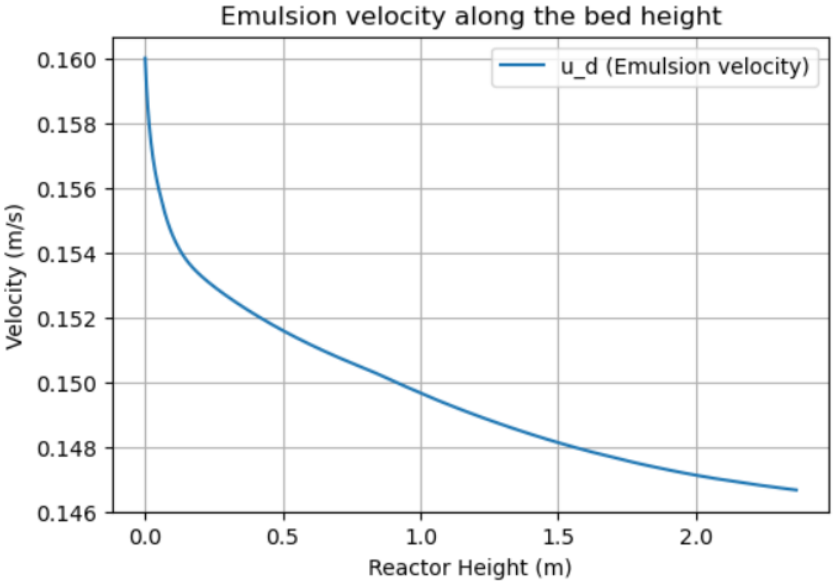

Figure 4.6: Vertical profile of emulsion velocity in the fluidized bed.

The reason behind this declining trend of the emulsion gas velocity is the gradual decrease in the minimum fluidization velocity, which can be seen in Figure 4.7, and it is also consistent with literature findings [100].

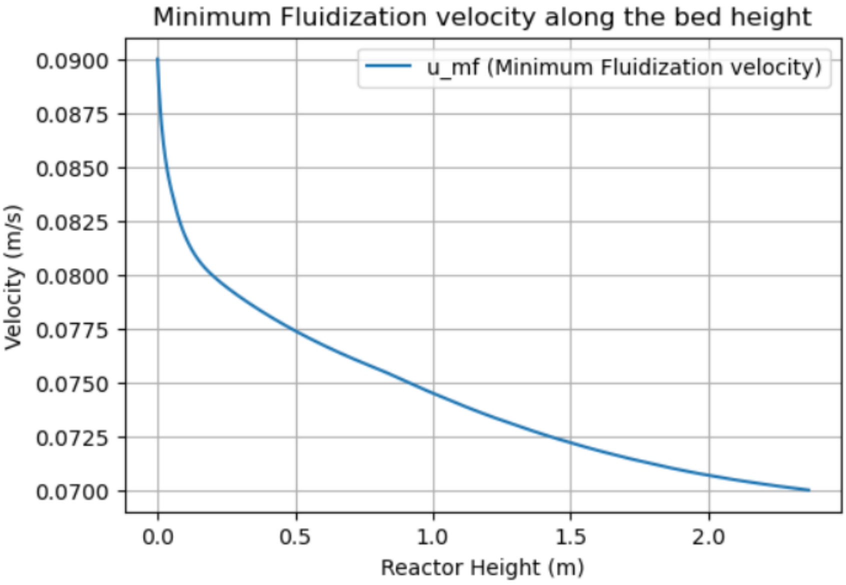

Figure 4.7: Vertical profile of minimum fluidization velocity in the fluidized bed.

Based on Equation 3.16, it is obvious that the emulsion gas velocity u_d depends greatly on the minimum fluidization velocity u_{mf}, which decreases as the gasification reactions proceed, producing more light gases (such as CO, H_2 and CO_2) and hence becoming less dense and less viscous. Less viscous gases exert less drag force on the suspended particles, which subsequently signifies that lower velocities are needed to reach minimum fluidization, so u_{mf} drops. Therefore, a lower minimum fluidization velocity will also lead to a lower emulsion gas velocity, since less gas is needed to fluidize the bed, while also more gas moves the bed as bubbles.

Emulsion void fraction

In Figure 4.8, the change in the emulsion void fraction is depicted along the height of the fluidized bed.

From Figure 4.8, it can be observed that the gaseous void fraction in the emulsion phase increases slightly as we move towards the surface of the fluidized bed, but remains relatively stable overall, around the value of 0.53. These values for the emulsion void fraction are consistent with literature findings, as measurements in the range of 0.4 - 0.7 are recorded for Geldart B particles in bubbling fluidized beds [35]. What is more, for Geldart B and D particles, it is often assumed that the emulsion void fraction ϵ_d is approximately equal to the void fraction during minimum fluidization conditions ϵ_{mf}, which was calculated to be 0.43, hence proving the validity of the model's results.

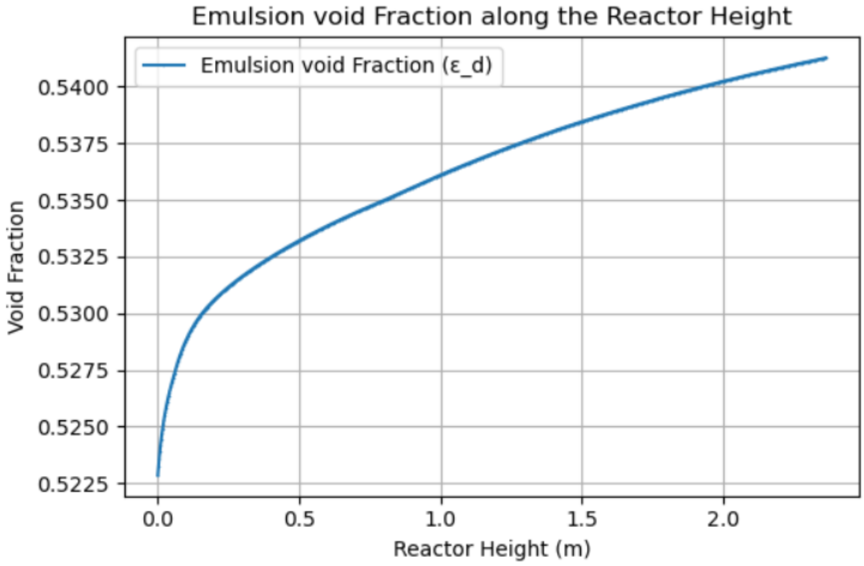

Figure 4.8: Vertical profile of emulsion void fraction in the fluidized bed.

4.4. Freeboard Hydrodynamics

In Figure 4.9, the change in the particle velocity in the freeboard is shown, which was derived from the particle motion equation (see Equation 3.28).

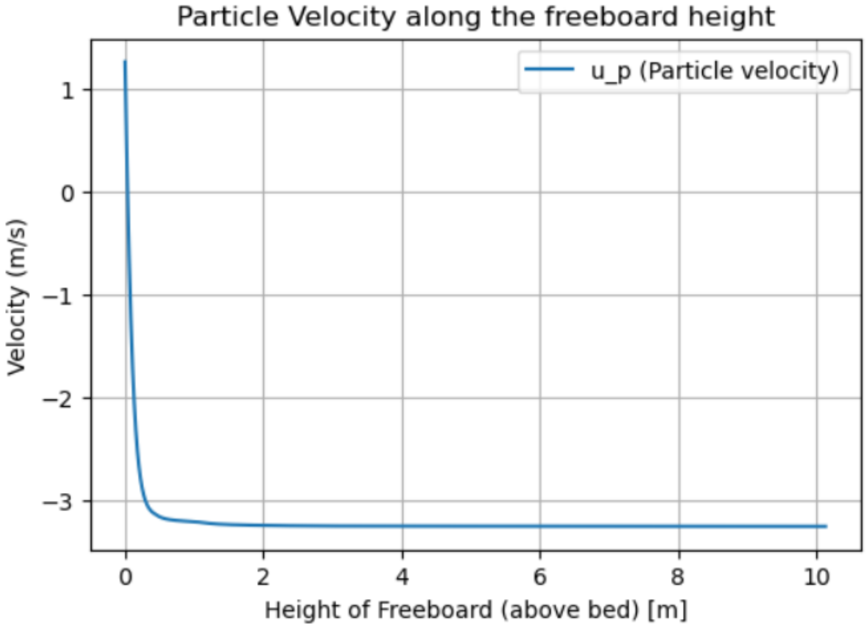

Figure 4.9: Vertical profile of particle velocity in the freeboard.

As can be noticed from the graph, at the bottom of the freeboard -close to the bed surface -, the particles are entrained upwards by the gas flow. The particles reach a maximum upwards velocity of around 1.2 m/s, and keep on moving upwards, but with a decreasing velocity value, due to gravity and drag force acting on the particles. When the particles reach the highest point in the freeboard, their velocity becomes zero, and then goes negative, indicating the particles' descent towards the bed surface. This evolution of the particles' velocity describes the typical behavior of particles in the freeboard area [35], where only the finest and smallest particles manage to escape the freeboard region and enter the cyclone, located downstream.

The mass of particles that was entrained in the freeboard was calculated using Equation 3.57, and was found to be 0.11 kg. This mass of solids corresponds to a particle volume of just $4.5 \cdot 10^{-5}$ m^3, which is negligible compared to the total freeboard volume - equal to 1.27 m^3. Therefore, based on this mass of entrained particles, the gas volume fraction in the freeboard, was calculated to be nearly unity, through Equation 3.38, which led to a velocity in the freeboard u_g of 0.30 m/s, based on Equation 3.37.

4.5. Model Validation

In order to validate the accuracy of the model constructed during this thesis project, as well as to assess its prediction capability, experimental data regarding the initial feedstock and the final syngas composition from a gasification test in TU Darmstadt were used. To be more specific, the syngas composition of Table 4.2 was used for comparison for the results of the constructed model [3], while the initial feedstock composition (proximate and ultimate analysis) that was used as input data for the numerical model can be seen in Table 3.2. The syngas composition seen in Table 4.2 constitutes the ”Target” composition seen in the Figures 4.10 - 4.11.

Table 4.2: Syngas Composition from Experimental Data [3].

Component	**Vol%**
CO (dry)	17.3
H_2 (dry)	21.9
CO_2 (dry)	50.4
CH_4 (dry)	6.9
H_2O	34.2

The distribution of gaseous agents across the nozzles that yielded a syngas composition similar to the experimental data can be seen in Table 4.3:

Table 4.3: Mass distribution per nozzle for O_2 and H_2O

Nozzle	**O_2 Distribution (wt%)**	**H_2O Distribution (wt%)**	**Location in the gasifier**
N2	–	20	Bed
N3	45	20	Bed
N4	33	20	Bed
N5	12	20	Freeboard
N6	10	20	Freeboard
N7	–	–	Freeboard

Looking at Table 4.3, one can notice that the mass ratio of O_2 between the nozzles in the bed and in the freeboard is: $\frac{78}{22} = 3.55$, which is in accordance with the experimental results from the study used for validation [3].

The syngas composition that was derived from the numerical model can be seen in Figures 4.10 and 4.11, where it is compared with the experimental results from the TU Darmstadt facility.

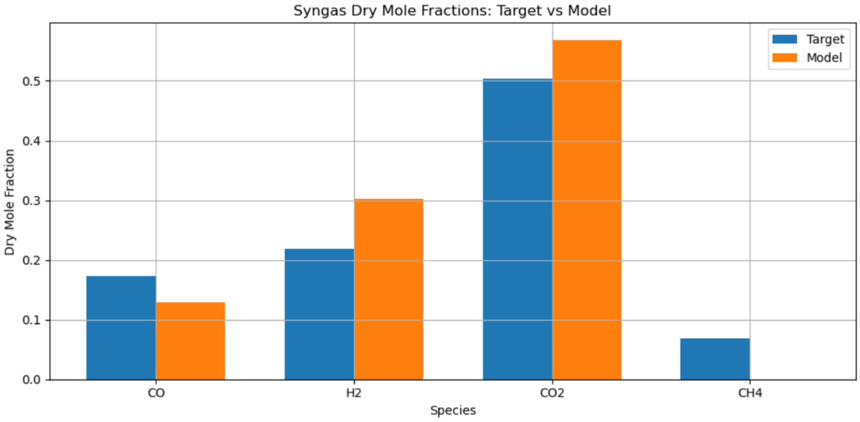

Figure 4.10: Dry syngas mole fractions: comparison between numerical results and experimental data.

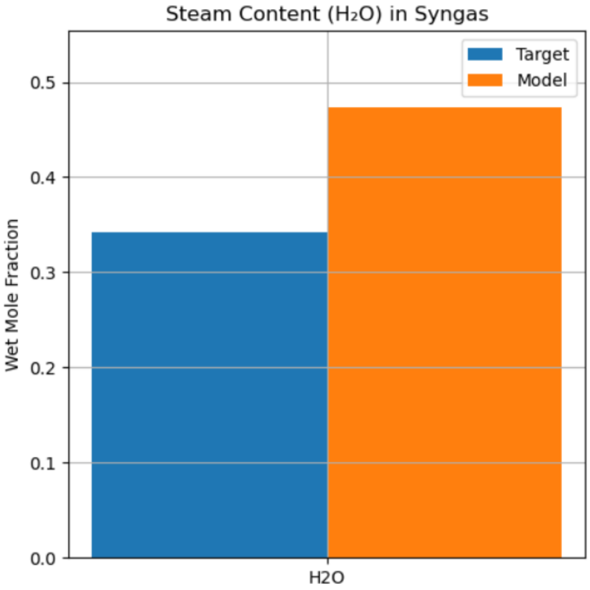

Figure 4.11: Steam mole fraction in the syngas: comparison between numerical results and experimental data.

As can be seen from Figure 4.10, the final syngas product from the experimental results has a lot of CO_2. The reason behind this very high percentage of CO_2 in the final syngas product is the use of carbon dioxide as an inert gas (instead of N_2 which is used in many experimental setups) for seal gas applications. In addition, since pilot-scale gasifiers experience higher heating losses than when they are at industrial-scale [101], a higher fraction of carbon must be combusted via the exothermic reaction $C + O_2 \longrightarrow CO_2$, in order to compensate for this heat loss. This helps to sustain the required temperature in the gasifier, but also raises the amount of CO_2 found in the final syngas product.

Looking at Figures 4.10 and 4.11, it can be concluded that the numerical model that has been developed, reasonably captures the behavior of the gasifier. When comparing the numerical results and the experimental set of data, it is observed that the model slightly overestimates the final composition of H_2O, H_2 and CO_2, while underestimates the CO content. Notably, the model fails to reproduce the CH_4 content of the syngas, whose concentration is negligible in the final product, contrary to the experimental results that report a value of CH_4 around 6.9 %. This difference between the numerical and experimental results suggests that the methane is being entirely reformed and consumed during the gasification process. As shown in Figure 4.12, methane depletes to zero inside the fluidized bed, due to the fast kinetics of methane reforming and methane oxidation reactions (see Reactions R3 and R9 in Table 3.1), producing mainly H_2 and CO, which are then subsequently consumed through further reactions. Under normal conditions, the steam methane reforming reaction requires temperatures above 800 ° C [102] to proceed effectively, which makes its complete depletion at just 751 ° C unrealistic. Therefore, it is safe to assume that the kinetics applied overestimate the consumption of CH_4, which exceeds realistic depletion.

Mole Evolution of Species along the Fluidized Bed

In Figure 4.12, the evolution of the total moles of each species along the height of the bed is illustrated.

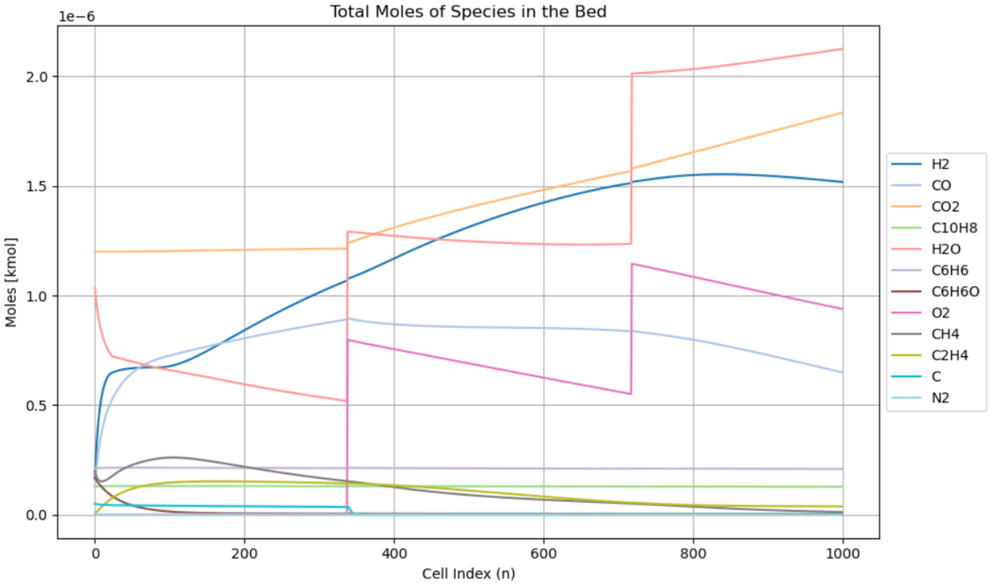

Figure 4.12: Evolution of moles of species in the bed, from the emulsion and bubble phase combined.

In Figure 4.13, a closer view of the mole quantity profiles along the fluidized bed for $C_{10}H_8$, C_6H_6, C_6H_6O, CH_4, C_2H_4 and C is provided.

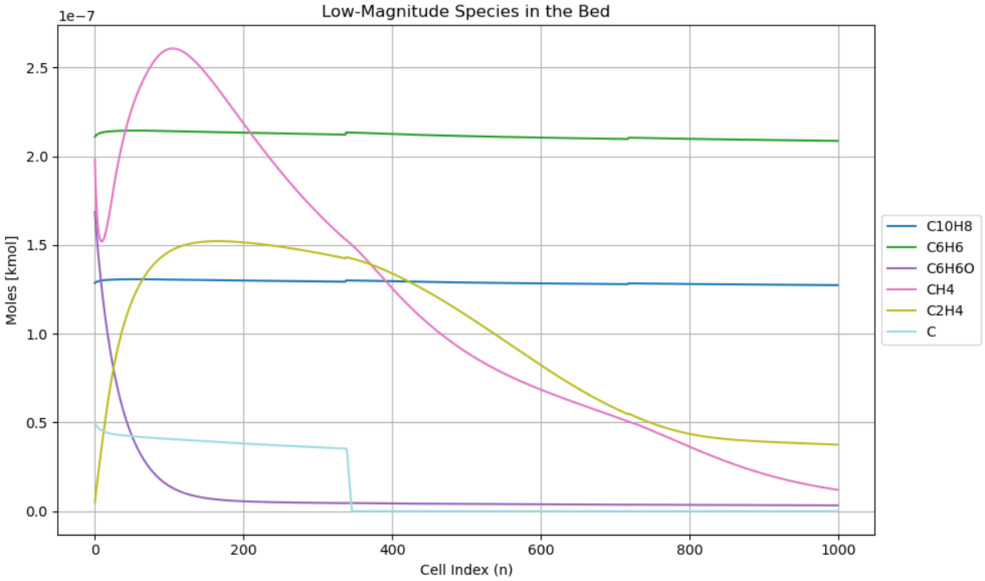

Figure 4.13: Zoomed-in depiction of mole quantity curves in the bed for $C_{10}H_8$, C_6H_6, C_6H_6O, CH_4, C_2H_4 and C.

The steady and substantial increase in the quantity of H_2 can be attributed to a combination of gasification, reforming and cracking reactions taking place throughout the bed, such as steam gasification of char ($C + H_2O \longrightarrow CO + H_2$), methane oxidation ($CH_4 + O_2 \longrightarrow CO + 2\,H_2$), and tar reforming reactions ($C_6H_6O + 2\,H_2O \longrightarrow 3\,CO + C_2H_4 + CH_4 + H_2$).

In the beginning of the fluidized bed, the amount of CO_2 remains relatively stable, but starts rising steadily after the nozzle N3 (cell index 338). At the nozzle N3, O_2 is injected at a significant amount, which starts the oxidation of carbon monoxide to carbon dioxide ($CO + 0.5\,O_2 \longrightarrow CO_2$), also validated by the gradual decrease of the CO quantity from that moment onward.

Meanwhile, H_2O exhibits a declining trend in the bottom region of the fluidized bed, probably attributed to the gasification and reforming reactions that steam participates in (such as $C + H_2O \longrightarrow CO + H_2$, $CH_4 + H_2O \longrightarrow CO + 3\,H_2$). At cell indices corresponding to nozzles N3 and N4 (338 and 718 respectively), the quantity of H_2O increases, due to the discontinuous nozzle injections at these points.

Similar to the trend displayed by H_2O, O_2 also shows sharp increases at the nozzle cell indices, which significantly increase its quantity. The injections of O_2 are followed by its depletion, as it reacts with other gaseous species and tars (e.g., $CH_4 + 0.5\,O_2 \longrightarrow CO + 2\,H_2$, $C_6H_6O + 4\,O_2 \longrightarrow 6\,CO + 3\,H_2O$).

Methane CH_4 and ethylene C_2H_4 exhibit early peaks, followed by a steady decline for both species which can be attributed to the cracking of tar species C_6H_6O as it reacts with steam ($C_6H_6O + 2\,H_2O \longrightarrow 3\,CO + C_2H_4 + CH_4 + H_2$) or the methanation reaction (for the case of CH_4) (see also Figure 4.13). Their subsequent removal occurs due to oxidation or reforming reaction with H_2O.

Tar species such as $C_{10}H_8$ and C_6H_6 exhibit significantly slower depletion profiles, in line with their lower reactivity and slower reforming and oxidation kinetics (see also Figure 4.13). A small peak is exhibited at cell 338, where nozzle N3 is located. The injection of O_2 and H_2O causes a rise in H_2 production, which favours Reaction R13 of Table 3.1, slightly increasing C_6H_6. In addition, a small increase for $C_{10}H_8$ is witnessed due to Reaction R11 of Table 3.1 (C_6H_6O -> $CO + 0.4\ C_{10}H_8 + 0.15\ C_6H_6 + 0.1\ CH_4 + 0.75\ H_2$). Contrary to that, phenol (C_6H_6O) seems to crack and decompose faster, due to its faster reaction rates with both steam and oxygen (see also Figure 4.13).

Solid carbon (C) decreases very gradually until the nozzle N3 (cell index 338), where the incoming O_2 and H_2O lead to its quick consumption, through its oxidation and gasification reactions.

Overall, the trend of the evolution of the different species aligns with the expected behavior and kinetic pathways, reflecting the complex phenomena and interplay that takes place between the different reactions. In addition, the model successfully captures the mass dynamics observed near the nozzle injection points, and how this controls the final species' concentrations.

Mole Fractions of Species along the Fluidized Bed

Based on the evolution of moles of all the species inside the fluidized bed, the graph portraying the evolution of the species' mole fractions (Figure 4.14) is created.

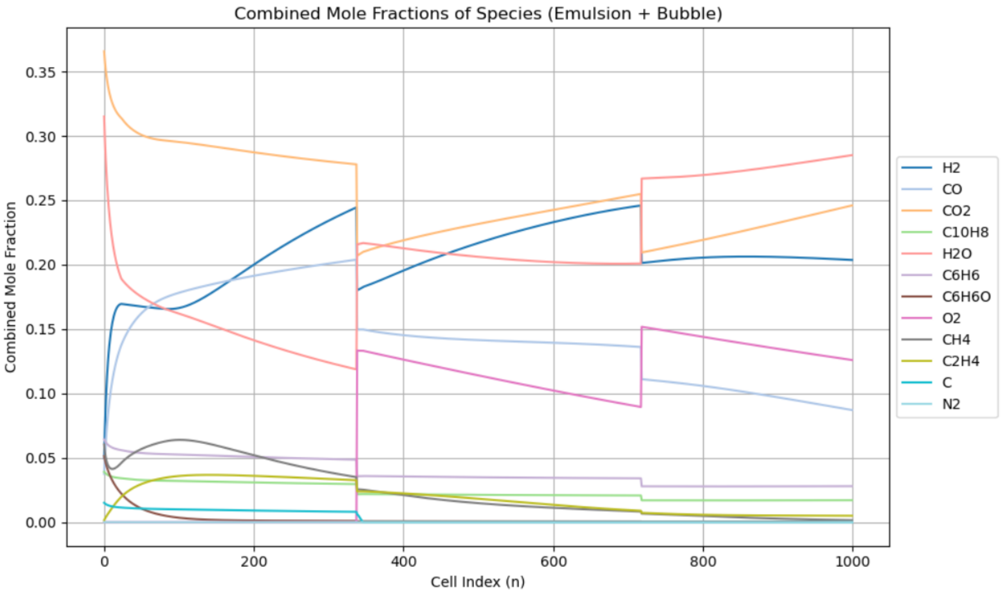

Figure 4.14: Evolution of mole fractions of species in the bed, from the emulsion and bubble phase combined.

In Figure 4.19, a closer view of the mole fraction profiles in the fluidized bed for $C_{10}H_8$, C_6H_6, C_6H_6O, CH_4, C_2H_4 and C is provided.

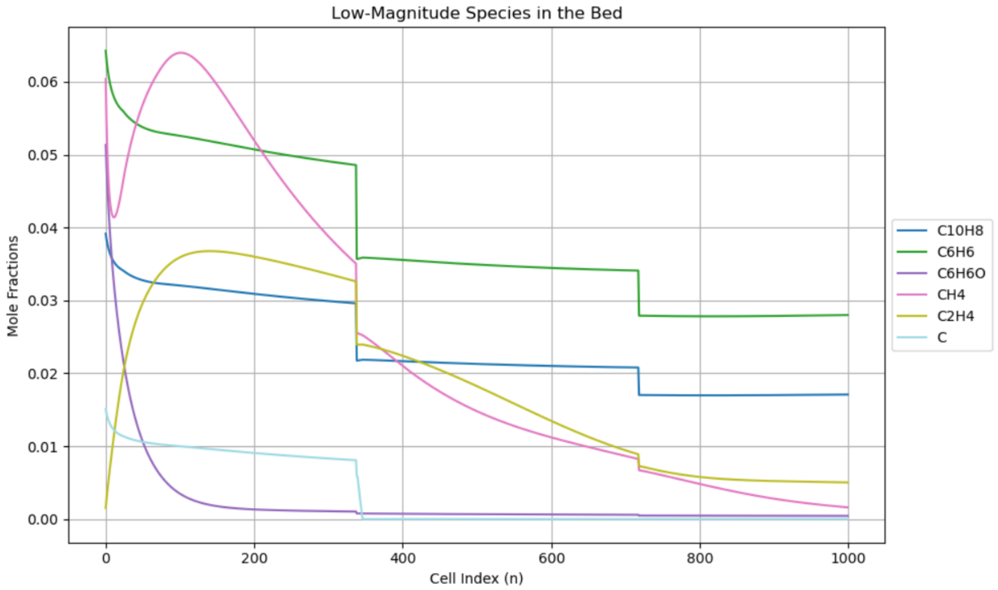

Figure 4.15: Zoomed-in depiction of mole fraction curves in the bed for $C_{10}H_8$, C_6H_6, C_6H_6O, CH_4, C_2H_4 and C.

It is important to note, that even though some spikes or dips are witnessed in Figure 4.14, that does not necessarily translate to spikes or dips in the mass or moles of these species. Since the mole fractions are normalized and must always sum up to unity, the injection of gasification agents through the nozzles can cause the mole fraction of existing species to decrease, even if they are not actually being consumed. This occurs when there is an external source or a sink term. In other cases, a change in the mole fraction reflects an actual consumption or production of the relevant species. For that reason, the need to interpret and examine mole fraction plots alongside mole quantity plots is highlighted. In any case, Figure 4.14 is useful in showcasing how the composition of the gas phase changes along the fluidized bed, and how the injections of gasification agents through the nozzles affects the final syngas composition. The trends displayed in Figure 4.14 are consistent with the depicted data in Figure 4.12, but now reveal the relative composition of the gas phase (emulsion gas and bubbles combined) at each location in the bed.

For example, the gradual increase of H_2 in the bed that was observed earlier, now translates to a growing mole fraction of H_2 in the lower and middle regions of the bed, but after nozzle N4 slowly declines and reaches a plateau. This slight decrease in the mole fraction indicates that the rate of growth of other species, such as CO_2 or H_2O is stronger than the one for H_2. Similarly, for CO, while it initially increases in both absolute and relative terms, in the middle area of the bed, its mole fraction decreases significantly, although its absolute mass (or quantity in moles) remains constant. This behavior can be attributed to the rising mole fraction of CO_2, which significantly increases after the injection of O_2 in nozzle N3.

Spikes in the mole fractions of H_2O and O_2 are clearly observed, which correspond to the incoming mass flows of these species through the injection nozzles N3 and N4, followed by a steady decline as they are reacting with other species and being consumed due to the gasification and oxidation reactions.

The dips witnessed for tar species $C_{10}H_8$ and C_6H_6 at the nozzle injection points (see Figure 4.15), don't correspond to their depletion of mass, but is rather an outcome of the renormalization of the mole fractions, as previously discussed. Regarding methane CH_4 and ethylene C_2H_4, the mole fractions of the species display an early peak, as also shown in Figure 4.12, followed by a gradual decline (see Figure 4.15). As for the species C and C_6H_6O, their mole fraction profiles are similar to their mole quantity curves in Figure 4.13.

Mole Evolution of Species along the Freeboard

Similarly to Figure 4.12, in Figure 4.16 the moles of the species in the freeboard can be seen, so as to really understand how the species get produced or consumed in this region.

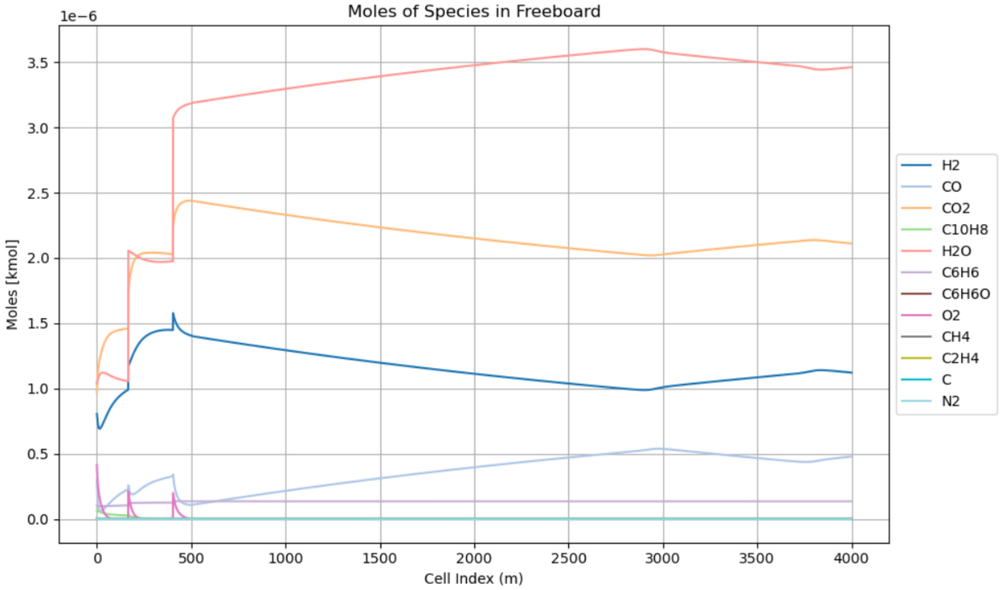

Figure 4.16: Evolution of the moles of species in the freeboard.

In Figure 4.17, a closer view of the mole quantity curves in the freeboard for $C_{10}H_8$, C_6H_6, C_6H_6O, CH_4, C_2H_4 and C is provided.

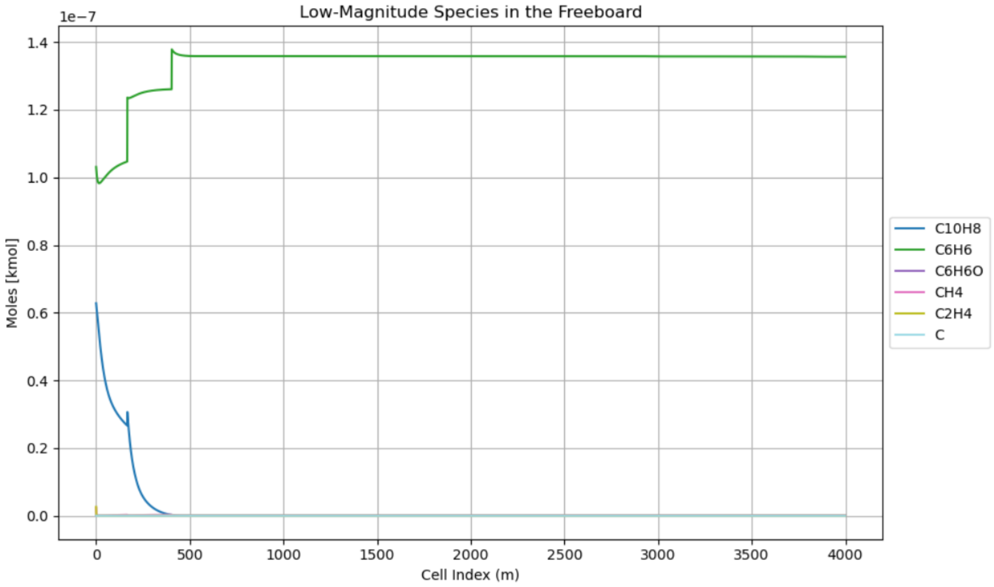

Figure 4.17: Zoomed-in depiction of mole quantity curves in the freeboard for $C_{10}H_8$, C_6H_6, C_6H_6O, CH_4, C_2H_4 and C.

As can be seen in Figure 4.12 or 4.14, the gas that exits the fluidized bed and enters the freeboard is rich in H_2, H_2O, CO_2 and CO to a lesser extent. The amount of H_2O initially drops slightly, due to the cracking reaction of $C_{10}H_8$. Two sharp spikes are witnessed at the freeboard cells 167 and 404, which is attributed to the injection of steam through the nozzles N5 and N6. Around the freeboard cell m = 500, the reverse water-gas shift reaction seems to take hold, initially producing CO and H_2O, and consuming H_2 and CO_2 ($CO_2 + H_2 \rightleftharpoons CO + H_2O$), which however switches around cell m = 3000.

The profile of CO_2 initially displays an increase due to oxidation reactions that occur with the incoming O_2 from the nozzles. Around the cell m = 500, a slight decline in the trend of CO_2 is witnessed, due to the reverse water-gas shift reaction. The domination of the WGSR reaction in the freeboard is also validated and aligns with the trend of the other participating species (H_2, CO and H_2O as previously discussed). Similarly to H_2O, the spikes in the profile of O_2 refer to the incoming mass from the nozzles N5 and N6, which is then consumed very fast by the oxidation reactions.

Tar compound C_6H_6 remains at a low level in the bed, not reacting completely, while $C_{10}H_8$ gets consumed away by Reactions R13 and R14 from Table 3.1 (see Figure 4.17). The consumption of $C_{10}H_8$ through Reaction R13 explains also the small production of C_6H_6 that is witnessed in this area of the freeboard ($C_{10}H_8$–> 6.5 C + 0.5 C_6H_6 + 0.5 CH_4 + 1.5 H_2). The species C_6H_6O, CH_4, C_2H_4 and C, have already been completely consumed inside the fluidized bed.

Overall, the species exiting the freeboard are mostly gases, with most tars having been cracked and converted to lighter species. The regime in the freeboard ends up being dominated by the reverse water-gas shift reaction leading to an equilibrium between the gases, which also highlights the need for high residence time in order to reach this phase.

Mole Fractions of Species along the Freeboard

In Figure 4.18 the evolution of the mole fractions of the species in the freeboard can be observed.

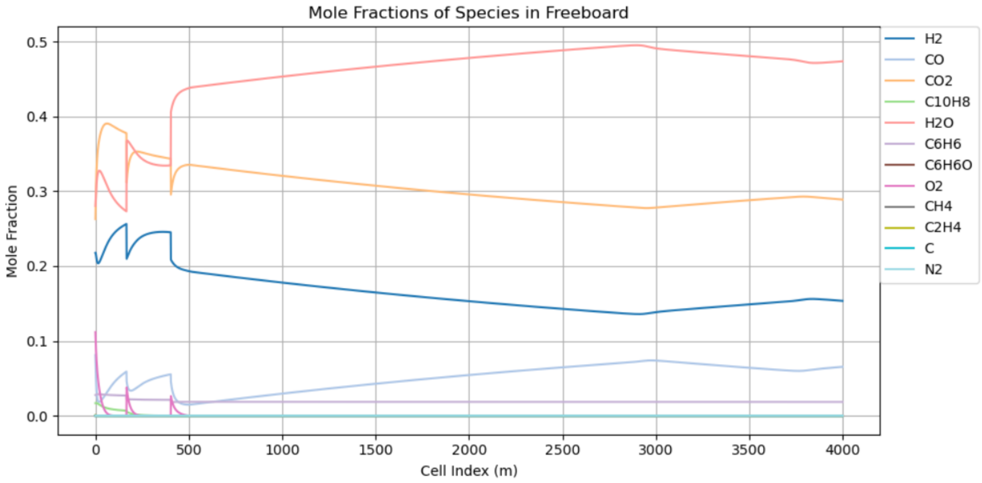

Figure 4.18: Evolution of mole fractions of species in the freeboard.

In Figure 4.19, a closer view of the mole fraction profiles in the freeboard for $C_{10}H_8$, C_6H_6, C_6H_6O, CH_4, C_2H_4 and C is provided.

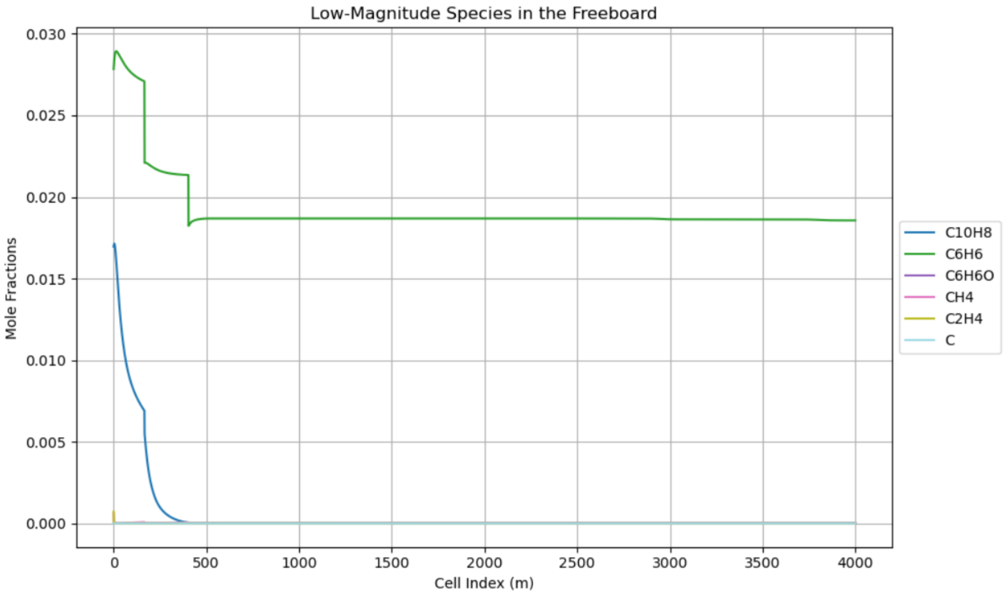

Figure 4.19: Zoomed-in depiction of mole fraction curves in the freeboard for $C_{10}H_8$, C_6H_6, C_6H_6O, CH_4, C_2H_4 and C.

Regarding the mole fraction profile of O_2 in the freeboard, two distinct spikes are observed at cell indices 167 and 404, which correspond to the mass increase due to the nozzle injections of oxygen. Immediately after these injections, the oxygen is quickly depleted, with its mole fraction dropping quickly, due to its involvement in oxidation reactions.

As for the profile of the mole fraction of CO, it closely resembles the trend of its total mole quantity from Figure 4.16, initially increasing and then dropping when oxygen and steam are injected through the nozzles, due to the oxidation and reforming reactions. Finally, its mole fraction increases as the reverse water-gas shift reaction dominates, which is also visible in the similar trend of H_2O.

The profile of the mole fraction of H_2 displays a gradual increase, followed by a drop and a subsequent recovery, which does not correspond to the consumption of H_2, but rather to the normalization constraint of the mole fractions. At the point where the drop in the mole fraction of H_2 is witnessed, an increase in the mole fraction of O_2 and H_2O occurs because of the nozzles, reducing the relative share of the former species. Similarly to H_2, the profile of CO_2 also displays two dips, which do not correspond to its depletion.

The mole fraction of $C_{10}H_8$ gradually declines, consistent with the trend presented in Figure 4.17. In contrast, C_6H_6 displays a decreasing mole fraction profile (see Figure 4.19), different than the one shown in Figure 4.17. This discrepancy is attributed to the fact that the mole fractions represent the proportion of each species in the total mixture, and therefore a larger absolute increase in another species, can cause the mole fraction of C_6H_6 to decrease,

Carbon Conversion Efficiency

The carbon conversion efficiency, which represents how much of the initial char released from pyrolysis reacts with other carbonaceous species, was found to be 100%. This result can be attributed to the fact that carbon is being treated as a pseudo-gaseous species, and not as a real solid-phase component, which likely leads to an overestimation of the reactivity of carbon. In addition, the current model does not take into account the bottom ash exiting the gasifier, or the entrained char particles carried with the syngas, which both represent mechanisms for incomplete carbon conversion in real-life applications. In practice, the carbon conversion efficiency in a bubbling fluidized bed gasifier typically ranges between 70 % - 90%, depending on the type of fuel used (higher conversion rates are usually achieved for fossil-based fuels, while lower are observed for waste-derived fuels) [16, 103].

4.6. Mass Balance Validation

In Figures 4.20 and 4.21 the preservation of mass is displayed across the bed and the freeboard respectively.

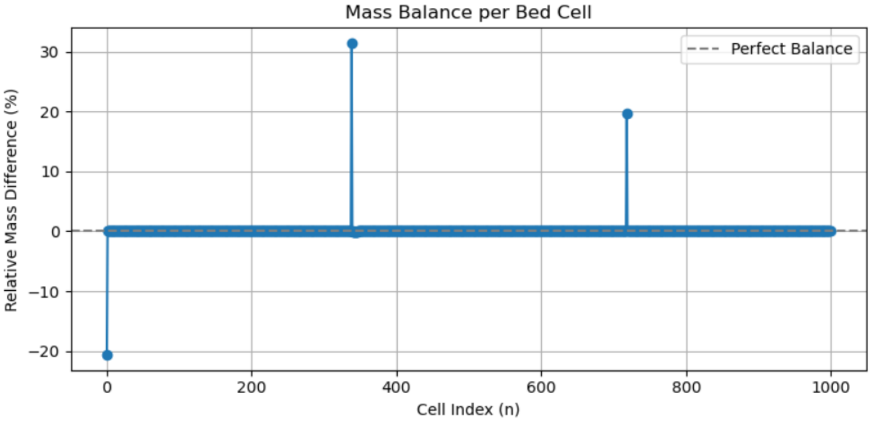

Figure 4.20: Preservation of mass balance across the bed.

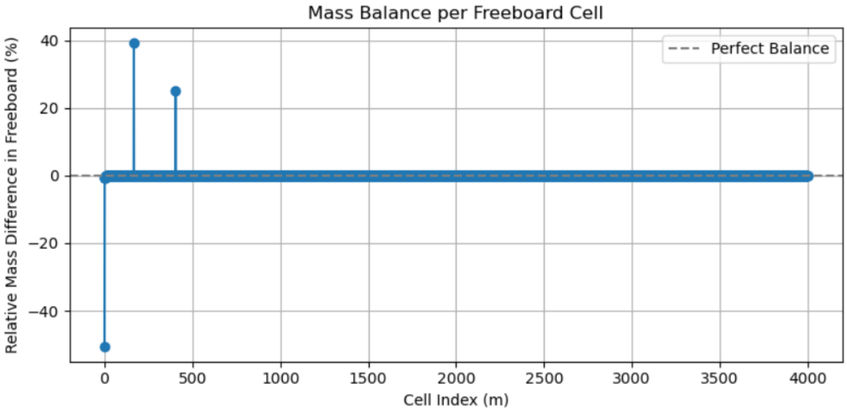

Figure 4.21: Preservation of mass balance across the freeboard.

In general, it is visible that mass balance is obeyed, with the only exception of three spikes in each Figure. The spikes in the relative mass balance that are observed in the bed and the freeboard correspond to the cells where nozzles are located (cell indices 167 and 404 for the bed, and 338 and 718 for the freeboard) as well as the first cell. The spikes at the nozzle positions are attributed to the modeling approach of the mass balance, where the parameters that are tracked are the mass entering from the cell below and the mass exiting from that cell. Therefore, the mass being injected through the nozzles is not taken into account, which leads to these visible spikes. At cell 0, both of the bed and the freeboard, the spikes in the mass balance are likely due to another modeling mechanism, the mass clipping. In the bed cell 0, the initial mass is introduced through the biomass pyrolysis products (for the emulsion phase) and through the mass inflow of CO_2 (for the bubble phase), and therefore there is no upstream cell considered that provides a convective mass inflow (see Section 3.3.5 for the mass balance ODEs). Similarly, for the first cell of the freeboard, there is no upstream cell considered that provides the convective mass inflow to the cell, but the initial mass is introduced through the last cell of the fluidized bed. In these cells, due to strong kinetics and numerical clippings of negative mass values, a portion of the initial mass gets lost. This phenomenon is captured by the negative spikes of the relative mass balance that are exhibited for cell 0.

In Figures 4.22 and 4.23, a closer view into the relative mass difference is provided for the fluidized bed and the freeboard respectively.

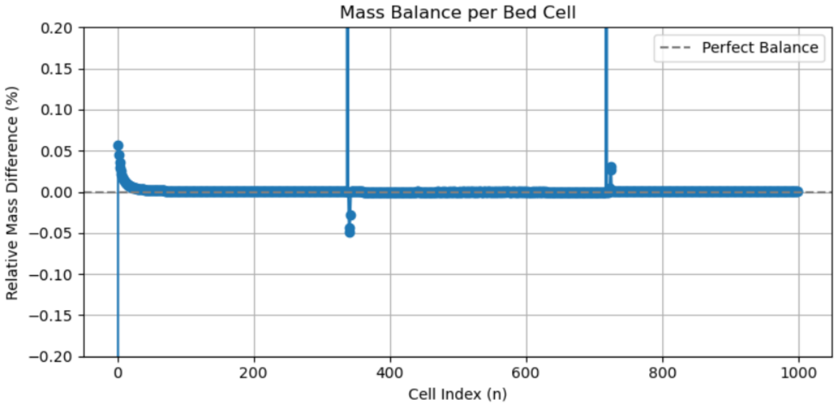

Figure 4.22: Zoomed-in depiction of relative mass difference per bed cell.

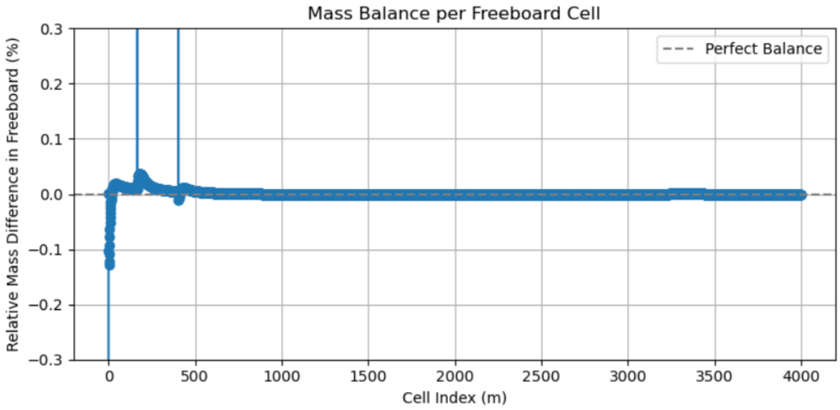

Figure 4.23: Zoomed-in depiction of relative mass difference per freeboard cell.

Excluding the localized spikes due to the nozzles, mass balance is kept within an approximately ± 0.05% and ± 0.1% deviation for the bed and the freeboard respectively. These small deviations are attributed to the mass clipping that is applied, when negative mass values occur. Overall, the deviations are not significant, proving that mass is preserved in the model.

4.7. Sensitivity Analysis

Since the accuracy of the constructed model is reasonably good, as previously proven, the model can be used to assess the effect of various parameters on the final syngas result and the gasification behavior. Therefore, in the current section, several different experiments of sensitivity analysis were conducted, in order to evaluate the influence of different conditions on the model.

4.7.1. Freeboard Temperature

Given the fact that the temperature in the freeboard during the experiments in TU Darmstadt, that this model is using as validation, is rather low - at just 751 ° C -, higher temperature levels were also tested out. The three different temperature profiles that were tried out were: 751 ° C (temperature of experimental campaign), 900 ° C and finally 1050 ° C. Keeping the gas distribution stable, with the same values as to what was mentioned in Section 4.5, the effect of different temperatures was examined.

The comparison of the syngas composition between the three tested freeboard temperatures can be seen in Figure 4.24.

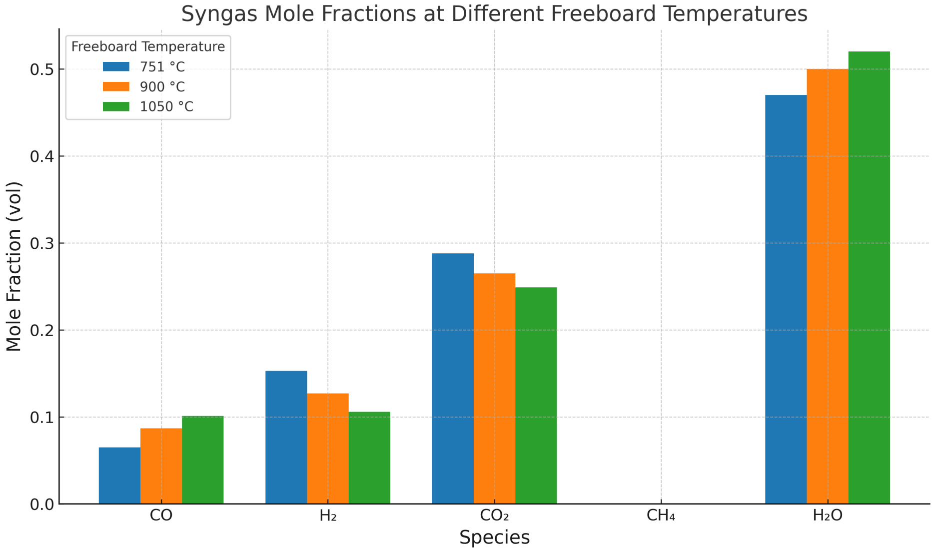

Figure 4.24: Wet syngas mole fractions at different freeboard temperatures

As can be seen from Figure 4.24, as the freeboard temperature increases, the content of the syngas in steam and carbon monoxide increases, while its content in H_2 and CO_2 decreases. This trend is consistent with the reaction mechanisms that are considered in the current model. In the freeboard, several endothermic reactions, such as the reverse water-gas shift reaction ($CO_2 + H_2 \longrightarrow CO + H_2O$), are favored by higher temperatures. Therefore, as the temperature increases, due to the Le Chatelier's principle for endothermic reactions, the equilibrium shifts more towards the products, and therefore CO and H_2O get produced. In addition, at higher freeboard temperatures, reactions such as the oxidation of hydrogen take place with much faster kinetics, contributing to the observed depletion of the reactant H_2 and increase of its H_2O content. While the species' trends displayed in Figure 4.24 are consistent with the thermodynamic expectations, it should be noted that the model is primarily governed by the chemical kinetic expressions, presented in Table 3.1. Hence, as the freeboard temperature increases, both the forward and the reverse rate of these Arrhenius-type reactions get favoured, leading to the final syngas compositions seen in Figure 4.24. Similarly to the model's results from Section 4.5, methane (CH_4) gets entirely reformed at all modeled temperatures. While this behavior is more reasonable for the higher temperatures (that favor the methane reforming reactions), the complete depletion of CH_4 at 751 ° C raises some eyebrows and is unexpected. Under normal conditions, at a low freeboard temperature of just 751 ° C, one would expect a higher CH_4 content. This leads to the conclusion that the kinetics of the methane reforming reactions must be unrealistically fast, causing an overestimation of the methane's consumption. Overall, the sensitivity analysis proves the small, but important effect that the freeboard temperature can have on the final syngas product. Since the sensitivity analysis test was conducted varying only the freeboard temperature, the carbon conversion efficiency within the bed remained unchanged, at full conversion.

4.7.2. Different Gas Distributions through the Nozzles

When operating at a constant pressure and temperature profile along the gasifier, the flowrates of incoming gasification agents and their distribution among the different nozzles play a significant role on the final syngas composition. The amount of incoming O_2 can be distributed among the N3, N4, N5 and N6 nozzles, while the incoming H_2O can be distributed among the N2, N3, N4, N5 and N6 nozzles. The fluidization agent CO_2 enters only through N1, so no sensitivity analysis can be conducted on this species.

Therefore the following gas distribution sensitivity tests, seen in Table 4.4, were conducted:

Table 4.4: Gas distribution profiles for steam and oxygen along different nozzles: comparison between two injection strategies.

Nozzle	Distribution 1 (Decreasing ↓)		Distribution 2 (Increasing ↑)		Location
	Steam (wt%)	O_2 (wt%)	Steam (wt%)	O_2 (wt%)	
N2	30	-	10	-	Bed
N3	25	40	15	10	Bed
N4	20	30	20	20	Bed
N5	15	20	25	30	Freeboard
N6	10	10	30	40	Freeboard

In Figure 4.25, the wet syngas mole fractions can be observed for different gaseous distributions that are applied. The ”Distribution 1” and ”Distribution 2” refer to the distributions displayed in Table 4.4, while the ”Original Run” refers to the gaseous distribution seen in Table 4.3.

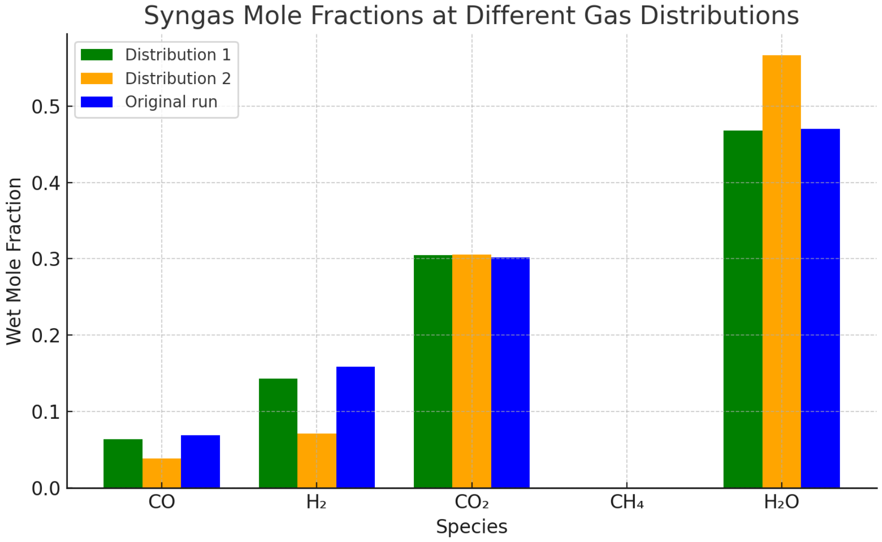

Figure 4.25: Wet syngas mole fractions at different gaseous distributions through the nozzles.

Comparing the results of ”Distribution 1” and the ”Original Run”, it is noticeable that the syngas composition does not change significantly. The similar trend in the syngas composition is reasonable, since both cases have a comparable overall gas distribution, with the most notable difference being witnessed in the distribution of steam. The revised Distribution 1 features more steam and slightly less oxygen injected in the bed, compared to the original run. This adjustment leads to a slightly lower content in H_2 and CO in the final syngas of ”Distribution 1”, higher content in CO_2, while the concentration of H_2O remains similar. These changes can be explained by the increased injection of steam in the bed, which favors reactions such as tar cracking and char gasification, releasing a higher amount of light gases (CO and H_2) early in the bed. However, due to the revised oxygen distribution profile, there is now more abundant oxygen in the freeboard, which oxidizes the gases, causing an increase in the content of CO_2 and a slight decrease of H_2 and CO.

The ”Distribution 2” of gasification agents, where more steam and oxygen is injected in the freeboard, leads to a final syngas product with a significantly higher H_2O content, while the concentration of CO and H_2 is decreased. This change is the result of higher availability of O_2 later in the gasifier (in the freeboard), where it reacts with CO and H_2, and oxidizes them forming CO_2 and H_2O. In addition, limited availability of steam in the lower regions of the reactor, limits reactions such as tar cracking or steam reforming, where these light gases would be formed. As a result, the steam is less effectively consumed, leading to its higher percentage in the final syngas product.

In both cases, the content of methane in the final syngas is depleted, similarly to the ”Original Run”.

4.7.3. Kinetic Parameters of Gasification Reactions

As was explained in Section 3.3.3, the final gasification reactions and their respective kinetic parameters used in this model, were collected from a variety of literature sources (see Table 3.1). The reason behind that choice, was the effort to establish a reaction pathway that accurately captures the gasification behavior of waste-derived feedstock. The kinetics of certain homogeneous reactions (i.e., H_2 oxidation or CO oxidation) were under-estimated, leading to an inaccurate and unrealistic final syngas composition. To address this problem, alternative reaction kinetics were examined. When a set of faster oxidation kinetics was tested, the incoming mass of O_2 through the freeboard nozzles got instantaneously consumed upon entering the reactor, leaving its mass being effectively zero throughout the freeboard region and no opportunity for it to react with the other species. In contrast, in Figure 4.26, the incoming mass of O_2 in the freeboard can clearly be observed under operation with more moderate oxidation kinetics, that were eventually used in the current version of the model and can be seen in Table 3.1.

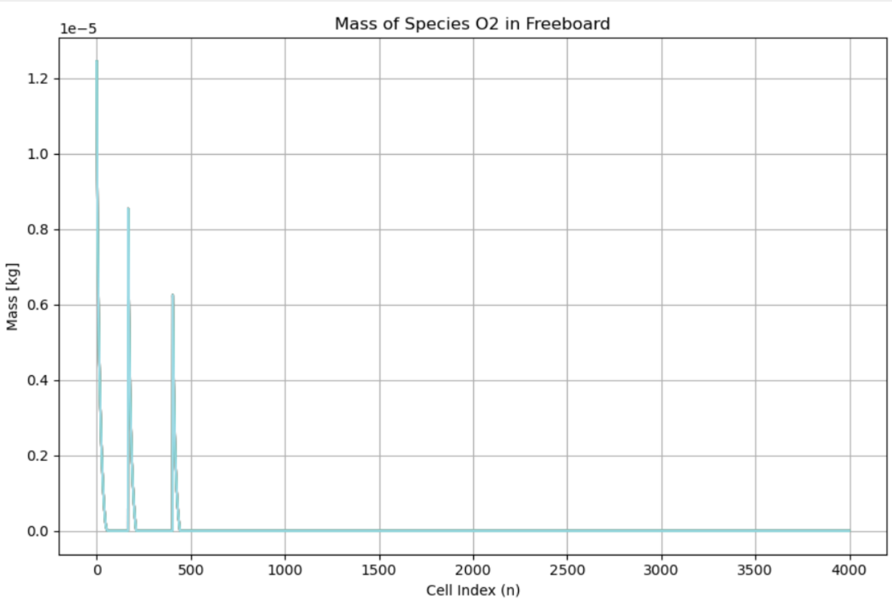

Figure 4.26: Spikes of mass of oxygen observed when entering through the nozzles of the freeboard.

Due to the sensitivity observed during our investigations, several reaction mechanisms were examined, and the final set of kinetics displayed in Table 3.1 was ultimately selected.

4.7.4. Initial Gasification Conditions

To assess the sensitivity of the final syngas composition on the initial inputs for the gasification model, a series of tests were carried out using alternative initial compositions. The initial conditions of the gasification model are provided by the pyrolysis model, and it has already been discussed that the results of the devolatilization process are realistic, but lie at the edge of the expected range. More reasonable and representative pyrolysis mass yield values were introduced in order to evaluate their influence on the final composition.

Therefore, using the same set of operating conditions, and only varying the outcome of the pyrolysis model, two different tests were conducted. The alternative pyrolysis data were derived from the study of Tokmurzin et al. (2020) [66], who examined the pyrolysis behavior of SRF feedstock under different temperatures.

The two different pyrolysis product yields that were used, were thus:

1. **Case 1**: gas = 37%, char = 16.5%, tars = 46.5%
2. **Case 2**: gas = 35.25%, char = 40.35%, and tars = 24.4%

The study of [66] only mentions the overall gas yield and doesn't go deep into the specific mass yield of each gaseous species. Therefore, for Case 1 and Case 2, the individual gas fractions that were used, were derived by proportionally scaling the original pyrolysis results (seen in section 4.1), so that the total gas yield matches for each case the gas yield that was reported by Tokmurzin et al.

Therefore, for each case, the individual mass yields of each species can be seen in Table 4.5:

Table 4.5: Different sets of pyrolysis product yields used for sensitivity analysis, based on Tokmurzin et al. [66]

Species	Case 1 [wt %]	Case 2 [wt %]
CO	4.89	4.66
CO_2	8.32	7.93
H_2	0.31	0.29
CH_4	8.61	8.21
H_2O	14.87	14.16
C	16.5	40.35
C_6H_6	15.5	8.13
C_6H_6O	15.5	8.13
$C_{10}H_8$	15.5	8.13

In Figure 4.27, the wet mole fractions of the syngas for different initial gasification conditions are depicted. The Case 1 and Case 2 of initial gasification conditions refer to the data displayed in Table 4.5, while the ”Original” refer to the original simulation of this model, with the initial gasification conditions displayed in section 4.1.

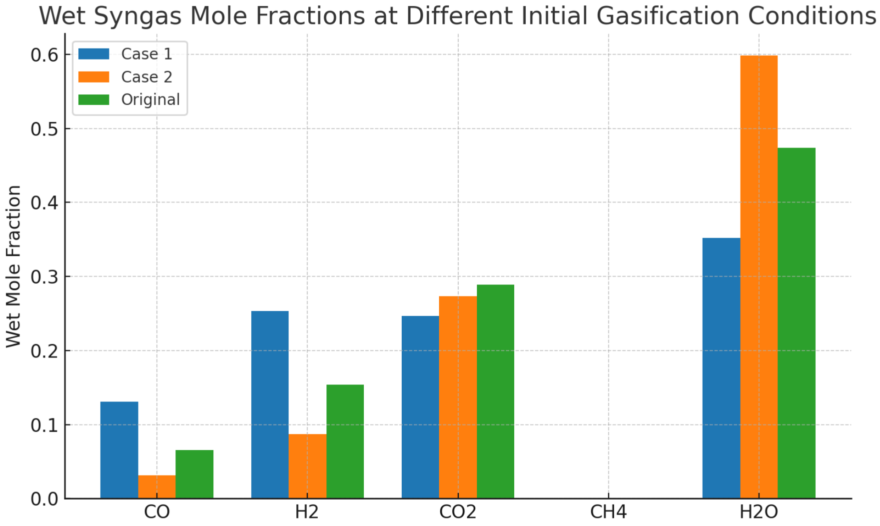

Figure 4.27: Wet syngas mole fractions at different initial gasification conditions.

In Case 1, which is characterized by a high tar yield (46.5%) and a low char yield (16.5%), the final syngas product is dominated by H_2O, H_2 and CO_2 regarding the gaseous products. The final concentration of CO is slightly over-predicted compared to the original simulation, while the content of H_2O is underestimated. These results can be attributed to the higher gas yield of the pyrolysis product (compared to the one considered for this model, seen in Table 4.1) and the high content in tars, which when cracked release CO and H_2. This, combined also with the lower content in char, leads to this lower amount of CO_2 (compared to the original simulation), which would otherwise be formed from char oxidation reactions, such as $C + O_2 \longrightarrow CO_2$.

In Case 2, which is characterized by a higher char content and lower tar content (compared to Case 1 and the original pyrolysis results), the final syngas composition features a high CO_2 yield, along with an underestimation of H_2 and an elevated H_2O concentration. The final concentration of CO (in wet basis) is lower than both the original simulation and the simulation with Case 1 initial gasification data. Compared to Case 1, the CO_2 content is now higher, slightly closer to the original simulation than before. The higher amount of CO_2 can be attributed to the higher char pyrolysis yield, which is then oxidized to form carbon dioxide. The lower yields of H_2 and CO witnessed can be linked to the lower percentage of tars in the initial conditions, which generally react with steam or oxygen to produce these lighter gases. The higher content in H_2O can also be explained by the decreased composition in tars and hence reduced tar cracking activity, which would otherwise consume steam.

Overall, the importance of the initial conditions to the numerical model is highlighted, showing how sensitive the model is to the gas, tar and char mass fractions that are provided to the model. Therefore, careful development of the pyrolysis model is critical, in order to ensure the accuracy of the final syngas predictions.

5

Conclusions

5.1. Conclusion

The current thesis project focused on the development and validation of a 1-D, two-phase model, for a bubbling fluidized bed gasifier operating on a waste-derived feedstock, such as Solid Recovered Fuel (SRF). The main focus of this project was on the hydrodynamics both in the fluidized bed and in the freeboard, as well as, the reaction kinetics in both these regions. A ”cell model” was constructed through the use of Python and the open-source software Cantera and the gasifier was discretized in small control volumes, where the local chemical reaction kinetics and hydrodynamics were solved for. The results of this model were validated against a set of experimental data, obtained during an SRF gasification test in 2020 in the gasifier setup of TU Darmstadt.

The model tried to bridge some literature gaps, by incorporating modeling aspects such as the freeboard chemistry and hydrodynamics, the release and creation of tars from pyrolysis, nozzle effects in the bed and the freeboard, as well as the implementation of a kinetic model tailored to waste-derived feedstock. In relation to the Research Question that was stated in Section 2.3.5, the present work successfully demonstrated that a 1-D model of a bubbling fluidized bed gasifier can integrate the aforementioned.

The use of some simplifying assumptions was made, such as the handling of solids as pseudo-gaseous species, the use of fixed temperatures in both regions of the gasifier or the implementation of a simplified, empirical pyrolysis model, which naturally affect the predictive capability of the model. Nevertheless, the model still managed to capture reasonably well the gasifier’s behavior. When the model’s predicted syngas composition results were compared to the experimental set of data that were used for validation, it was obvious that the model succeeded in predicting reasonably well the concentration of the major syngas species. The syngas’ content in H_2, CO, CO_2 and H_2O were generally predicted accurately, with a slight overestimation in the content of carbon dioxide, hydrogen and steam, and a corresponding underestimation of carbon monoxide. The most notable deviation in the model’s results was the complete depletion of CH_4 inside the bed, which was experimentally found to have a dry mole fraction value in the syngas of approximately 7 %, highlighting an overestimation of the kinetics of methane oxidation and reforming reactions.

A series of sensitivity analysis tests were then carried out in order to explore the impact of specific parameters on the model’s results. In particular, the increase of the freeboard temperature led to a rise in the CO and H_2O content in the final syngas, most likely attributed to the favoring of the reverse water-gas shift reaction with increasing temperature. In addition, different gas injection profiles through the nozzles were tested, showing that when the majority of the gasification agents is injected into the freeboard, a syngas with elevated levels of H_2O and CO_2 will be formed. The effect of different kinetic constants was also explored, which demonstrated their significant impact on the product distribution of the gasification process, highlighting the importance of their selection. Finally, two simulations with alternative initial gasification conditions were performed, which emphasized the need for an accurate pyrolysis model, as a wrong prediction of the pyrolysis yields would alter significantly the results.

Overall, it is safe to say that the model can reasonably approximate the performance of the experimental setup, and provide a solid basis for further simulations of gasification processes with SRF.

Several areas for future model development have been identified, which are discussed further in depth in Section 6.

5.2. Discussion

One of the main challenges that was faced during this project, was the difficulty of Cantera handling solids, as well as the numerical stiffness of the model. Regarding the treatment of the heterogeneous reactions, Cantera handles heterogeneous reactions (such as the char gasification reactions) through surface interfaces between the reacting species, such as a catalyst surface. These surfaces must be defined and usually considered as ”surface between two bulk phases, or along an edge at the intersection of two surfaces” [104], which doesn’t really align with how reactions occur in the fluidized bed setting. In a fluidized bed gasifier reactions occur across the whole volume of the reactor, not at fixed surfaces. The solid particles are suspended by the flowing gas, reacting with the gases as they move around them. Therefore, Cantera’s way of handling gas-solid reactions doesn’t really coincide with this, which led to the simplification being made where solids were treated as pseudo-gaseous species in order to overcome this obstacle.

As for the numerical stiffness of the system, this posed a significant challenge, as the model’s simulations would take significant time to complete and to reach convergence. Specific solvers were used for the integration of the mass balance equations, tailored to solving stiff systems and ordinary differential equations, which were however very computationally expensive. A large set of different relaxation factors, different number of maximum allowed iterations were tried out in order to make the model converge. In addition, the emulsion phase mechanism would struggle more to reach convergence than the bubble phase, which can probably be attributed to the larger set of equations occurring in the emulsion phase (due to the fact that the heterogeneous reactions take place there).

5.3. Reflection

As global temperatures are rising and the impacts of anthropogenic climate change become more and more evident and detrimental, the transition to a sustainable society seems more urgent than ever. This thesis project contributes to that transition by helping understand better the processes behind biomass gasification and advancing its modeling. Gasification has been proven a key technology for the production of syngas, and is able to handle a variety of feedstocks. Therefore, gasification can produce renewable syngas when biogenic or waste-derived feedstock is used. Syngas is a highly versatile building block that be used to produce other chemicals, such as sustainable aviation fuel, green methanol, or hydrogen. All of these products are essential for decarbonizing sectors which are hard to electrify (such as long distance transport, aviation and heavy industry). When gasification is paired with waste-derived feedstock (such as agricultural, industrial by-products or municipal waste), this process provides the opportunity to make use of materials that would otherwise be discarded. This allows for the carbon included in these materials to be emitted in an controlled way, and potentially carbon-neutral or even carbon-negative manner, while also simultaneously phasing out the use of fossil fuels. The development of a 1-D model of a bubbling fluidized bed for this thesis project can hence facilitate the optimization of producing renewable fuels, by making their production process more scalable and efficient. This thesis project aligns therefore with broader societal and environmental goals, such as clean energy development, climate change mitigation and sustainable urban spaces.

6

Future Work

In the present section, some possible topics that can be addressed for further development of the model will be discussed.

Numerical Improvements and Convergence Stability

As previously discussed in Section 4.2, it is evident that some cells of the bed and the freeboard are struggling with convergence more than the others. The is largely attributed to the introduction of the external mass inflow term in the mass balance ODEs, which has a significant value, and is hence causing this difficulty to reach convergence.

Some possible improvements that could be implemented on the code in order to reduce the computational cost would be:

1. **Adaptive under-relaxation**: Currently, a fixed value for the relaxation factor is being introduced in both the phases of the fluidized bed and in the freeboard, which could be further improved by defining a relaxation factor that is dynamically adjusted based on the difference between the previous and the current value for each iteration. This could probably facilitate convergence, by selecting a relaxation factor that is optimized and more case-specific.
2. **Local refinement in the grid**: A finer discretization in the regions with nozzle inflow, but a generally coarser grid, could reduce computational cost and simultaneously help improve the numerical stability of the model.

Reaction and Mass Transfer Limitations

Another important thing that should be implemented in a future version of the model would be the mass transfer limitations that could exist in the heterogeneous reactions between char, tar and the reacting gases. While it is common in literature to assume that the heterogeneous reactions are kinetically-controlled [50], rather than mass-transfer limited, in order to get a better, more realistic understanding of how the reactions proceed inside the reactor, a study of the potential mass transfer limitations would be essential.

Energy Balance and Temperature Profile

In addition, the integration of an energy balance in the model, could improve its reaction realism and its predictive capabilities. Currently, in the model, one uniform temperature is considered in the bed and another in the freeboard. While the assumption of a uniform temperature for the bed is reasonable, due to its well-mixed nature, for the freeboard this assumption seems to fall short, since larger temperature gradients are observed there. Therefore, the incorporation of an energy balance in the freeboard would significantly help with the calculation of the chemical kinetics.

Solids Handling and Carbon Mass Balance

What is more, currently, in the model, solid particles are treated as pseudo-gaseous species, as previously mentioned, and in the carbon mass balance only the upwards motion of the particles has been considered. However, in reality, solid particles also have a downward motion in the bed, which has not been taken into account, and could potentially affect the carbon mass balance in the fluidized bed.

Alternative Modeling Platforms

Although the use of Python, along with Cantera, has been a very useful tool in modeling in 1-D a bubbling fluidized bed gasifier, Cantera faces some limitations in handling reactions with solids, as has been previously discussed. Therefore, alternative approaches to this model are worth considering. Aspen Plus features a ”Fluidized Bed Reactor” module, which, alongside with a user-defined kinetic model written in Fortran, could be used to simulate 1-D behavior of the gasifier. The ”FluidBed” module, as it is called in the Aspen Plus environment, describes an isothermal fluidized bed, which considers and models the 1-D fluid dynamics of the process and the solids entrainment in the freeboard [105]. It can take into account parameters, such as the particle size, geometry of the reactor, additional gas supply and the effect of chemical reactions on the fluid-dynamics and reverse [106]. While these are parameters that have already been considered in the current model, the Aspen Plus module seems to be able to handle solids more successfully, which is where Cantera lacks in power. However, it should be mentioned that Aspen Plus cannot account for the localized effects of the nozzles along the height of the reactor. Another possible alternative could be the use of open-source software MFIX - Multiphase Flow with Interphase eXchanges [107], which has been developed by NETL (National Energy Technology Laboratory), to model multiphase flow reactors. The MFIX software is particularly well-suited for gas-solid interactions, offering several different modeling approaches that deal with fluids and solids, such as the Two-Fluid Model, the Discrete Element Model, the Coarse Grain Particle etc. MFIX supports user-defined subroutines, as well as specific initial and boundary conditions (where the nozzle effect could be introduced) [107], which could make it an interesting candidate for this modeling purpose.

Pyrolysis Modeling

In addition, although pyrolysis is commonly considered as instantaneous in setups like the one considered in this model, incorporating the pyrolysis kinetics could improve the accuracy of the overall model and represent a more realistic and accurate species release. Given the fact that the importance of the initial conditions has already been proven in Section 4.7.4, the need for a more realistic and consistent pyrolysis model is highlighted.

Reaction Kinetics for Plastic Feedstocks

Furthermore, most of the gasification reaction kinetics used in this study have been derived from literature focused on the use of biomass as feedstock. Although Bhattarai et al. [60] also proposed an empirical kinetic model for municipal plastic waste as feedstock, most of the available literature still focuses on fossil fuels and, more recently, increasingly on biogenic feedstock. However, as previously discussed in Section 4.7.3, even within the study with plastic feedstock, some of the proposed kinetic expressions were found to be unrealistic, as they failed to accurately capture the reaction behavior. This pinpoints the need to revise and update such expressions with more consistent and representative kinetics, that capture better the characteristics of such gasification reactions.

Other Aspects to Explore

Finally, as was previously discussed in Section 2.3.4, two additional areas in fluidized bed modeling that call for further development, are the effects of materials, such as fuel ash, on the catalytic activity of reactions, as well as, a more realistic char model, that accounts for its full elemental composition.

References

[1] International Energy Agency. ”World Energy Outlook 2018”. Tech. rep. Licence: CC BY 4.0. Paris: International Energy Agency (IEA), 2018. URL: `https://www.iea.org/reports/world-energy-outlook-2018`.

[2] D. G Goodwin, H. K Moffat, I. Schoegl, R. L Speth, and B. W Weber. “Cantera: An Object-oriented Software Toolkit for Chemical Kinetics, Thermodynamics, and Transport Processes”. 2024. DOI: `10.5281/ZENODO.14455267`. URL: `https://zenodo.org/doi/10.5281/zenodo.14455267`.

[3] E. Langner, J. Kaltenmorgen, C. Heinze, J. Ströhle, and B. Epple. “Fluidized bed gasification of solid recovered fuels in a 500 kWth pilot plant”. In: *Fuel* 344 (2023), p. 127901.

[4] S. Hamel. “PhD Thesis”. PhD thesis. University of Siegen, 2001. ISBN: 3-18-346906-5.

[5] International Energy Agency. ”World Energy Outlook 2024”. Tech. rep. Licence: CC BY 4.0. Paris: International Energy Agency (IEA), 2024. URL: `https://www.iea.org/reports/world-energy-outlook-2024`.

[6] M. Beirow, A. M. Parvez, M. Schmid, and G. Scheffknecht. “A detailed one-dimensional hydrodynamic and kinetic model for sorption enhanced gasification”. In: *Applied Sciences* 10.17 (2020), p. 6136.

[7] European Commission. ”Causes of Climate Change”. Accessed: 2025-02-03. 2025. URL: `https://climate.ec.europa.eu/climate-change/causes-climate-change_en#:~:text=CO2%20produced%20by%20human,industrial%20level%20(before%201750)`.

[8] NASA Global Climate Change. ”Global Temperature | Vital Signs of the Planet”. Accessed: 2025-01-24. 2025. URL: `https://climate.nasa.gov/vital-signs/global-temperature/?intent=121#:~:text=Overall%2C%20Earth%20was%20about%202.45,change%20in%20global%20surface%20temperatures.`.

[9] BBC News. ”Climate change: IPCC report is ’code red for humanity’ ”. Accessed: 2025-01-24. 2021. URL: `https://www.bbc.com/news/science-environment-58073295`.

[10] Wikipedia contributors. ”Bioenergy”. Tech. rep. Accessed on 14 May 2025. San Francisco, CA: Wikipedia, The Free Encyclopedia, 2025. URL: `https://en.wikipedia.org/wiki/Bioenergy`.

[11] International Energy Agency. ”An Updated Roadmap to Net Zero Emissions by 2050”. `https://www.iea.org/reports/world-energy-outlook-2022/an-updated-roadmap-to-net-zero-emissions-by-2050`. Accessed: 2025-04-11. 2022.

[12] ECOS Environmental Consultants. *What is SRF? Definition of SRF*. Accessed: 2025-06-23. n.d. URL: `https://www.ecos.ie/glossary/what-is-srf-definition-of-srf/`.

[13] Clarity Eco. *What is Solid Recovered Fuel (SRF)?* Accessed: 2025-06-23. Clarity Eco. URL: `https://clarity.eco/knowledge/what-is-rdf-srf/`.

[14] U.S. Energy Information Administration. ”Biomass Explained”. `https://www.eia.gov/energyexplained/biomass/`. Accessed: 2025-04-11. 2023.

[15] W. J. Liu and H. Q. Yu. “Thermochemical Conversion of Lignocellulosic Biomass into Mass-Producible Fuels: Emerging Technology Progress and Environmental Sustainability Evaluation”. In: *ACS Environmental Au* 2.2 (Dec. 2021), pp. 98–114. ISSN: 2694-2518. DOI: `10.1021/acsenvironau.1c00025`. URL: `http://dx.doi.org/10.1021/acsenvironau.1c00025`.

[16] D. Krause, P. Herdel, J. Ströhle, and B. Epple. “HTW™-gasification of high volatile bituminous coal in a 500 kWth pilot plant”. In: *Fuel* 250 (Aug. 2019), pp. 306–314. ISSN: 0016-2361. DOI: `10.1016/j.fuel.2019.04.014`. URL: `http://dx.doi.org/10.1016/j.fuel.2019.04.014`.

[17] G. J Stiegel and R. C Maxwell. “Gasification technologies: the path to clean, affordable energy in the 21st century”. In: *fuel processing technology* 71.1-3 (2001), pp. 79–97.

[18] M. S. Masnadi, J. R Grace, X. T. Bi, C. J. Lim, N. Ellis, Y. H. Li, and A. P. Watkinson. “Single-fuel steam gasification of switchgrass and coal in a bubbling fluidized bed: A comprehensive parametric reference for co-gasification study”. In: *Energy* 80 (2015), pp. 133–147.

[19] G. Mirmoshtaghi. “Biomass gasification in fluidized bed gasifiers: Modeling and simulation”. PhD thesis. Mälardalen University, 2016.

[20] J. Gil, M. P Aznar, M. A. Caballero, E. Francés, and J. Corella. “Biomass gasification in fluidized bed at pilot scale with steam- oxygen mixtures. Product distribution for very different operating conditions”. In: *Energy & Fuels* 11.6 (1997), pp. 1109–1118.

[21] J. Sanchez-Hervas, I. Ortiz, V. Martí, and A. Andray. “Removal of organic sulfur pollutants from gasification gases at intermediate temperature by means of a zinc–nickel-oxide sorbent for integration in biofuel production”. In: *Catalysts* 13.7 (2023), p. 1089.

[22] Y. Bai and H. Si. “Experimental study on feeding characteristics of conical bottom pneumatic spout feeder for biomass pyrolysis”. In: *Chemical Engineering and Processing - Process Intensification* 166 (Sept. 2021), p. 108490. ISSN: 0255-2701. DOI: `10.1016/j.cep.2021.108490`. URL: `http://dx.doi.org/10.1016/j.cep.2021.108490`.

[23] C. Loha, S. Gu, J. De Wilde, P. Mahanta, and P. K. Chatterjee. “Advances in mathematical modeling of fluidized bed gasification”. In: *Renewable and Sustainable Energy Reviews* 40 (2014), pp. 688–715.

[24] A. A. Jain, A. Mehra, and V. V. Ranade. “Modeling and simulation of a fluidized bed gasifier”. In: *Asia-Pacific Journal of Chemical Engineering* 13.1 (2018), e2155.

[25] S. Gangwal. ”Gasification R&D Overview”. Tech. rep. Presented at the BETO Gasification Workshop, November 2022. U.S. Department of Energy, Bioenergy Technologies Office, 2022. URL: `https://www.energy.gov/sites/default/files/2022-12/beto-03-gasification-wkshp-nov-2022-gangwal.pdf`.

[26] IEA Bioenergy Task 33. ”Fuels from Biomass and Waste Gasification”. Accessed: 2025-07-29. 2023. URL: `https://task33.ieabioenergy.com/fuels-from-biomass-and-waste-gasification/`.

[27] D. R. Wagner. “Advancing Entrained-Flow Gasification of Waste Materials and Biomass for Hydrogen Production”. In: Presented at the 2024 FECM/NETL Spring R&D Project Review Meeting, 23–25 April 2024, Pittsburgh, PA. The University of Utah. Salt Lake City, UT, 2024.

[28] H. A. M. Knoef. “Handbook biomass gasification”. In: 2005. URL: `https://api.semanticscholar.org/CorpusID:133091728`.

[29] Y. Huang, Y. Wan, S. Liu, Y. Zhang, H. Ma, S. Zhang, and J. Zhou. “A Downdraft Fixed-Bed Biomass Gasification System with Integrated Products of Electricity, Heat, and Biochar: The Key Features and Initial Commercial Performance”. In: *Energies* 12.15 (Aug. 2019), p. 2979. ISSN: 1996-1073. DOI: `10.3390/en12152979`. URL: `http://dx.doi.org/10.3390/en12152979`.

[30] Leszek S. “Fluidization”. Master’s thesis, supervised by Marek Sciazko, AGH University of Science and Technology, Department of Energy and Fuels. January 2015. 2015.

[31] “Particle aggregation”. Wikipedia, retrieved 12 April 2025. Available online at `https://en.wikipedia.org/wiki/Particle_aggregation`. 2025.

[32] C. E. Agu, C. Pfeifer, M. Eikeland, L.A. Tokheim, and B. M. Moldestad. “Detailed one-dimensional model for steam-biomass gasification in a bubbling fluidized bed”. In: *Energy & fuels* 33.8 (2019), pp. 7385–7397.

[33] J.R.C. Rey, A. Longo, B. Rijo, C.M. Pedrero, L.A.C. Tarelho, P.S.D. Brito, and C. Nobre. “A review of cleaning technologies for biomass-derived syngas”. In: *Fuel* 377 (2024), p. 132776.

[34] D Toporov and R Abraham. “Gasification of low-rank coal in the High-Temperature Winkler (HTW) process”. In: ” Journal of the Southern African Institute of Mining and Metallurgy” 115.7 (2015), pp. 589–597.

[35] D. Kunii and O. Levenspiel. “Fluidization Engineering”. In: (1991).

[36] P. Basu. ”Combustion and gasification in fluidized beds”. CRC press, 2006.

[37] D. Cirillo, M Costa, M La Villetta, D Piazzullo, M. V. Prati, and V Rocco. “”Experimental validation of a one-dimensional steady model for downdraft biomass gasifiers””. In: *Proceedings of CHT-17 ICHMT International Symposium on Advances in Computational Heat Transfer*. Begel House Inc. 2017.

[38] C. Chen, J. Werther, S. Heinrich, H. Y. Qi, and E. U. Hartge. “CPFD simulation of circulating fluidized bed risers”. In: *Powder technology* 235 (2013), pp. 238–247.

[39] X. Ku, T. Li, and T. Løvås. “CFD–DEM simulation of biomass gasification with steam in a fluidized bed reactor”. In: *Chemical Engineering Science* 122 (2015), pp. 270–283.

[40] H. Liu, A. Elkamel, A. Lohi, and M. Biglari. “Computational fluid dynamics modeling of biomass gasification in circulating fluidized-bed reactor using the Eulerian–Eulerian approach”. In: *Industrial & engineering chemistry research* 52.51 (2013), pp. 18162–18174.

[41] D. Geldart. “Types of gas fluidization”. In: *Powder technology* 7.5 (1973), pp. 285–292.

[42] R. Cocco and J. W. Chew. “50 years of Geldart classification”. In: *Powder Technology* 428 (2023), p. 118861.

[43] M. Pell. ”Gas fluidization”. Elsevier, 2012.

[44] L. S. Fan and C. Zhu. “Principles of gas-solid flows”. In: *International Journal of Multiphase Flow* (1999).

[45] X. T. Li, J. R. Grace, C. J. Lim, A. P. Watkinson, H. P. Chen, and J. R. Kim. “Biomass gasification in a circulating fluidized bed”. In: *Biomass and bioenergy* 26.2 (2004), pp. 171–193.

[46] Aspen Technology, Inc. ”Aspen Plus”. Tech. rep. Accessed on 14 May 2025. Bedford, MA: AspenTech, 2025. URL: `https://www.aspentech.com/en/products/engineering/aspen-plus`.

[47] M. Puig-Gamero, D. T. Pio, L. AC Tarelho, P Sánchez, and L. Sanchez-Silva. “Simulation of biomass gasification in bubbling fluidized bed reactor using aspen plus®”. In: *Energy Conversion and Management* 235 (2021), p. 113981.

[48] Q. Miao, J. Zhu, S. Barghi, C. Wu, X. Yin, and Z. Zhou. “Model validation of a CFB biomass gasification model”. In: *Renewable energy* 63 (2014), pp. 317–323.

[49] E. D. Gordillo and A. Belghit. “A two phase model of high temperature steam-only gasification of biomass char in bubbling fluidized bed reactors using nuclear heat”. In: *International Journal of Hydrogen Energy* 36.1 (2011), pp. 374–381.

[50] B. Hejazi, J. R. Grace, X. Bi, and A. Mahecha-Botero. “Kinetic model of steam gasification of biomass in a dual fluidized bed reactor: Comparison with pilot-plant experimental results”. In: *Energy & Fuels* 31.11 (2017), pp. 12141–12155.

[51] A. Inayat, M. M. Ahmad, S. Yusup, and M. I. A. Mutalib. “Biomass steam gasification with in-situ CO2 capture for enriched hydrogen gas production: a reaction kinetics modelling approach”. In: *Energies* 3.8 (2010), pp. 1472–1484.

[52] Y. D. Kim, C. W. Yang, B. J. Kim, K. S. Kim, J. W. Lee, J. H. Moon, W. Yang, T. U. Yu, and U. Do Lee. “Air-blown gasification of woody biomass in a bubbling fluidized bed gasifier”. In: *Applied energy* 112 (2013), pp. 414–420.

[53] A. Pitkäoja, J. Ritvanen, S. Hafner, T. Hyppänen, and G. Scheffknecht. “Simulation of a sorbent enhanced gasification pilot reactor and validation of reactor model”. In: *Energy Conversion and Management* 204 (2020), p. 112318.

[54] S.P. Bhattacharya. “Gasification Performance of Australian Lignites in a Pressurized Fluidized Bed Gasifier Process Development Unit Under Air and Oxygen-enriched Air Blown Conditions”. In: *Process Safety and Environmental Protection* 84.6 (Nov. 2006), pp. 453–460. ISSN: 0957-5820. DOI: `10.1205/psep06007`. URL: `http://dx.doi.org/10.1205/psep06007`.

[55] T. K. Tulu, S. M. Atnaw, R. D. Bededa, D. G. Wakshume, and V. R. Ancha. “Kinetic modeling and optimization of biomass gasification in bubbling fluidized bed gasifier using response surface method”. In: *Int J Renew Energy Dev* 11.4 (2022).

[56] S. M. Beheshti, H. Ghassemi, and R Shahsavan-Markadeh. “Process simulation of biomass gasification in a bubbling fluidized bed reactor”. In: *Energy conversion and management* 94 (2015), pp. 345–352.

[57] Ö. Ç. Mutlu and T. Zeng. “Challenges and opportunities of modeling biomass gasification in Aspen Plus: A review”. In: *Chemical Engineering & Technology* 43.9 (2020), pp. 1674–1689.

[58] P. E. A. Debiagi, G. Gentile, M. Pelucchi, A. Frassoldati, A. Cuoci, T. Faravelli, and E. Ranzi. “Detailed kinetic mechanism of gas-phase reactions of volatiles released from biomass pyrolysis”. In: *Biomass and Bioenergy* 93 (2016), pp. 60–71.

[59] S. Hamel and W. Krumm. “Mathematical modelling and simulation of bubbling fluidised bed gasifiers”. In: *Powder technology* 120.1-2 (2001), pp. 105–112.

[60] A. Bhattarai, S. Kafle, M. Sakhakarmy, S. Moogi, and S. Adhikari. “Fluidized-bed gasification kinetics model development using genetic algorithm for biomass, coal, municipal plastic waste, and their blends”. In: *Energy* 313 (2024), p. 133989.

[61] A. Jess. “Mechanisms and kinetics of thermal reactions of aromatic hydrocarbons from pyrolysis of solid fuels”. In: *Fuel* 75.12 (1996), pp. 1441–1448.

[62] D. Zhu, Q. Wang, Z. Zhang, G. Xie, et al. “Kinetics simulation study of biomass partial gasification for producer gas and biochar co-production in the fluidized bed”. In: *Energy* (2025), p. 134919.

[63] R. Jaiswal, C.E. Agu, H.K. Nielsen, M.S. Eikeland, B.M. Emilie Moldestad, and R.K. Thapa. “Investigation of bubble properties in a bubbling fluidized-bed gasification reactor using a computational particle fluid dynamic model”. In: *Industrial & Engineering Chemistry Research* 62.21 (2023), pp. 8500–8514.

[64] W. M. Champion, C. D. Cooper, K. R. Mackie, and P. Cairney. “Development of a chemical kinetic model for a biosolids fluidized-bed gasifier and the effects of operating parameters on syngas quality”. In: *Journal of the Air & Waste Management Association* 64.2 (2014), pp. 160–174.

[65] A. Goyal, S. Pushpavanam, and R. K. Voolapalli. “Modeling and simulation of co-gasification of coal and petcoke in a bubbling fluidized bed coal gasifier”. In: *Fuel processing technology* 91.10 (2010), pp. 1296–1307.

[66] D. Tokmurzin, J. Y. Nam, T. R. Lee, S. J. Park, H. Nam, S. J. Yoon, T. Y. Mun, S. M. Yoon, J. H. Moon, J. G. Lee, et al. “High temperature flash pyrolysis characteristics of waste plastics (SRF) in a bubbling fluidized bed: Effect of temperature and pelletizing”. In: *Fuel* 326 (2022), p. 125022.

[67] P. Basu. ”Biomass gasification and pyrolysis: practical design and theory”. Academic press, 2010.

[68] F. Prashanth, R. N. Sarma, A. Jain, S. Segar, H. Choudhari, and R. Vinu. “Biomass fast pyrolysis kinetics using curie-point pyrolysis: Comparison with pyroprobe and thermogravimetric analysis”. In: *Journal of the Energy Institute* 115 (2024), p. 101699.

[69] C. Dupont, J. M. Commandre, P. Gauthier, G. Boissonnet, S. Salvador, and D. Schweich. “Biomass pyrolysis experiments in an analytical entrained flow reactor between 1073 K and 1273 K”. In: *Fuel* 87.7 (2008), pp. 1155–1164.

[70] A. Aghaalikhani, J. C. Schmid, D. Borello, J. Fuchs, F. Benedikt, H. Hofbauer, F. Rispoli, U. B. Henriksen, Z. Sárossy, and L. Cedola. “Detailed modelling of biomass steam gasification in a dual fluidized bed gasifier with temperature variation”. In: *Renewable Energy* 143 (2019), pp. 703–718.

[71] K. Bizon. “Application of pseudohomogeneous and heterogeneous models in assessing the behavior of a fluidized-bed catalytic reactor”. In: *Energies* 14.1 (2021), p. 208.

[72] Barry J. Azzopardi. ”SAUTER MEAN DIAMETER”. Accessed: June 9, 2025. 2011. URL: `https://www.thermopedia.com/content/1108/`.

[73] Y. Yao, A. Panahi, M. Schiemann, and Y. A. Levendis. “Determination of size and porosity of chars during combustion of biomass particles”. In: *Combustion and Flame* 242 (2022), p. 112182. ISSN: 0010-2180. DOI: `https://doi.org/10.1016/j.combustflame.2022.112182`. URL: `https://www.sciencedirect.com/science/article/pii/S0010218022001973`.

[74] D. Tarlinski, E. Freisewinkel, T. Eisenbach, R. Span, M. Schiemann, and V. Scherer. “Combustion of single walnut shell particles in a laminar flow reactor under oxy-fuel conditions: Optical measurements and particle sampling”. In: *Fuel* 369 (2024), p. 131613.

[75] R. Wu and L. L Baxter. “Dynamic biomass char porosity during gasification: Model compared with data”. In: *Energy* 267 (2023), p. 126603.

[76] M. B. Nikoo. and M. Nader. “Simulation of biomass gasification in fluidized bed reactor using ASPEN PLUS”. In: *Biomass and Bioenergy* 32.12 (2008), pp. 1245–1254. ISSN: 0961-9534. DOI: `https://doi.org/10.1016/j.biombioe.2008.02.020`. URL: `https://www.sciencedirect.com/science/article/pii/S0961953408000688`.

[77] D. Neves, H. Thunman, A. Matos, L. Tarelho, and A. Gómez-Barea. “Characterization and prediction of biomass pyrolysis products”. In: *Progress in energy and combustion Science* 37.5 (2011), pp. 611–630.

[78] Cantera Developers. ”Cantera Documentation: Reaction Rates”. Accessed: March 10, 2025. 2024. URL: `https://cantera.org/3.1/reference/kinetics/reaction-rates.html#sec-three-body-reaction`.

[79] I.A. Gibson, C.J. Slim, Y. Zheng, S. A. Scott, J. F. Davidson, and A. N. Hayhurst. “An examination of Wen and Yu’s formula for predicting the onset of fluidisation”. In: *Chemical Engineering Research and Design* 135 (July 2018), pp. 103–111. ISSN: 0263-8762. DOI: `10.1016/j.cherd.2018.05.009`. URL: `http://dx.doi.org/10.1016/j.cherd.2018.05.009`.

[80] D. Wang and L.-S. Fan. “Particle characterization and behavior relevant to fluidized bed combustion and gasification systems”. In: *Fluidized Bed Technologies for Near-Zero Emission Combustion and Gasification*. Ed. by Fabrizio Scala. Woodhead Publishing Series in Energy. Woodhead Publishing, 2013, pp. 42–76. ISBN: 978-0-85709-541-1. DOI: `https://doi.org/10.1533/9780857098801.1.42`. URL: `https://www.sciencedirect.com/science/article/pii/B9780857095411500029`.

[81] J. Riaza, P. E. Mason, J. M Jones, A. Williams, J. Gibbins, and H. Chalmers. “Shape and size transformations of biomass particles during combustion”. In: *Fuel* 261 (2020), p. 116334.

[82] Q. Guo, X. Chen, and H. Liu. “Experimental research on shape and size distribution of biomass particle”. In: *Fuel* 94 (2012), pp. 551–555.

[83] A. Luckos and A. Koekemoer. “On the sphericity of coal and char particles”. In: *South African Journal of Chemical Engineering* 19.3 (2014), pp. 62–71.

[84] K. Hilligardt and J. Werther. “Local bubble gas hold-up and expansion of gas/solid fluidized beds”. In: *Ger. Chem. Eng.(Engl. Transl.);(Germany, Federal Republic of)* 9.4 (1986).

[85] J. F. Richardson and W. N. Zaki. “Sedimentation and fluidisation: Part I”. In: *Chemical Engineering Research and Design* 75 (1997), S82–S100.

[86] C. E. Agu, C. Pfeifer, M. Eikeland, L. A. Tokheim, and B. M. E Moldestad. “Models for predicting average bubble diameter and volumetric bubble flux in deep fluidized beds”. In: *Industrial & Engineering Chemistry Research* 57.7 (2018), pp. 2658–2669.

[87] Arena U. “Process and technological aspects of municipal solid waste gasification. A review”. In: *Waste Management* 32.4 (2012). Solid Waste Gasification, pp. 625–639. ISSN: 0956-053X. DOI: `https://doi.org/10.1016/j.wasman.2011.09.025`. URL: `https://www.sciencedirect.com/science/article/pii/S0956053X11004314`.

[88] A. Haider and O. Levenspiel. “Drag coefficient and terminal velocity of spherical and nonspherical particles”. In: *Powder Technology* 58.1 (1989), pp. 63–70. ISSN: 0032-5910. DOI: `https://doi.org/10.1016/0032-5910(89)80008-7`. URL: `https://www.sciencedirect.com/science/article/pii/0032591089800087`.

[89] A. V. Narayana and M. V. Leela. “Modeling of Freeboard Fluidized Bed Gasifier Integrated to Bubbling Dense Bed”. In: *Research Journal of Pharmaceutical, Biological and Chemical Sciences* 4.4 (2013), pp. 1033–1044. URL: `https://www.rjpbcs.com/pdf/2013_4(4)/%5B108%5D.pdf`.

[90] TU Darmstadt – Energy Systems and Technology. *Energy Systems and Technology - TU Darmstadt*. Accessed: 2025-06-30. 2025. URL: `https://www.est.tu-darmstadt.de/est_est/index.en.jsp`.

[91] C. Heinze, J. May, E. Langner, J. Ströhle, and B. Epple. “High Temperature Winkler gasification of Rhenish lignite in an optimized 500 kWth pilot plant”. In: *Fuel* 333 (2023), p. 126289.

[92] F. Schlupp, J. Page, C. Djelal, and L. Libessart. “Use of Biomass Bottom Ash as an Alternative Solution to Natural Aggregates in Concrete Applications: A Review”. In: *Materials* 17.18 (2024), p. 4504.

[93] A.E. Ghaly and K.N. MacDonald. “Mixing patterns and residence time determination in a bubbling fluidized bed system”. In: *American Journal of Engineering and Applied Sciences* 5.2 (2012), pp. 170–183.

[94] R. B. Bates, A. F. Ghoniem, W. S. Jablonski, D. L. Carpenter, C. Altantzis, A. Garg, J. L Barton, R. Chen, and R. P Field. “Steam-air blown bubbling fluidized bed biomass gasification (BFBBG): Multi-scale models and experimental validation”. In: *AIChE Journal* 63.5 (2017), pp. 1543–1565.

[95] Wikipedia contributors. *Péclet number*. [Online; accessed 24-June-2025]. 2025. URL: `https://en.wikipedia.org/w/index.php?title=P%C3%A9clet_number&oldid=123456789`.

[96] C.E.J Van Lare, H.W. Piepers, J.N. Schoonderbeek, and D Thoenes. “Investigation on bubble characteristics in a gas fluidized bed”. In: *Chemical Engineering Science* 52.5 (1997), pp. 829–841.

[97] M. S. Zulkefli. “Hydrodynamic Behavior of Geldart particles type B and D in semi circular fluidized bed”. In: (2012).

[98] Rossella Girimonte and Brunello Formisani. “The Variation of the Bubble Phase Properties of a FCC Fluidized Bed at High Temperature”. In: *10th International Conference on Circulating Fluidized Beds and Fluidization Technology (CFB-10)*. Ed. by T. Knowlton. ECI Symposium Series. Engineering Conferences International. 2013. URL: `http://dc.engconfintl.org/cfb10/80`.

[99] C. E. Agu, L. A. Tokheim, M. Eikeland, and B. M. E. Moldestad. “Improved models for predicting bubble velocity, bubble frequency and bed expansion in a bubbling fluidized bed”. In: *Chemical Engineering Research and Design* 141 (2019), pp. 361–371.

[100] B. Das and A. Datta. “Modeling of hydrodynamics in a bubbling fluidized-bed gasifier and evaluation of the inter-phase gas exchange rate under different operating conditions”. In: *Particuology* 25 (2016), pp. 151–158.

[101] J. Kim, H. Oh, S. Lee, and Y.S. Yoon. “Advanced one-dimensional entrained-flow gasifier model considering melting phenomenon of ash”. In: *Energies* 11.4 (2018), p. 1015.

[102] A.G. Konstandopoulos, C. Pagkoura, and S. Lorentzou. “20 - Solar fuels and industrial solar chemistry”. In: *Concentrating Solar Power Technology*. Ed. by Keith Lovegrove and Wes Stein. Woodhead Publishing Series in Energy. Woodhead Publishing, 2012, pp. 620–661. ISBN: 978-1-84569-769-3. DOI: `https://doi.org/10.1533/9780857096173.3.620`. URL: `https://www.sciencedirect.com/science/article/pii/B9781845697693500200`.

[103] S. W. Park, J. S. Lee, W. S. Yang, M. T. Alam, and Y. C. Seo. “A comparative study of the gasification of solid refuse fuel in downdraft fixed bed and bubbling fluidized bed reactors”. In: *Waste and Biomass Valorization* 11 (2020), pp. 2345–2356.

[104] Cantera Developers. *Cantera YAML Input Format – Reactions*. `https://cantera.org/3.1/yaml/reactions.html`. Accessed June 29, 2025. 2025.

[105] Aspen Technology. *Reaction in Fluidized Beds: Guide to the Fluidized Bed Reactor Demo*. Aspen Plus Documentation. Aspen Technology. Bedford, MA, 2013.

[106] R. V. Kappagantula, G. D. Ingram, and H. B Vuthaluru. “Application of Aspen Plus fluidized bed reactor model for chemical Looping of synthesis gas”. In: *Fuel* 324 (2022), p. 124698.

[107] NETL. *MFIX Multiphase Flow with Interphase eXchanges*. `https://mfix.netl.doe.gov/products/mfix/`. Accessed June 29, 2025. 2025.

[108] Cantera Developers. ”Cantera Documentation: Transport Models”. Accessed: 2025-04-24. URL: `https://cantera.org/dev/python/transport.html`.

[109] C. Michelbach and A. Tomlin. “An experimental and kinetic modeling study of the ignition delay and heat release characteristics of a five component gasoline surrogate and its blends with iso-butanol within a rapid compression machine”. In: *International Journal of Chemical Kinetics* 53.6 (2021), pp. 787–808.

[110] G. P. Smith and D. M. Golden and M. Frenklach and N. W. Moriarty and B. Eiteneer and M. Goldenberg and C. T. Bowman and R. K. Hanson and W. C. Gardiner Jr. and V. V. Lissianski and Z. Qin. “GRI-Mech 3.0”. `http://www.me.berkeley.edu/gri_mech/`. Accessed via Cantera mechanism file gri30_highT.yaml. 1999.

[111] CRECK Modeling Group. ”TOT-H2: Detailed Kinetic Mechanism for Hydrogen Combustion”. 2019. URL: `https://www.creckmodeling.polimi.it/menu-kinetics/menu-kinetics-detailed-mechanisms/107-category-kinetic-mechanisms/402-mechanisms-1911-tot-ht/`.

[112] ANSYS. ”CHEMKIN Software Suite”. 2023. URL: `https://www.ansys.com/products/fluids/ansys-chemkin-pro`.

[113] California Institute of Technology Explosion Dynamics Laboratory. ”CHEMKIN File Formats”. 2023. URL: `https://shepherd.caltech.edu/EDL/PublicResources/sdt/formats/chemkin.html`.

[114] A. Miyoshi. ”Chemkin-II Input”. Accessed: February 25, 2025. URL: `https://akrmys.com/public/chemkin/CKm_inp.html.en`.

[115] J. M. Powers. ”Notes on Transport Phenomena”. Accessed: February 25, 2025. URL: `https://www3.nd.edu/~powers/ame.60636/transport.pdf`.

A

Cantera YAML Mechanism Files

In Figure A.1, a screenshot from the emulsion phase Cantera YAML mechanism can be seen, illustrating how individual species, such as H_2 and O_2 are defined in the Cantera environment.

```yaml
phases:
- name: emulsion
  thermo: ideal-gas
  elements: [O, H, C, N]
  species: [H2, CO, CO2, C10H8, H2O, C6H6, C6H6O, O2, CH4, C2H4, C, N2]
  kinetics: gas
  reactions: all
  transport: mixture-averaged
  state:
    T: 1073.15
    P: 1.01325e+05

species:
- name: H2
  composition: {H: 2}
  thermo:
    model: NASA7
    temperature-ranges: [200.0, 1000.0, 6000.0]
    data:
    - [2.34433112, 7.98052075e-03, -1.9478151e-05, 2.01572094e-08, -7.37611761e-12,
      -917.935173, 0.683010238]
    - [2.93286579, 8.26607967e-04, -1.46402335e-07, 1.54100359e-11, -6.88804432e-16,
      -813.065597, -1.02432887]
  transport:
    model: gas
    geometry: linear
    diameter: 2.92
    well-depth: 38.0
    polarizability: 0.79
    rotational-relaxation: 280.0
  note: TPIS78

- name: O2
  composition: {O: 2}
  thermo:
    model: NASA7
```

Figure A.1: Screenshot from the Cantera emulsion phase mechanism.

At the top, the thermodynamic model for the mechanism is defined as well as the elements considered in the mechanism, the total amount of species involved, the general transport model and the temperature and pressure conditions. For all the mechanisms in Cantera, the approximation of the gas as ideal gas was used, in order to calculate parameters, such as the density and the dynamic viscosity of each. The ”kinetics : gas” field shows that only gas-phase reactions are considered in this mechanism, while the ”reactions: all” field indicates that all the reactions specified in this mechanism file are actually taking place. In addition, the ”transport” model is defined as ”mixture-averaged”, which means that Cantera calculates transport properties of the phase based on average values across the mixture of gases [108].

As can be seen, each species begins with the keyword ”name”, followed by its molecular composition. Afterwards, the ”thermo” section defines the thermodynamic model that is being used to calculate the thermodynamic properties of the species as a function of temperature. More specifically, they are used to determine the specific heat capacity, entropy and enthalpy of the species, which are essential for the determination of equilibrium states, reaction kinetics, their transport properties and their changing properties during a process [109]. In this case, the model used is the NASA7 [110], which refers to a set of seven temperature-dependent polynomial coefficients, applied over three temperature ranges, shown in the ”temperature-ranges” field, as specified as [200.0, 1000.0, 6000.0] in the case of H_2. The NASA7 coefficients and the temperature range were derived from the CRECK file for the species C_6H_6O, C_6H_6 and $C_{10}H_8$ [111] and from the already-existing ”gri30-highT.yaml” file from Cantera’s documentation for the rest of the compounds, and they were input in the YAML mechanisms. The files in CRECK are in CHEMKIN format [112], which is commonly used for defining chemical kinetics mechanisms. CHEMKIN, which is now a part of ANSYS, is a software tool used for modeling complex chemical kinetics and simulating various reacting systems. In CHEMKIN format, the first 7 values of coefficients for each species are for the upper temperature interval [113, 114], while in the YAML file the first 7 thermodynamics data are for the low temperature interval, so the necessary reordering needed to be made. After the ”thermo” section, there is the ”transport” section, specifying the transport properties for each species. These include the Lennard-Jones parameters — mainly the molecular geometry, collision diameter (Å), and potential well depth (K) — which are used by Cantera to calculate the viscosity, thermal conductivity, and diffusion coefficients of the different mechanisms. The values for these properties for each species were derived from the CRECK file (which was interpreted with the help of [115]) and were inserted into the YAML file (see Figure A.1).

This structure was then repeated for each gaseous species considered in the emulsion phase (see the row ”species” in the ”phases” section at the top of the Figure A.1), as well as in the other mechanisms (bubble and freeboard).

B

Model Algorithm

The overall simulation process is outlined in detail below:

1. **Step 1: Initialization**
    - *Step 1.1*: Import libraries, load the required Python packages, such as Cantera, NumPy, SciPy, SymPy, and matplotlib.
    - *Step 1.2*: Load the Cantera mechanisms (the YAML files) representing the emulsion phase, the bubble phase and the freeboard.
    - *Step 1.3*: Define the reactor geometry, by specifying its height and its diameter(s). Divide the fluidized bed and the freeboard into N and M horizontal cells respectively (the decision behind the number of the discretized cells will be explained further in Section 4.2). Calculate the height of the midpoint of each cell (y and y_{FB}) as well as the cell heights (dn and dm).
    - *Step 1.4*: Define the operating conditions, the gasification and pyrolysis temperature, the operating pressure P, the gas constant R, the gravitational constant g as well as the number of nozzle openings.
    - *Step 1.5*: Define the fuel and bed properties, the feedstock inflow rate, the particle density ρ_p and particle size of the bed material d_p as well as the superficial gas velocity u_0.
    - *Step 1.6*: Based on the given geometry of the gasifier that this model is based on, define the nozzle heights and the species entering through each one (gasification , fluidization and seal gas agents (O_2, H_2O or CO_2)).
2. **Step 2: Pyrolysis Modeling**
    - *Step 2.1*: Depending on whether the feedstock is biomass or SRF, follow the respective pyrolysis model. For biogenic feedstock, form symbolic expressions for the elemental balances for elements C, H, O, empirical correlations for the calculation of the mass yield of char, CH_4, CO and H_2, and for the energy balance of the pyrolysis gas. By using the proximate and ultimate analysis of the feedstock and the pyrolysis temperature, the Equations C.2 - C.20 are solved through a non-linear solver (such as ”least squares”) and the mass fractions of each species for the pyrolysis product are determined. This constitutes the ”pyrolysis solver” function. For waste-derived feedstock, based on the pyrolysis temperature, calculate the mass yields of the pyrolysis products, through solving Equations 3.1 - 3.9.
    - *Step 2.2*: Initialize the mass fractions of the emulsion phase for cell 0 based on the results of the pyrolysis model.
    - *Step 2.3*: Initialize the mass fractions of the bubble phase for cell 0, based on the CO_2 mass inflow entering through the nozzle at the bottom of the reactor and acting as a seal gas. The mass flow of carbon dioxide is known based on the TU Darmstadt’s experiments, that this model is based on for validation.

3. **Step 3: Nozzle Profile**
    - *Step 3.1*: Define the mass flow distribution percentages of each species (which are user-defined and subject to a sensitivity analysis conducted later), based on the total mass flows which are already known from the experimental conditions in TU Darmstadt.
    - *Step 3.2*: Assign these mass flows to the reactor grid. Based on the height where each nozzle is located, assign the mass flow entering through the nozzle to the nearest cell of the reactor's computational grid. Define the arrays $m_{in,b}$ and $m_{in,FB}$ for the bed and the freeboard respectively, that contain these nozzle injection profiles.
4. **Step 4: Initial Bed Hydrodynamics Calculations**
    - *Step 4.1*: Calculate the value of ϵ_{mf} through Eq. 3.11, solved via the "fsolve" Python solver.
5. **Step 5: Fluidized Bed Mass Balance ODE Solution**
    - *Step 5.1:* Define the residence time that the species are present in the bed, and by dividing with the bed cell discretization, define the residence time in one cell.
    - *Step 5.2:* Formulate the loop over all cells of the bed. Set up the convergence criteria for all cells (such as maximum number of iterations and system's tolerance). Initialize an array called "emulsion Y prev" and "bubble Y prev" with the current mass fractions of the Cantera emulsion and bubble mechanisms respectively.
    - *Step 5.3:* Begin the inner iteration loop. For cell 0 and for the first iteration in the "max inner iterations" range, set the emulsion and bubble state for this cell based on the gasification temperature, the operating pressure and the "emulsion Y prev" and the "bubble Y prev" arrays. Both the "emulsion Y prev" and "bubble Y prev" are currently initialized with the outputs of "Step 2: Pyrolysis Modeling".
    - *Step 5.4:* Store the current values of the emulsion and bubble density, as well as the mass and mole fractions for these two phases in arrays.
    - *Step 5.5:* Calculate the fluidization properties. More specifically, calculate the minimum fluidization velocity u_{mf} (through a function based on the Equation 3.12), the emulsion gas velocity u_d (Equation 3.16), the emulsion porosity or voidage ϵ_d (Equation 3.17), the bubble speed u_b (Equation 3.23), the bubble rise velocity $u_{b,i}$ (Equation 3.24), the bubble volume fraction ϵ_b (Equation 3.25) and the Archimedes number Ar (Equation 3.13). Save the results in arrays.
    - *Step 5.6:* Based on the fluidization properties calculated in Step 5.5, compute the bubble diameter (Equation 3.26) and store the results in arrays.
    - *Step 5.7:* Calculate the mass exchange area over all bubbles in each bed cell (A_{db}) by using the "calc Adb" function based on Equation 3.49. Calculate the mass transfer coefficient (K_{db}) between the bubble and suspension phase by using the "calc Kdb" function, which is based on Equation 3.48. Compute the volume of the current cell (V_{cell}) by using the function "V cell", which is based on (Equation 3.63). Finally, for current cell 0 consider the actual mass inflow values.
    - *Step 5.8:* Define the initial mass for each species in the emulsion and the bubble phase. For cell 0, the initial mass of each species in the emulsion phase is defined by multiplying the feedstock mass inflow rate with the cell residence time and the pyrolysis yields (calculated from Step 2.1 of the Algorithm). For the bubble phase, the initial mass values of the species, are defined through multiplying the CO_2 flow rate entering at the bottom of the reactor with the cell residence time. For cells above n=0, the initial mass values were derived from the solution of the ODEs for the previous cell for each respective species.
    - *Step 5.9:* Solve the three different bed mass balance ODEs using the "solve ivp" Python command, with stiff solver "LSODA".
        - In the ODE function for the emulsion phase mass balance (Equation 3.43) calculate the interphase mass exchange term (Equation 3.46), the reaction rate term and the convective inflow (Equation 3.44) and outflow term (Equation 3.44) for each cell and for

  each species (apart from C). Calculate the rate of mass change for each species in the emulsion phase and store it in the ”dMd dt values” array. Explicitly enforce that the ”dMd dt values” value for C is zero, to ensure that the mass balance of carbon is handled through a separate equation.
  - In the ODE function for the bubble phase mass balance (Equation 3.43), calculate the interphase mass exchange term (Equation 3.47), the reaction rate term, the incoming flow term $m_{in,b}$ (which has been defined earlier in the Step 3.2 of the algorithm) and the convective inflow (Equation 3.45) and outflow term (Equation 3.45) for each cell and for each species (apart from C). Calculate the rate of mass change for each species in the bubble phase and store it in the ”dMb dt values” array.
  - In the ODE for the mass balance of C in the emulsion phase (Equation 3.50), calculate the reaction rate term, the convective inflow and outflow (Equation 3.44), the wake inflow and outflow (Equation 3.51), as well as the drift inflow and outflow term (Equation 3.52). Calculate the rate of mass change for C and store it in the ”dM C dt values” array.

  Integrate the ODEs over a time span of ”t span” (equal to the cell residence time) and using the initial masses from Step 5.8 of the Algorithm. Access the final values of the ODEs solution and store them.

- *Step 5.10:* Clip the negative values from the solution of the ODEs and update the mass arrays (”M d final” and ”M b final”).
- *Step 5.11:* Compute the sum of the masses of all species for the current cell in both the emulsion and the bubble phase, calculate the respective mass fractions by dividing with the mass sum. Use the solution from the previous iteration if the new values are nonphysical or if the total mass is near zero. If necessary, clip and re-normalize the mass fractions.
- *Step 5.12:* Calculate the maximum difference between the old array of the species' mass fractions and the new one, that got derived from the ODEs solution. If the maximum difference is below the tolerance threshold, mark this cell as converged and break the inner loop, moving on to the next cell. If the maximum difference is above the tolerance, use an under-relaxation factor to update the ”emulsion Y prev” and the ”bubble Y prev” arrays. The relaxation factor aims at decreasing the rush of numerical instability, by gradually updating the mass fraction instead of jumping to the new value immediately.
  - *Step 5.12.1:* For the next iteration, update the emulsion and bubble phases with the under-relaxed ”emulsion Y prev” and the ”bubble Y prev” arrays. Repeat Steps 5.4 until 5.12.
  - *Step 5.12.2:* If convergence is reached before the iteration counter surpasses the ”max inner iterations”, then mark the cell as converged. If convergence is still not reached when the iteration counter reaches the ”max inner iterations”, then mark the cell as non-converged, and the last available ”emulsion Y prev” and ”bubble Y prev” are used. Move on to the next cell.
- *Step 5.13:* For the next cell, repeat Steps 5.4 until 5.12, until reaching cell number N.

6. **Step 6: Initial Freeboard Hydrodynamics Calculations**
   - *Step 6.1:* Initialize the conditions of the freeboard Cantera mechanism, based on the freeboard temperature and the emulsion and bubble phase characteristics at the end of the bed region.
   - *Step 6.2:* Calculate the initial particle starting speed $u_{p,0}$, based on Equation 3.27, and solve the equation of motion for the ghost bubbles u_{gb}, through the Equations **??**, **??** and **??**.
   - *Step 6.3:* Calculate the mass of entrained solids into the freeboard (through Equation 3.57). Afterwards, compute the volume that the entrained solids occupy in the freeboard (Equation 3.40), based on which you can calculate the voidage in the freeboard ϵ_{PGZ} (Equation 3.38) and then the gas velocity in the freeboard u_g (Equation 3.37).
7. **Step 7: Freeboard Mass Balance ODE Solution**

- *Step 7.1:* Define the residence time that the species are present in the freeboard, and by dividing with the freeboard cell discretization, define the residence time in one cell.
- *Step 7.2:* Formulate the loop over all cells of the freeboard. Set up the convergence criteria for all cells. Initialize an array called ”freeboard Y prev” with the current mass fractions of the freeboard Cantera mechanism.
- *Step 7.3:* Begin the inner iteration loop. For cell 0 and for the first iteration in the ”max iterations” range, set the freeboard state for this cell based on the freeboard temperature, the pressure and the ”freeboard Y prev” array. Note that the freeboard mechanism is initialized at that point with the results of the emulsion and bubble phase mechanism from the top bed cell.
- *Step 7.4:* Store the current values of the freeboard density, mass and mole fractions in arrays.
- *Step 7.5:* Solve the ODE describing the motion of the entrained particles in the freeboard (Equation 3.28). The ODE is based on the Reynolds number Re (Equation 3.36) and the drag coefficient c_w correlation (Equation 3.35), as well as on the relative particle velocity u_r (3.34).
- *Step 7.6:* Define the initial mass for each species in the freeboard phase. For cell 0, the initial mass, as previously stated, is equal to the mass of each individual species exiting the bed (from both the emulsion and the bubble phase). For the cells above m=0, the initial mass values of each species were derived from the solution of the freeboard mass balance ODE for the previous cell for each respective species.
- *Step 7.7:* Solve the two different freeboard mass balance ODEs using the ”solve ivp” Python command, with stiff solver ”LSODA”.
  - In the ODE function for the gaseous species of the freeboard phase (Equation 3.53), calculate the reaction rate term, the incoming flow term $\dot{M}^{m}_{\mathrm{in,j}}$, and the convective mass inflow (Equation 3.54) and outflow term (Equation 3.55) for each cell and for each species (apart from C). Calculate the rate of mass change for each species and store it in the ”dM gas dt freeboard values” array. Explicitly enforce that the ”dM gas dt freeboard values” value for carbon species is zero.
  - In the ODE for the mass balance of C in the freeboard phase (Equation 3.58), calculate the reaction rate term and the convective mass inflow (Equation 3.59) and outflow term (Equation 3.60). Calculate the rate of mass change for carbon and store it in the ”dM C dt freeboard values” array.

  Integrate the ODEs over a time span of ”t span” (equal to the residence time in a cell in the freeboard) and using the initial masses from Step 7.6. Access the results of the ODEs and store them.
- *Step 7.8:* Clip the ODE results to prevent negative values, and update the mass array (M FB final).
- *Step 7.9:* Sum up the final masses of all species for the current cell and calculate the mass fraction for each individual species, by dividing with the mass sum. Use previous solution if the new values are nonphysical or if the total mass is near zero. If necessary, clip and re-normalize the mass fractions.
- *Step 7.10:* Calculate the maximum difference between the old array of the species’ mass fractions and the new one, that got derived from the ODEs solution. If the maximum difference is below the tolerance threshold, mark this cell as converged and break the inner loop, moving on to the next cell. If the maximum difference is above the tolerance, use an under-relaxation factor to update the ”freeboard Y prev” array.
  - *Step 7.10.1:* For the next iteration, update the freeboard phase with the under-relaxed ”freeboard Y prev” array. Repeat Steps 7.4 until 7.10.
  - *Step 7.10.2:* If convergence is reached before the iteration counter surpasses the ”max inner iterations”, then mark the cell as converged. If convergence is still not reached

    when the iteration counter reaches the ”max inner iterations”, then mark the cell as non-converged, and the last available ”freeboard Y prev” is used. Move on to the next cell.

  - *Step 7.11:* For the next cell, repeat Steps 7.4 until 7.10, until reaching cell number M.

8. **Step 8: Processing the Results**
   After the loop over all the cells of the gasifier has been completed, the results are stored and used to analyze gas composition, species profiles, and overall performance of the gasifier.

C

Pyrolysis of biomass feedstock

The pyrolysis of biomass, despite various compositions of biomass and the different experimental conditions and reactor types, still shows some common trends for the products released, which can be explained by the fact that most biomass fuels have a relatively similar elemental composition [77]. In this thesis project, the model developed by Neves et al. (2011) [77] was chosen to be followed for the determination of the pyrolysis products of biogenic feedstock. The pyrolysis products that were considered were the char, tar and the volatiles CO, CO_2, CH_4, H_2O, H_2, and longer hydrocarbons CxHy, which were eventually considered to be approximated by ethylene C_2H_4. Additionally, tar was assumed to be composed only of C, H and O, while char solely of carbon.

The inputs to the biomass pyrolysis model are the ultimate analysis in carbon, hydrogen and oxygen (denoted as $Y_{C,F}$, $Y_{H,F}$ and $Y_{O,F}$). The ultimate analysis is expressed on a dry, ash-free basis (daf), meaning that both moisture and ash had been removed from the feedstock sample prior to measuring its contents in carbon (C), hydrogen (H) and oxygen (O). In addition to the ultimate analysis, other inputs to the model are the proximate analysis (moisture and ash content (%)) of the biomass and the pyrolysis temperature (T), while the outputs of the model are the mass fractions of the components in the pyrolysis product. More specifically, the inputs and outputs of the biomass pyrolysis model are shown in the Table C.1. The subscript ”F” in the following terms refers to dry, ash-free fuel.

Inputs to the pyrolysis model	Outputs of the pyrolysis model
$Y_{C,F}$	$Y_{CO,F}$
$Y_{O,F}$	$Y_{CO_2,F}$
$Y_{H,F}$	$Y_{CH_4,F}$
T	$Y_{H_2,F}$
Fuel Moisture	$Y_{H_2O,F}$
Fuel Ash	$Y_{tar,F}$
	$Y_{ch,F}$
	$Y_{C_xH_y,F}$

Table C.1: Inputs and outputs of the biomass pyrolysis model.

As previously mentioned in the assumptions list, the outputs of the pyrolysis model are used as the inputs to the gasification model, and therefore the aforementioned Cantera mechanisms (see Section 3.3.1).

Equation C.1 describes the decomposition of biomass fuel into its pyrolysis products.

$$\begin{aligned} \textit{Biomass} \rightarrow\ & Y_{CO,F} \cdot \mathrm{CO} + Y_{CO_2,F} \cdot \mathrm{CO_2} + Y_{H_2O,F} \cdot \mathrm{H_2O} + Y_{H_2,F} \cdot \mathrm{H_2} \\ & + Y_{CH_4,F} \cdot \mathrm{CH_4} + Y_{C_2H_4,F} \cdot \mathrm{C_2H_4} + Y_{tar,F} \cdot \mathrm{Tar} + Y_{ch,F} \cdot \mathrm{Char} \end{aligned} \tag{C.1}$$

Equations C.2, C.3 and C.4 are empirical relations derived in [77] that express the content of tar in carbon, oxygen and hydrogen as a function of the temperature and the respective content of carbon, oxygen and hydrogen in the water, ash-free fuel.

$$\frac{Y_{\text{C,tar}}}{Y_{\text{C},F}} = 1.05 + 1.9 \times 10^{-4} \cdot T, \quad R^2 = 0.07 \tag{C.2}$$

$$\frac{Y_{\text{O,tar}}}{Y_{\text{O},F}} = 0.92 - 2.2 \times 10^{-4} \cdot T, \quad R^2 = 0.07 \tag{C.3}$$

$$\frac{Y_{\text{H,tar}}}{Y_{\text{H},F}} = 0.93 + 3.8 \times 10^{-4} \cdot T, \quad R^2 = 0.06 \tag{C.4}$$

Since it has been assumed that tar consists solely of carbon, oxygen and hydrogen, in order to guarantee that the mass fractions sum to unity and avoid numerical inconsistencies in the model, the results from the Equation C.2 - Equation C.4 were renormalized.

Similarly to tars, Equations C.5, C.6 and C.7 give the $\mathrm{C, H, O}$ composition of the char based on the pyrolysis temperature (which must be inside the range of 250-1000 ° C). Despite the assumption that char consists only of carbon in the gasification reactions, in order to be in accordance with the empirical model by Neves et al. and obtain the most accurate pyrolysis yields, the following Equations were adopted for the pyrolysis model. Again, the results of the following Equations, were renormalized to ensure they sum to unity.

$$Y_{\text{C,ch}} = 0.93 - 0.92 \cdot \exp\left(-0.42 \times 10^{-2} \cdot T\right), \quad R^2 = 0.65 \tag{C.5}$$

$$Y_{\text{H,ch}} = -0.41 \times 10^{-2} + 0.10 \cdot \exp\left(-0.24 \times 10^{-2} \cdot T\right), \quad R^2 = 0.75 \tag{C.6}$$

$$Y_{\text{O,ch}} = 0.07 + 0.85 \cdot \exp\left(-0.48 \times 10^{-2} \cdot T\right), \quad R^2 = 0.56 \tag{C.7}$$

Based on the model proposed by Neves et al. (2011), the equations that were employed for the calculation of the product yields, were the elemental balances for C, H, O (Eq. C.8, C.9 and C.10 respectively), the empirical Equations (C.11), (C.12), (C.13), (C.14), (C.16) and (C.20) which were derived by the authors (further detailed below). This approach guarantees that the overall elemental balances for carbon, hydrogen and oxygen are satisfied by design, ensuring thermodynamic consistency between the incoming fuel's composition and the pyrolysis product yields.

$$\begin{aligned} Y_{\text{C},F} - Y_{\text{C,char}} \cdot Y_{\text{char},F} = Y_{\text{C,tar}} \cdot Y_{\text{tar},F} + Y_{\text{C},C_2H_4} \cdot Y_{C_2H_4,F} \\ + Y_{\text{C},CH_4} \cdot Y_{\text{CH}_4,F} + Y_{\text{C},CO} \cdot Y_{\text{CO},F} + Y_{\text{C},CO_2} \cdot Y_{\text{CO}_2,F} \end{aligned} \tag{C.8}$$

$$\begin{aligned} Y_{\text{O},F} - Y_{\text{O,char}} \cdot Y_{\text{char},F} = Y_{\text{O,tar}} \cdot Y_{\text{tar},F} \\ + Y_{\text{O},CO} \cdot Y_{\text{CO},F} + Y_{\text{O},CO_2} \cdot Y_{\text{CO}_2,F} + Y_{\text{O},H_2O} \cdot Y_{\text{H}_2O,F} \end{aligned} \tag{C.9}$$

$$\begin{aligned} Y_{\text{H},F} - Y_{\text{H,char}} \cdot Y_{\text{char},F} = Y_{\text{H,tar}} \cdot Y_{\text{tar},F} + Y_{\text{H},C_2H_4} \cdot Y_{C_2H_4,F} \\ + Y_{\text{H},CH_4} \cdot Y_{\text{CH}_4,F} + Y_{\text{H},H_2O} \cdot Y_{\text{H}_2O,F} + Y_{\text{H},H_2} \cdot Y_{\text{H}_2,F} \end{aligned} \tag{C.10}$$

The elemental mass contributions used in Reactions C.8–C.10, which are multiplied with the pyrolysis product yields - the desired outputs of the model - (see Table C.1) -, refer to the mass fractions of elements C, H, and O in each pyrolysis product species. These are calculated based on the molecular weights of the elements and species involved. Therefore:

- $Y_{\text{C,char}}$ = 1, $Y_{\text{C, C}_2\text{H}_4}$ = 24/28, $Y_{\text{C, CO}}$ = 12/28, $Y_{\text{C,CO}_2}$ = 12/44, $Y_{\text{C, CH}_4}$ = 12/16
- $Y_{\text{O, CO}}$ = 16/28, $Y_{\text{O, CO}_2}$ = 16/44, $Y_{\text{O, H}_2\text{O}}$ = 16/18

- $Y_{\mathrm{H,\,C_2H_4}}$ = 4/28, $Y_{\mathrm{H,\,CH_4}}$ = 4/16, $Y_{\mathrm{H,\,H_2O}}$ = 2/18, $Y_{\mathrm{H,\,H_2}}$ = 1

The empirical Equations C.11 - C.20 are essential for the calculation of the pyrolysis products, since it is obvious that the unknowns in this problem (the pyrolysis yields of all the substances) are more than the elemental balances of C, H, O [77].

$$Y_{\mathrm{char},F} = 0.106 + 2.43 \cdot \exp\left(-0.66 \cdot 10^{-2} \cdot T\right) \quad R^2 = 0.56 \tag{C.11}$$

$$Y_{\mathrm{H_2,F}} = 1.145 \cdot \left(1 - \exp\left(-0.11 \times 10^{-2} \cdot T\right)\right)^{9.384}, \quad R^2 = 0.94 \tag{C.12}$$

$$\frac{Y_{\mathrm{H_2,F}}}{Y_{\mathrm{CO,F}}} = 3 \times 10^{-4} + \frac{0.0429}{1 + \left(\frac{T}{632}\right)^{-7.23}}, \quad R^2 = 0.73 \tag{C.13}$$

$$Y_{\mathrm{CH_4,F}} = -2.18 \times 10^{-4} + 0.146 \cdot Y_{\mathrm{CO,F}}, \quad R^2 = 0.88 \tag{C.14}$$

Despite the fact that the LHV of the pyrolysis gas ($\mathrm{LHV_G}$) ideally depends on its composition (e.g., yields of CO, H_2, CH_4, etc. see Equation C.15), the present model uses the empirical Equation C.16 from Neves et al. [77], to estimate the $\mathrm{LHV_G}$ as a function of the pyrolysis temperature, since the gas composition (both the gas yield, $Y_{\mathrm{G,F}}$, and the yields of its individual species) is not already known. Neves' model was based on collected experimental data from literature and validated for different biomass compositions and for a wide range of temperatures.

$$Y_{\mathrm{G,F}} \cdot \mathrm{LHV_G} = Y_{\mathrm{C}_x\mathrm{H}_y,\mathrm{F}} \cdot \mathrm{LHV}_{\mathrm{C}_x\mathrm{H}_y} + Y_{\mathrm{CH_4,F}} \cdot \mathrm{LHV_{CH_4}} + Y_{\mathrm{CO,F}} \cdot \mathrm{LHV_{CO}} + Y_{\mathrm{H_2,F}} \cdot \mathrm{LHV_{H_2}} \tag{C.15}$$

$$\mathrm{LHV}_G = -6.23 + 2.47 \times 10^{-2} \cdot T, \quad R^2 = 0.78 \tag{C.16}$$

Figure C.1 describes the decomposition or the overall mass balance for biomass during pyrolysis, showing that the dry, ash-free fuel (daf) is decomposed into the following four products: char, permanent gas, liquid organics and pyrolytic water, the 3 last of which constitute the pyrolytic volatiles ($Y_{\mathrm{V,F}}$) (Equation C.17).

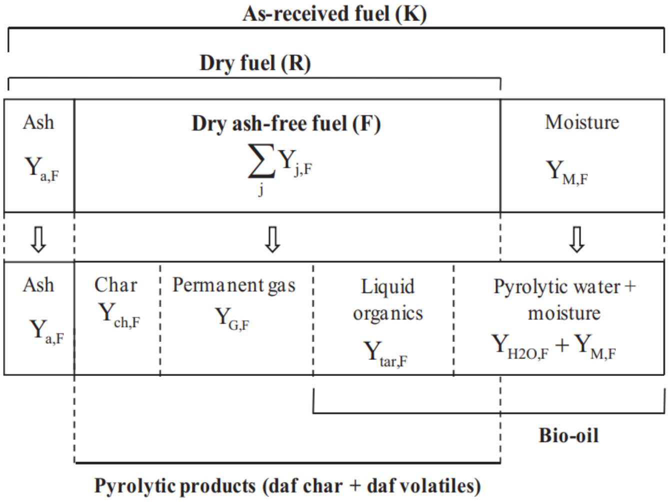

Figure C.1: Overall mass balance of biomass pyrolysis [77]

$$Y_{\mathrm{V,F}} = Y_{\mathrm{G,F}} + Y_{\mathrm{tar,F}} + Y_{\mathrm{H_2}O,\mathrm{F}} \tag{C.17}$$

Therefore, from the mass balance of Figure C.1, it can be seen that the pyrolytic volatiles ($Y_{V,F}$) are comprised of the water-ash-free fuel minus the char content (Equation C.18) and that the permanent gas can be expressed as what is left from the pyrolytic volatiles when we subtract the liquid organics and the pyrolytic water (combining Equation C.17 and Equation C.18 into Equation C.19):

$$Y_{\text{V,F}} = \sum_j Y_{j,F} - Y_{\text{ch},F} \tag{C.18}$$

$$Y_{\text{G,F}} = \sum_j Y_{j,F} - Y_{\text{ch},F} - Y_{\text{H}_2O,\text{F}} - Y_{\text{tar,F}} \tag{C.19}$$

, where j refers to the elements C, H, O.

Hence, Equation C.20 constitutes an alternative form of the energy balance of the total gas (Equation C.15), where, since the total gas yield ($Y_{G,F}$) remains unknown, it is replaced with Equation C.19.

$$\begin{gathered}\left(\sum_j Y_{j,F} - Y_{\text{char},F} \cdot \sum_j Y_{j,\text{char}}\right) \cdot \text{LHV}_G = \\ (Y_{\text{tar},F} + Y_{\text{H}_2\text{O},F}) \cdot \text{LHV}_G + Y_{\text{C}_x\text{H}_y,F} \cdot \text{LHV}_{\text{C}_x\text{H}_y} \\ + Y_{\text{CH}_4,F} \cdot \text{LHV}_{\text{CH}_4} + Y_{\text{CO},F} \cdot \text{LHV}_{\text{CO}} + Y_{\text{H}_2,F} \cdot \text{LHV}_{\text{H}_2}\end{gathered} \tag{C.20}$$

, where j refers to the elements C, H, O.

It should be noted that the temperature in the previous Equations is in Celsius (° C).

Based on the inputs being imported in the model (see Table C.1), the Equations C.2 - C.7 were first solved, followed by Equation C.11 - Equation C.14 and Equation C.16. Lastly, the system of 4 equations Equation C.8, Equation C.9, Equation C.10 and Equation C.20 was solved for, producing the outputs seen in Table C.1.